

SPECTRAL VARIABILITY STUDIES AND ACCELERATION SCENARIOS IN  
JETS OF BLAZARS

A dissertation presented to  
the faculty of  
the College of Arts and Sciences of Ohio University

In partial fulfillment  
of the requirements for the degree  
Doctor of Philosophy

Manasvita Joshi

June 2009

© 2009 Manasvita Joshi. All Rights Reserved.

This dissertation titled  
SPECTRAL VARIABILITY STUDIES AND ACCELERATION SCENARIOS IN  
JETS OF BLAZARS

by

MANASVITA JOSHI

has been approved for  
the Department of Physics and Astronomy  
and the College of Arts and Sciences of Ohio University by

---

Markus Böttcher

Associate Professor of Physics and Astronomy

---

Benjamin M. Ogles

Dean, College of Arts and Sciences

# Abstract

3

JOSHI, MANASVITA, Ph.D., June 2009, Physics and Astronomy

Spectral Variability Studies and Acceleration Scenarios in Jets of Blazars (171 pp.)

Director of Dissertation: Markus Böttcher

This work focuses on the study of spectral energy distributions (SEDs) and the spectral variability patterns of blazars, especially BL Lac objects. It also investigates the dominant mode of particle acceleration in the jets of blazars.

The first part of the work describes the BL Lac object 3C 66A, which was the target of an intensive multiwavelength campaign in 2003/2004. During the campaign, flux measurements from radio to X-ray frequencies and upper limits in the very high energy (VHE)  $\gamma$ -ray regime were obtained. A time-dependent leptonic jet model has been used to obtain a detailed description of the physical processes in 3C 66A. This successful model results in the reproduction of the observed spectral energy distribution (SED) and the optical variability pattern. The model also predicts an intrinsic cutoff value for the VHE  $\gamma$ -ray emission and the possibility of the object being observed by MAGIC, Fermi, and other future missions.

The second part of the work uses the internal shock model to explore the particle acceleration scenarios and the subsequent production of radiation via synchrotron and synchrotron self-Compton processes at sub-pc scales of a relativistic jet. A code has been developed to simulate the acceleration mechanism and to calculate the resulting spectrum after accounting for the inhomogeneity in the photon density throughout

the acceleration region by dividing the region into multiple zones and considering the subsequent time-dependent radiation transfer within the zone and in between zones. An extensive study to understand the effects of varying shock and radiative parameters on the SED and spectral lightcurves of a generic blazar source has been carried out to aid in future theoretical analysis of such sources.

This dissertation also includes a brief description of the observations conducted with the 1.3 m McGraw-Hill telescope of the MDM observatory at Kitt Peak, Arizona. The observations were carried out as a part of an ongoing long-term project designed to monitor the optical variability of a sample of  $\gamma$ -ray loud blazars on various time scales and carry out follow-up observations of the optical afterglows of gamma-ray bursts, should the occasion arise.

Approved:

---

Markus Böttcher

Associate Professor of Physics and Astronomy

*Dedicated to Science*

# Acknowledgments

I thank my advisor, Prof. Markus Böttcher, who gave me the freedom to explore the science in my own style while guiding me towards understanding it correctly and clearly. His door has always been open and his face always beaming with a smile ready to welcome the silliest of my questions at any point of the day. I am forever indebted to him for his moral, professional, and financial support, without which I would not have been able to reach this stage.

I am grateful to Prof. Joseph Shields for guiding and helping me in my professional endeavors, when I most needed it. I am thankful to Prof. Thomas Statler, who was always there when I needed help and guidance. I thank Dr. Mangala Sharma and Dr. Douglas Clowe for their help and advice. I thank Prof. Daniel Phillips for his support. I am thankful to all my committee members: Markus Böttcher, Joseph Shields, M. Prakash, and Howard Dewald, for taking time out of their busy schedules to be a part of my defense.

I thank the entire Department of Physics and Astronomy for being the way it is and feel very lucky to be a part of it. I am grateful to Ms. Ennice Sweigart and Ms. Tracy Inman for their love and support and I thank Mr. Don Roth for his technical support and expertise. I thank the entire staff of Ohio Supercomputer Center (OSC) for their help in running my simulations on their IBM Opteron Cluster - Glenn.

I am extremely grateful to all my friends and colleagues: Azita, Justin, Jack, Steve, Divya, Sudeshna, Swati, Tesfaye, Aman, Inam, for their personal and professional

support and for being with me in good and in bad times of my journey. The love and care they have given me is hard to express in words.

Finally, I would like to express my gratitude to my mom and dad, my sister Trina, my brother Aman, and the rest of my family back in India who always believed in me and had full confidence that I will complete this journey successfully. This part would not be complete if I do not acknowledge the one person who contributed the most, my significant other, Karthikeyan. He has always been there for me, supporting me, and motivating me. Most importantly, I thank him for introducing me to Calvin & Hobbes who always cheer me up, and the Dragon Ball star Goku who inspires me to never give up.

# Table of Contents

	Page
Abstract . . . . .	3
Dedication . . . . .	5
Acknowledgments . . . . .	6
List of Figures . . . . .	10
List of Tables . . . . .	12
List of Symbols . . . . .	13
List of Abbreviations . . . . .	16
1 Introduction . . . . .	19
1.1 Active Galactic Nuclei . . . . .	19
1.2 Blazars . . . . .	24
1.2.1 Spectral classification of blazars . . . . .	27
1.2.2 Spectral variability of blazars . . . . .	28
1.3 Particle acceleration mechanisms . . . . .	29
1.4 Overview . . . . .	30
2 MDM Observations . . . . .	32
2.1 Introduction . . . . .	32
2.2 Observations and Data Analysis . . . . .	34
2.2.1 Observations . . . . .	35
2.2.2 Data Reduction . . . . .	38
2.2.3 Gamma-Ray Burst Afterglows . . . . .	42
2.3 Summary . . . . .	45
3 The BL Lac object 3C 66A . . . . .	46
3.1 Introduction . . . . .	46
3.2 3C 66A Observations . . . . .	48
3.3 Time-dependent Leptonic Jet Model . . . . .	55
3.4 Model Parameters . . . . .	59
3.5 Results . . . . .	64
3.6 Summary . . . . .	79
4 Internal Shock Model for Blazar Jets . . . . .	83

4.1	Introduction . . . . .	83
4.2	Shocks . . . . .	87
4.3	Collision Hydrodynamics . . . . .	91
	4.3.1 Collision Parameters . . . . .	93
	4.3.2 Emission region parameters . . . . .	98
4.4	Photon Escape Timescale . . . . .	101
4.5	Numerical Method . . . . .	105
	4.5.1 The Zone Scheme . . . . .	110
4.6	Time Delays . . . . .	114
4.7	Synchrotron Function Fitting . . . . .	118
4.8	Summary . . . . .	120
5	Modeling Results and Acceleration Scenarios . . . . .	123
	5.1 Parameter Study . . . . .	123
	5.2 Acceleration Scenarios . . . . .	144
	5.3 Summary . . . . .	145
6	Summary and Conclusions . . . . .	146
	6.1 Blazar Observations and Modeling . . . . .	146
	6.2 Internal Shock Model . . . . .	148
	6.3 Modeling Results and Acceleration Scenarios . . . . .	150
	6.4 Future Direction . . . . .	151
	Bibliography . . . . .	155
A	Photon Escape Time Calculation . . . . .	168

# List of Figures

1.1	Schematic of an AGN model . . . . .	21
1.2	Conceptual scheme for unification of radio-quiet AGNs. . . . .	25
1.3	Conceptual scheme for unification of radio-loud AGNs. . . . .	26
1.4	An example of the blazar sequence. . . . .	28
2.1	Photograph of the 1.3 m McGraw-Hill telescope. . . . .	35
2.2	A comparison of the raw and reduced images of the BL Lac object WComae. . . . .	39
2.3	Lightcurves of 3C 66A obtained from the long-term blazar monitoring program. . . . .	41
2.4	An artist's conception of a GRB in a hypernova model. . . . .	43
3.1	Observed lightcurves of 3C 66A in the optical bands. . . . .	51
3.2	Observed SED of 3C 66A at various epochs during the core campaign period in 2003. . . . .	53
3.3	Color-magnitude diagram for the B- and R- bands. . . . .	54
3.4	Schematic diagram of the jet coming out of the central engine of a blazar. . . . .	56
3.5	Simulation of the quiescent state of 3C 66A observed around October 1st 2003. . . . .	65
3.6	Simulation of the flaring state for a generic 10 day flare. . . . .	66
3.7	Time-averaged SED of 3C 66A for a period of 23 days. . . . .	68
3.8	The simulated lightcurve for various flaring profiles. . . . .	70
3.9	Simulated lightcurves for the optical, X-rays and $\gamma$ -ray energy regimes. . . . .	71
3.10	The simulated hardness-intensity diagram. . . . .	72
3.11	Simulated spectral hysteresis pattern in the R-band, 1 keV and 10 keV energy regimes. . . . .	76
3.12	Simulated hysteresis pattern for 1 MeV, 100 MeV and 10 GeV energy regimes. . . . .	77
3.13	Simulation of the effect of the BLR on the instantaneous SED of 3C 66A. . . . .	79
4.1	Schematic of the shock propagation through a medium. . . . .	90
4.2	Schematic of inner and outer shells propagating through a well collimated jet. . . . .	93
4.3	Diagram of the two-shell interaction resulting in an inelastic collision. . . . .	95
4.4	Illustration of the three possible direction of photon escape from a cylindrical region. . . . .	103
4.5	Comparison of the volume and angle averaged photon escape timescales . . . . .	104
4.6	Illustration of the zone scheme used in the modelling. . . . .	111
4.7	Comparison of the exact expression and numerical approximation of $R(x)$ . . . . .	119

5.1	Simulated time-averaged SED of a generic source illustrating the effect of varying wind parameters. . . . .	131
5.2	Simulated time-averaged SED of a generic source illustrating the effect of varying 1st set of shell parameters. . . . .	133
5.3	Simulated time-averaged SED of a generic source illustrating the effect of varying 3rd set of shell parameters. . . . .	134
5.4	Simulated time-averaged SED of a generic source illustrating the effect of varying 1st set of emission-region parameters. . . . .	135
5.5	Simulated time-averaged SED of a generic source illustrating the effect of varying 2nd set of emissio-region parameters. . . . .	137
5.6	Simulated time-averaged SED of a generic source illustrating the effect of varying 3rd set of emission-region parameters. . . . .	139
5.7	Simulated time-averaged SED of a generic source illustrating the effect of varying jet parameter. . . . .	140
5.8	Example of simulated lightcurves of a generic blazar source resulting varying 1st set of shell parameters. . . . .	141
5.9	Simulated lightcurves of a generic blazar source various energy bands illustrating the effect of varying shell widths. . . . .	142
5.10	Simulated lightcurves in various energy bands of a generic source illustrating the effect of varying $q$ . . . . .	143
A.1	Angle and escape length considerations for a cylinder geometry. . . . .	169

# List of Tables

1.1	Possible simple unification according to weak unification model. . . .	24
3.1	Model Parameters used to reproduce the quiescent and flaring state of 3C 66A as shown in Figures 3.5 and 3.6, respectively. . . . .	62
5.1	Parameter list used to obtain the first simulation from run 1. . . . .	126
5.2	Parameter list for various simulations used for the parameter study.	127
5.3	Parameter study of the shock, emission-region, and jet parameters. .	129

# List of Symbols

$z$	Redshift of an object
$c$	Speed of light
$R_b$	Radius of the blob
$q$	Particle spectral index
$\gamma_{1(2)}$	Particle low (high) energy cutoff
$Q_e^{inj}$	Particle injection function
$Q_0^{inj}$	Particle injection density
$L_{inj}$	Particle injected luminosity
$B$	Magnetic field
$\epsilon_B$	Equipartition parameter
$U_B$	Magnetic field energy density
$U_e$	Electron energy density
$\Gamma$	BLF of the blob
$\theta_{obs}$	Angle between the jet and our line of sight
$\sigma_T$	Thomson cross section
$P_{syn}$	Synchrotron power
$P_{IC}$	Inverse Compton power
$U_{ph}$	Photon energy density
$t_{e,esc}$	Electron escape timescale
$t_{ph,esc}$	Photon escape timescale

$D$	Doppler boosting factor
$L_D$	Bolometric disk luminosity
$\tau_T$	Thomson optical depth
$\tau_{cool, syn}^{obs}$	Observed synchrotron cooling timescale
$\tau_{dyn}^{obs}$	Observed dynamical timescale
$B_G$	Magnetic field strength in Gauss
$\nu_{syn(ssc)}^{peak}$	Peak Synchrotron (SSC) frequency
$\nu_{ssc, cutoff}$	SSC cutoff frequency
$u_{0(1)}$	Speed of the unshocked (shocked) fluid
$\rho_{0(1)}$	Density of the unshocked (shocked) fluid
$P_{0(1)}$	Pressure of the unshocked (shocked) fluid
$\Gamma_{i(o)}$	BLF of the inner (outer) shell
$M_{i(o)}$	Mass of the inner (outer) shell
$\Delta_{i(o)}$	Width of the inner (outer) shell
$\Gamma_m$	BLF of the merged shell
$E_{int}$	Internal energy of the merged shell
$\Gamma_{sh}$	BLF of the emission region
$\Gamma_{FS(RS)}$	BLF of the FS (RS) front
$E_{fs(rs)}$	Internal energy of the forward (reverse) region
$\rho_{fs(rs)}$	Matter density of baryons in the forward (reverse) region
$p_{fs(rs)}$	Pressure of the shocked fluid in the forward (reverse) region

$\Delta_{fs(rs)}$	Width of the forward (reverse) region
$t_{cr,fs(rs)}$	Shock crossing time of the forward (reverse) region
$\gamma_{min(max)}$	Minimum (Maximum) RLF of electrons
$U_{fs}$	Forward shock energy density
$\varepsilon_B$	Fraction of shock energy stored as magnetic energy
$\varepsilon_e$	Fraction of shock energy stored as electron energy
$\zeta_e$	Fraction of electrons effectively accelerated
$\alpha$	Electron acceleration rate parameter
$R$	Radius of the cylindrical region
$h$	Height of the cylindrical region
$L_w$	Wind luminosity
$t_w$	Total duration of the wind
$r_L$	Larmor radius

# List of Abbreviations

<i>AGILE</i>	Astrorivelatore Gamma ad Immagini LEggero
<i>AGN</i>	Active Galactic Nuclei
<i>BLF</i>	Bulk Lorentz Factor
<i>BLLac</i>	BL Lacertae
<i>BLR</i>	Broad Line Region
<i>BLRG</i>	Broad Line Radio Galaxy
<i>CCD</i>	Charge Coupled Device
<i>CD</i>	Contact Discontinuity
<i>CGRO</i>	Compton Gamma Ray Observatory
<i>EC</i>	External Compton
<i>EGRET</i>	Energetic Gamma Ray Experiment Telescope
<i>FRI(II)</i>	Fanaroff-Riley type I(II)
<i>FS</i>	Forward Shock
<i>FSRQ</i>	Flat Spectrum Radio Quasar
<i>GRB</i>	Gamma Ray Burst
<i>HBL</i>	High-frequency-peaked BL Lac
<i>HID</i>	Hardness Intensity Diagram
<i>IC</i>	Inverse Compton
<i>IIRB</i>	Intergalactic Infrared Radiation Background
<i>IR</i>	Infra Red

<i>IRAF</i>	Image Reduction and Analysis Facility
<i>KN</i>	Klein Nishina
<i>LBL</i>	Low-frequency-peaked BL Lac
<i>NLR</i>	Narrow Line Region
<i>NLRG</i>	Narrow Line Radio Galaxy
<i>OVP</i>	Optical Variability Pattern
<i>OVV</i>	Optically Violent Variables
<i>PCA</i>	Proportional Counter Array
<i>RLF</i>	Random Lorentz Factor
<i>RLQ</i>	Radio Loud Quasar
<i>ROSAT</i>	ROentgen SATellite
<i>RS</i>	Reverse Shock
<i>RXTE</i>	Rossi X-ray Timing Explorer
<i>SED</i>	Spectral Energy Distribution
<i>SMBH</i>	Super Massive Black Hole
<i>SSA</i>	Synchrotron Self Absorption
<i>SSC</i>	Synchrotron Self Compton
<i>STACEE</i>	Solar Tower Air Cherenkov Effect Experiment
<i>ToO</i>	Target of Opportunity
<i>UV</i>	Ultra Violet
<i>VERITAS</i>	Very Energetic Radiation Imaging Telescope Array System

<i>VHE</i>	Very High Energy
<i>VLBA</i>	Very Large Baseline Array
<i>VLBI</i>	Very Long Baseline Interferometry
<i>WEBT</i>	Whole Earth Blazar Telescope
<i>XMM</i>	X-ray Multi Mirror

# CHAPTER 1

## Introduction

### 1.1 Active Galactic Nuclei

Modern observations of galaxies reveal a very high level of activity in the center of certain galaxies, which is not a feature of a typical galaxy. The center of such an active galaxy, which is roughly the innermost 1% of the galaxy, is generally brighter than the rest of the galaxy. Such galaxies, with active galactic nuclei (AGN), are bright and luminous objects and are believed to harbor a super-massive black hole (SMBH) in their center. The tremendous amount of power that is observed from such objects is attributed to the presence of this SMBH, which gradually accretes matter via an accretion disk and releases large amounts of energy in the form of relativistic outflows, called jets (Figure 1.1).

As shown in Figure 1.1, the central engine consisting of the SMBH and the accretion disk is what is responsible for powering up the jets to highly relativistic energies. The broad line region (BLR) that is relatively close to the central engine is a high-density clumpy region consisting of thick gas clouds. The number density of electrons, present in this region, lies between  $10^9$  and  $10^{10} \text{ cm}^{-3}$  (Carroll and Ostlie 1996). This region gives rise to broad emission lines seen in the spectra of many AGNs. The BLR and the central engine are surrounded by a thick torus of gas and dust. If viewed from

the side, the dough-nut shaped molecular torus does not allow the radiation coming from the disk (continuum) and the emission lines of the BLR to reach the observer directly, and hence, is optically thick to the radiation. The narrow line region (NLR) also contains clouds of gas that give rise to narrow emission lines, seen in the spectrum of many AGNs. This is because the number density of electrons in NLR is only  $\sim 10^4 \text{ cm}^{-3}$ , and due to its low density, the gas in this region produces both allowed and strong forbidden emission lines. The jets are composed of highly relativistic particles, like electrons, protons and positrons. These particles subsequently cool off via synchrotron radiation or Compton upscattering of photons to produce radiation in the entire electromagnetic spectrum.

The two largest subclasses of AGNs are Seyfert galaxies and quasars. The main difference between them is in the amount of radiation emitted by the compact central source or the central engine. The total energy emitted by the nucleus of a typical Seyfert galaxy at visible wavelengths is comparable to the energy emitted by all of the stars in the galaxy, whereas in a typical quasar the nuclear source is brighter than the stars by a factor of 100 or more ([Peterson 1997](#)).

A Seyfert galaxy has a quasar-like nucleus although the host galaxy is clearly detectable. They are mostly found in spiral galaxies and are further divided into two subclasses, namely the Seyfert 1 and Seyfert 2. Two sets of emission lines are superposed on one another in the spectra of Seyfert 1 galaxies. One set of lines are the narrow emission lines resulting from the low-density ionized gas and the second

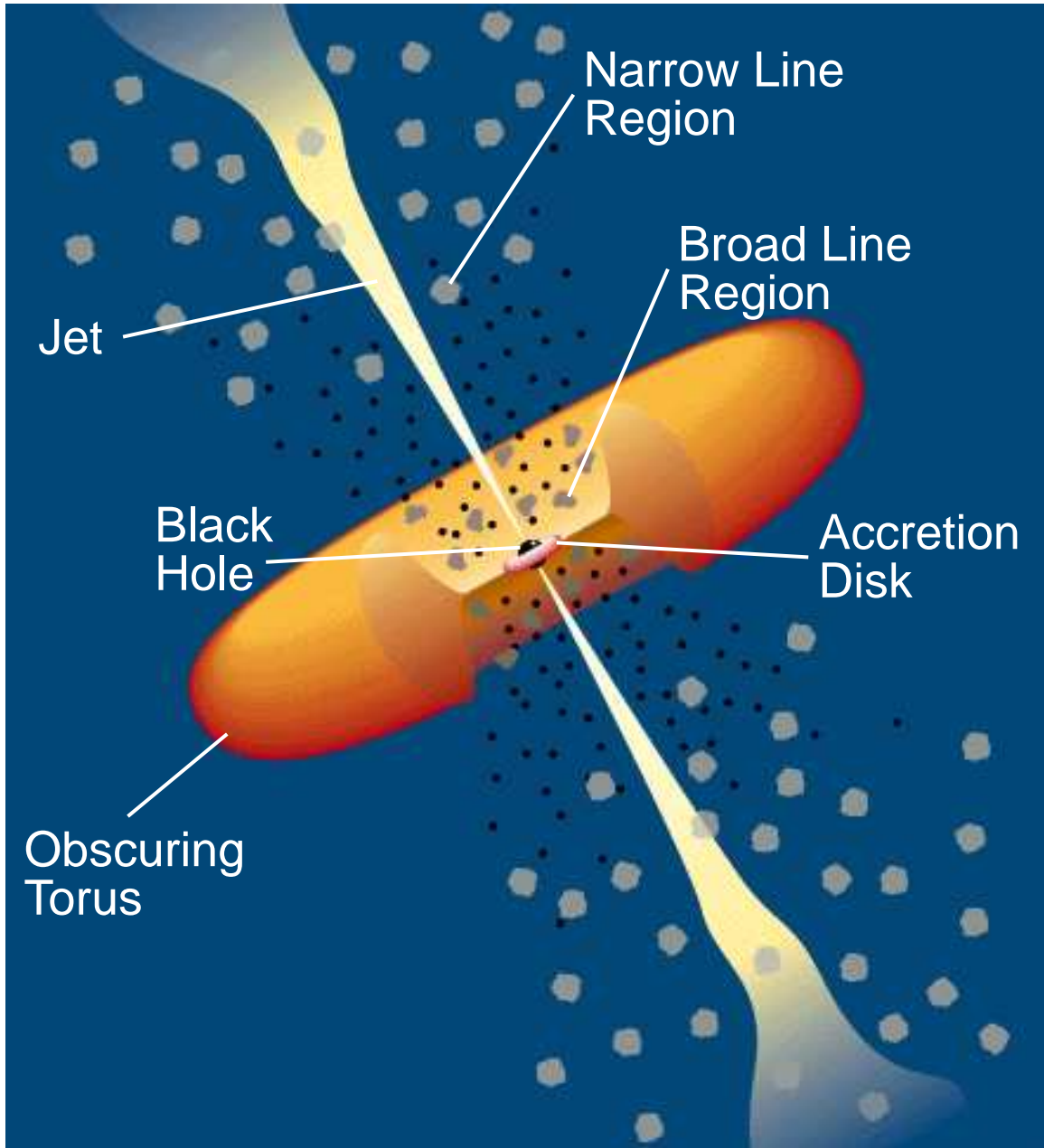


Figure 1.1: Schematic of an AGN model. Credit: C.M. Urry and P. Padovani ([http://heasarc.gsfc.nasa.gov/docs/cgro/images/epo/gallery/agns/agn\\_up\\_model.gif](http://heasarc.gsfc.nasa.gov/docs/cgro/images/epo/gallery/agns/agn_up_model.gif))

set of lines are the broad permitted emission lines characteristic of the high density ionized gas. In the case of Seyfert 2 galaxies, only narrow lines are present in their spectra (Peterson 1997).

Quasars, also known as quasi-stellar objects (QSOs), are the most luminous subclass of AGNs. They are star-like objects that exhibit broad emission lines and are variable in every waveband in which they have been studied. The variability is present in the continuum as well as in the broad emission lines. They have large UV fluxes referred to as the “ultraviolet excess” of quasars. Quite often, the radio morphology of quasars and radio galaxies is broadly described in terms of two components, an extended component (radio lobe) that is spatially resolved and a compact core that is unresolved at  $\approx 1''$  resolution. Fanaroff-Riley type I (FR I) radio galaxies are an example of such a two-component radio morphology. In addition to these two components, quasars often exhibit the presence of jets that appear to originate at the central compact source and extend out to the radio lobes. The Fanaroff-Riley type II (FR II) radio galaxies are examples of such three-component radio morphology and quasars are mostly associated with FR II type sources. Quasars are found in two categories, radio-loud and radio-quiet quasars. The radio emission of radio-quiet quasars is 100 times lower than their UV-optical-IR emission (Peterson 1997).

Two types of radio galaxies, the broad-line radio galaxies (BLRG) and the narrow-line radio galaxies (NLRG), have optical spectra of the sort that is identified with AGN activity and are considered to be the radio-loud analogs of Seyfert 1 and 2

galaxies, respectively. An important difference between these radio galaxies and the Seyferts is that unlike Seyferts they are found to have elliptical host galaxies rather than spirals (Peterson 1997).

A small subset of AGNs show very large variations in their flux over short time scales. Such AGNs are known as optically violent variables (OVVs). Some of the properties of OVVs are shared by BL Lac objects (BL Lacs), named after the prototype of the class, BL Lacertae, which was originally identified as a highly variable star. The OVVs and BL Lacs together form the subclass of AGN called the blazars (Peterson 1997), which are discussed in detail in the next section.

All subclasses of AGNs show clear evidence for anisotropy in their radio and higher-frequency radiation. This implies that the appearance of a given AGN depends strongly on the observer's location relative to the axis of symmetry of the AGN. Thus, the classification of AGNs might be a function of the viewing angle. This idea is the building block of the “unified models” of AGNs. There are two types of unified models, weak and strong. In the weak unification model there are two types of AGNs, radio-quiet and radio-loud, that can be unified on the basis of the variations in their optical and radio luminosity as well as the apparent differences due to the orientation of the system relative to the observer (Peterson 1997). The basic aspects of a general unification scheme according to the weak model are given in Table 1.1 (Peterson 1997), where FIR stands for Far InfraRed.

Table 1.1: Possible simple unification according to weak unification model. Credit: (Peterson 1997).

Radio Properties	Orientation	
	Face-on	Edge-on
Radio Quiet	Seyfert 1	Seyfert 2
	QSO	FIR galaxy?
Radio Loud	BL Lac	FR I
	BLRG	NLRG
	Quasar/OVV	FR II

Figures 1.2 and 1.3 illustrate the conceptual scheme for unification of Seyfert galaxies, and FR I, FR II & blazars, respectively (credit: [segre.ieec.uab.es/AAE\\_UAB/2003-04/classes/agn01.ppt](http://segre.ieec.uab.es/AAE_UAB/2003-04/classes/agn01.ppt)). The strong unification model, on the other hand, attributes all the differences observed in AGNs to the various orientation effects.

## 1.2 Blazars

Blazars are the most extreme class of AGNs exhibiting the most violent high-energy phenomena observed till now. This class is comprised of BL Lac objects and flat spectrum radio quasars (FSRQs). They have been observed at all wavelengths, from radio through very-high energy (VHE)  $\gamma$ -rays. The eminent features of these objects are non-thermal continuum spectra, a high degree of linear polarization in the optical, rapid variability at all wavelengths on various time scales, and radio jets with individual components often exhibiting apparent superluminal motion that is relativistically beamed towards our line of sight. Blazars are classified according

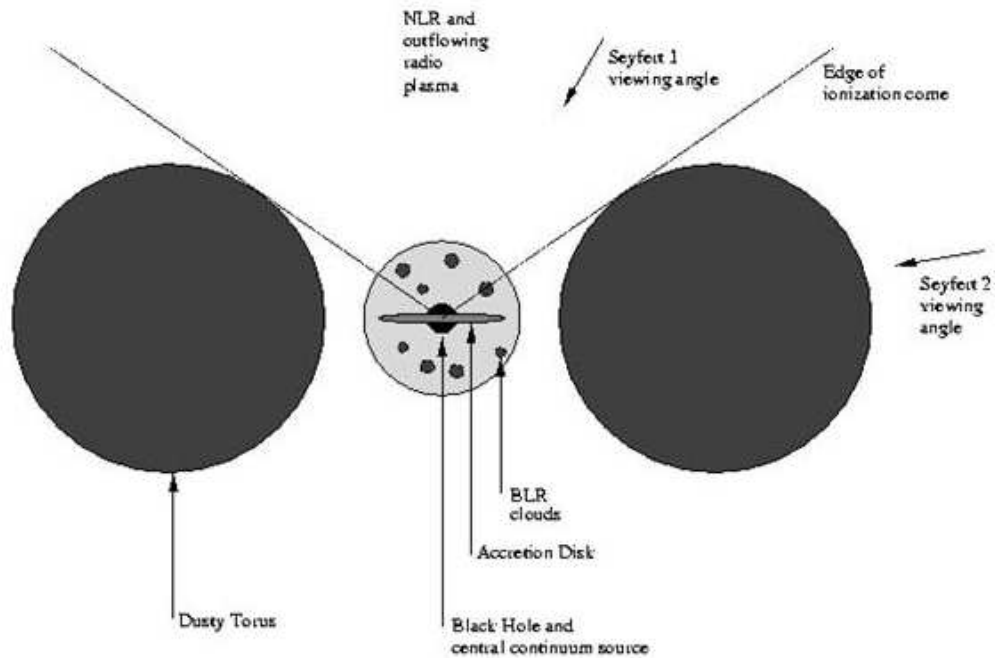


Figure 1.2: Conceptual scheme for unification of radio-quiet AGNs. A dusty torus surrounds the central continuum source and the BLR. An observer close to the torus axis would have an unobscured view of the central region and will classify the AGN as a “Seyfert 1” whereas an observer closer to the torus midplane would not be able to see this region directly but will see the NLR directly and will classify the same AGN as a “Seyfert 2”. Credit: Francisco Castander.

to the survey they were monitored in and the sequence followed to observe them.

For example, the blazar 3C 66A stands for the 66<sup>th</sup> object observed in the third Cambridge survey and cataloged at that position. The letter “A” is attached to its name to distinguish it from a nearby radio source 3C 66B separated from 3C 66A by  $\sim 6$  arcmin in the sky (Böttcher et al. 2005). An arcminute is a unit of angular measurement and is equal to  $(1/60)^{\text{th}}$  of a degree.

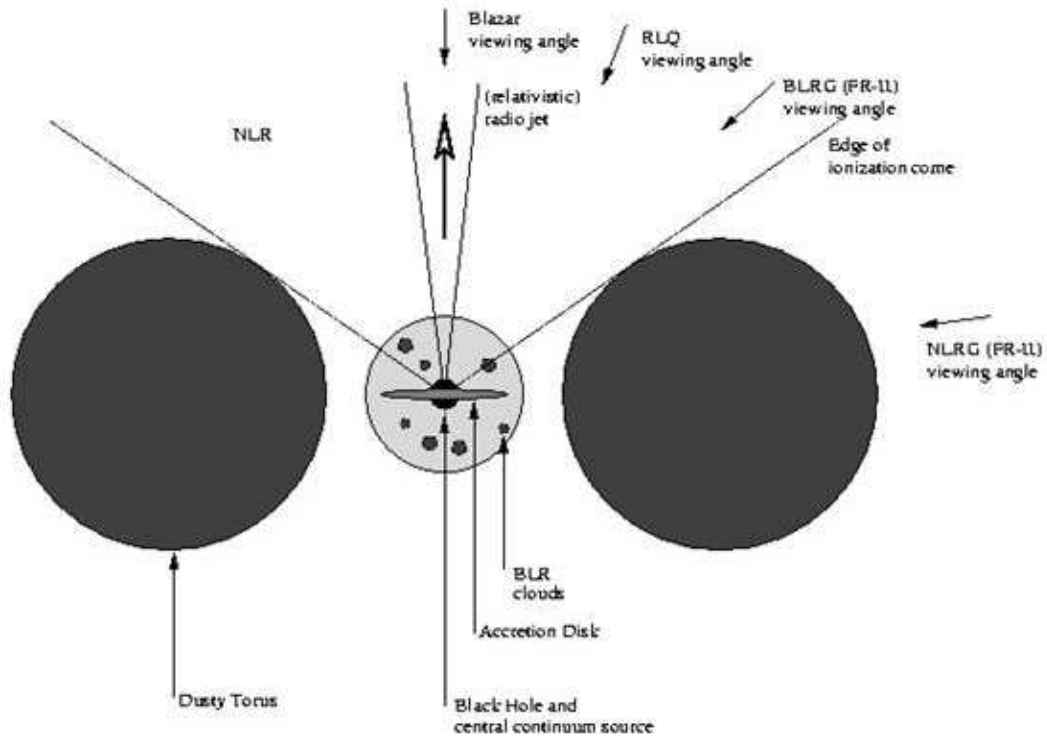


Figure 1.3: Conceptual scheme for unification of radio-loud AGNs. Depending on the location of the observer with respect to jet axis, the radio-loud AGN would get classified either as a blazar, radio-loud quasar (RLQ), a BLRG, or an NLRG. FR I radio galaxies, not shown in the figure, are believed to be the parent population of BL Lac objects. A BL Lac object when viewed edge-on can get classified as an FR I. Credit: Francisco Castander.

The properties of BL Lac objects and FSRQs are very similar except that BL Lacs are distinguished by the absence of strong emission or absorption lines in their spectra. However, weak emission or stellar absorption lines can be detected in very high signal-to-noise-ratio spectra although with an equivalent width, in the rest-frame of the host galaxy, of  $< 5\text{\AA}$ .

### 1.2.1 Spectral classification of blazars

The broadband spectrum of blazars exhibits two broad spectral components and is dominated by non-thermal emission. The low energy component is attributed to synchrotron emission from non-thermal electrons in a relativistic jet. The high energy component is due either to the Compton upscattering of low-energy radiation by the synchrotron-emitting electrons (for a recent review see, e.g., [Böttcher 2007](#)) or hadronic processes initiated by relativistic protons co-accelerated with the electrons ([Mücke et al. 2003](#); [Mücke and Protheroe 2001](#)). The peak frequencies and relative  $\nu F_\nu$  fluxes of these two components provide the observational distinction between various blazar sub-classes. Here,  $F_\nu$  is the flux observed per unit frequency interval. It is usually measured in units of  $\text{ergs s}^{-1}\text{cm}^{-2}\text{Hz}^{-1}$ . The  $\nu F_\nu$  peak frequencies increase whereas the  $\nu F_\nu$  peak value and the dominance of the  $\gamma$ -ray flux over the low-frequency emission decrease (Figure 1.4), as the sequence progresses from FSRQ to high-frequency peaked BL Lac (HBL) through low-frequency peaked BL Lac (LBL) object. LBLs are intermediate between the FSRQs and the HBLs. Their low-frequency component peak lies in the IR or optical regime whereas the high-energy component peak is located at several GeV and the  $\gamma$ -ray output is slightly higher than the spectral output of their low-frequency counterpart. However, recent observations have questioned the existence and physical significance of this blazar sequence and the apparent sequence has been attributed to selection effects arising from the use of flux-limited samples ([Padovani 2007](#)).

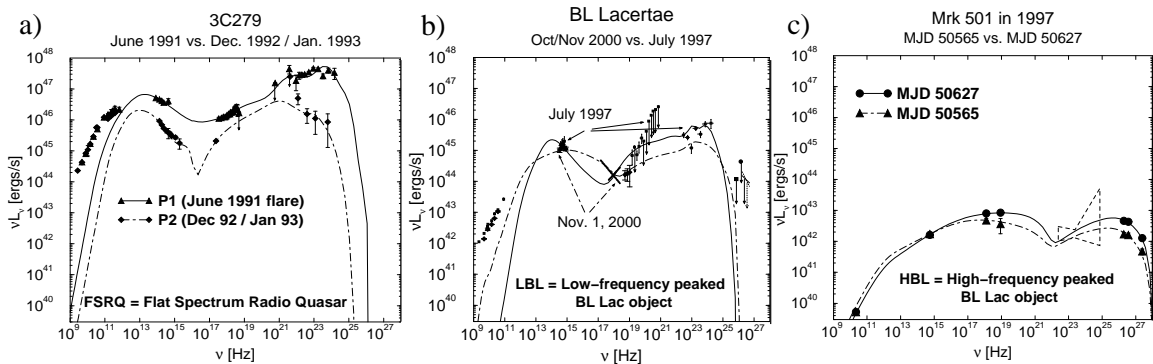


Figure 1.4: An example of the blazar sequence using the SEDs of, the quasar, 3C 279 (Hartman et al. 2001), the LBL, BL Lacertae (Böttcher et al. 2003), and, the HBL, Mrk 501 (Petry et al. 2000). For each object, two simultaneous broadband spectra at two different epochs are shown. The curves show the simulated SEDs, using a leptonic jet model.

## 1.2.2 Spectral variability of blazars

Blazars are often known to exhibit variability at all wavelengths, varying on time scales from months to a few days, to even less than an hour in some cases (e.g., Aharonian et al. 2007; Albert et al. 2007; Gaidos et al. 1996; Catanese and Weekes 1999). At x-ray energies, some HBLs exhibit characteristic features when the photon energy spectral index,  $\alpha$ , is plotted against the x-ray flux. These plots are known as the hardness-intensity diagrams (HIDs) and the clockwise loop structures are called spectral hysteresis (e.g. see, Section 3.11). This spectral hysteresis can be interpreted as the signature of synchrotron radiation, due to the gradual injection and/or acceleration of ultrarelativistic electrons in the emitting region and their subsequent radiative cooling (Kirk et al. 1998; Georganopoulos and Marscher 1998; Kataoka et al. 2000; Kusunose et al. 2000; Li and Kusunose 2000; Böttcher and Chiang 2002). In

case of LBLs, it becomes hard to observe this feature as these objects are much fainter than HBLs at x-ray energies, thereby making the extraction of time-resolved spectral information observationally very challenging.

Measurements of blazar spectral variability are important tools in constraining physical models, pertaining to the location and primary mechanism of acceleration of relativistic electrons and their subsequent radiative cooling (Li and Kusunose 2000; Kusunose et al. 2000; Böttcher and Chiang 2002). Results of detailed spectral and variability models can also shed light on the dynamics of the central engine, associated with the formation of collimated relativistic outflows (jets). Microvariability on intraday time scales, accompanied by simultaneous observations at higher frequencies, especially x-rays and  $\gamma$ -rays, are important tools in constraining the electron energy distribution, total energy requirements, magnetic fields, geometry, and details of the electron acceleration in the jets of blazars.

### 1.3 Particle acceleration mechanisms

In order to understand the physics of relativistic outflows fully, it is imperative to know the mode and location of the mechanism responsible for accelerating the radiating particles to such high energies in the jet. The acceleration of particles in such outflows, at a location closer to the central engine (sub-pc scales), is mostly associated with the propagation of relativistic shocks through the jet.

The location of the injection of particles into the emitting region and the mechanism for their subsequent acceleration still remain open questions to be answered. Significant progress has been made in this area in the past few years. In the case of leptonic jet models, the electrons could be injected and/or accelerated through various scenarios, like, impulsive injection near the base of the jet (Dermer and Schlickeiser 1993; Dermer et al. 1997). Isolated shocks propagating along the jet (Marscher and Gear 1985; Kirk et al. 1998; Sikora et al. 2001) or internal shocks from the collision of multiple shells of material in the jet (Spada et al. 2001) are amongst the favored models for explaining the acceleration of electrons. The more recent scenarios for explaining the acceleration are parallel (Sokolov et al. 2004) and oblique shocks (Ostrowski and Bednarz 2002) propagating through a pre-existing jet or particle acceleration in shear flows existing in relativistic jets (Rieger and Duffy 2004). All the above mentioned shocks and different types of acceleration processes will be discussed in detail in Chapters 4 and 5.

## 1.4 Overview

The goal of this work is to understand the physics of relativistic jets, especially those of BL Lac objects, by means of spectral and variability studies. A brief description of my observational efforts, in the optical band, in order to carry out the spectral and variability studies on various blazars, is given in Chapter 2. Chapter 3 describes the observational and theoretical analysis of the BL Lac object 3C 66A that was ob-

served simultaneously in the entire electromagnetic spectrum in the year 2003 - 2004. In Chapter 4, I discuss the theoretical model and the code that I have developed to study the acceleration mechanism and radiation transfer in blazars. Chapter 5 enunciates the results obtained from this theoretical modeling of the acceleration and radiation processes in the jets of blazars. Finally, I conclude with the implications of my work and where to go from here in Chapter 6.

This dissertation has Appendix A that lays out the important steps used for analytically obtaining the expression for the volume and angle-averaged escape timescale of a photon from a cylindrical geometry.

## CHAPTER 2

# MDM Observations

### 2.1 Introduction

Observations of celestial objects throughout the electromagnetic spectrum are what really defines astronomy. The radiation that is collected in such observations is analyzed to give insights and aid in the theoretical understanding of the physics of astronomical objects. One such way of attempting to comprehend the physics of complex processes taking place inside a celestial body is via optical astronomy. A tiny fraction of the electromagnetic spectrum is the visible part, which spans the wavelength range of 400-700 nm. The visible part forms the main ingredient of optical astronomy although observations of celestial objects at ultraviolet and near-infrared wavelengths are also carried out using optical telescopes. Optical telescopes are extensively used in blazar monitoring campaigns. The observations provide us with valuable information regarding the optical variability patterns (OVPs) of such highly variable objects. They give us information about any kind of correlation that might exist, in an object, between optical and other wavebands (X-rays,  $\gamma$ -rays, etc.). They also shed light on the interplay of different physical processes responsible for producing the observed radiation.

A long-term blazar monitoring program to capture the optical variability patterns of some highly energetic blazars is being carried out at the MDM observatory. The MDM observatory is located at Kitt Peak, Arizona, and consists of two optical telescopes, the 2.4 m Hiltner telescope and the 1.3 m McGraw-Hill telescope. The 2.4 m and 1.3 m refer to the diameter of the primary mirror used in these reflector-type optical telescopes. The observatory is owned and run by a consortium of five universities: University of Michigan, Dartmouth College, Ohio State University, Columbia University, and Ohio University. This gives the blazar-monitoring group an easy access to conduct their observations, primarily, on the 1.3 m McGraw-Hill telescope. The group carries out 4 observational runs each year, with each run separated from the previous one by about 2-3 months. This allows an approximately even sampling of the long-term light curves of the targets.

Besides being intensively involved in the theoretical analysis of blazars and developing a theoretical model to understand the acceleration mechanism of relativistic particles in such objects, I have also been involved in directly observing blazars with the 1.3 m MDM telescope. In this chapter, I will describe my involvement with the group in obtaining the data for the target  $\gamma$ -ray blazars and the subsequent data reduction of a few blazars. This on-going project is aimed at understanding the OVPs of such blazars in order to put stronger constraints on the mode of particle acceleration in the jets of blazars. In addition to the blazar-monitoring program, I have

also carried out optical follow-up observations of the afterglows of a few  $\gamma$ -ray bursts (GRBs), which will be described in a later section of this chapter.

## 2.2 Observations and Data Analysis

The entire blazar-monitoring program including the follow-up observations of GRB afterglows is carried out on the 1.3 m McGraw-Hill telescope. The telescope has an equatorial mount, which means that one rotational axis of the telescope is parallel to the Earth's axis of rotation. It is a Cassegrain-type telescope, in which, the parabolic-shaped primary mirror focuses the light onto a convex hyperbolic-shaped secondary mirror. The primary mirror is perforated from the center and the secondary mirror is placed inside the focal length of the primary mirror, so that the incoming radiation is finally focused at a point behind the primary mirror. All the electronics and the light acquisition devices are attached to the telescope at this point (Fig. 2.1). The data are collected using a CCD-camera and can be acquired in five optical wavebands, namely the ultraviolet (U), blue (B), visual (V), red (R), and the near-infra-red (I).

In Section 2.2.1, I will describe our procedure of obtaining the data. The preliminary data reduction steps are described in Section 2.2.2. The follow-up observations of the GRB afterglows are described in Section 2.2.3.



Figure 2.1: Photograph of the 1.3 m McGraw-Hill telescope of the MDM observatory located at Kitt Peak, Arizona. The long green-colored tube is the equatorial mount. Connected to this tube is the waffle-tree arrangement that supports the primary mirror, not seen in the photograph, and the secondary mirror, of diameter 0.5 m, on the top. Credits: Markus Böttcher

### 2.2.1 Observations

The main purpose of this long-term blazar monitoring project is to sample the OVP of  $\gamma$ -ray loud blazars on intranight timescales to put stricter constraints on the dominant mode of acceleration of particles in the jets of these blazars. This class of blazars consists of BL Lac objects and  $\gamma$ -ray loud FSRQs that can be detected at  $E > 100$  MeV.

This project serves a variety of other important scientific purposes besides achieving our main goal. One of the purposes is to contribute to on-going monitoring programs by the international Whole Earth Blazar Telescope (WEBT) collaboration. WEBT is a conglomeration of optical, near-infrared, and radio telescopes located all over the globe. The observing activity, in case of WEBT, shifts from east to west around the world as the Earth rotates (<http://www.to.astro.it/blazars/webt/>). This allows for a continuous and densely sampled monitoring of blazars at all times. We include some of WEBT targets in our observing runs and provide WEBT with the acquired data, which is then used in conjunction with the data obtained from other wavebands to analyze the physical properties of target objects (Raiteri et al. 2008). The other scientific purpose served by our project is the optical observations of a few target blazars in tandem with on-going X-ray and  $\gamma$ -ray observations of the same objects (Ciprini et al. 2007). Such types of simultaneous and multiwavelength blazar campaigns are extremely useful for better understanding the broadband emission of blazars.

Depending on the level of optical emission exhibited by the object during our run, our optical data serve as a triggering point for conducting high-energy (X-ray and  $\gamma$ -ray) observations of that object (Böttcher et al. 2007). We also look for any correlation that might exist between the brightness of some well-known blazars and their intranight variability timescales to compare against theoretical model predictions. This investigation is carried out by studying their color-magnitude diagram, which is

an indicator of how the brightness and spectral hardness (producing more energetic photons), of an object, are related during a certain time-interval. The other purpose of this project is to monitor some of the few, very poorly observed and understood blazars in order to study their variability properties and look for degree of similarity with other better-known blazars. In addition to the blazar-monitoring program, we also participate in the optical monitoring of GRB afterglows if the occasion arises, and have been successful a few times (see e.g., [Akerlof et al. 2006](#); [Yost et al. 2006](#); [Böttcher and Joshi 2005](#); [Mirabal et al. 2005](#)).

The observations for these objects are carried out in the standard UBVRI system of filters. These filters transmit an object's light only within certain narrow wavelength bands. The filtering of light helps us measure the brightness of an object in a particular bandpass that falls within the wavelength range of the filter being used. The brightness measurement helps us detect any kind of variability (flaring) that might be taking place inside the object at that time. Since any filter lets only a specific range of wavelength pass through, filters in general are also indicators of the energy range in which a particular object is emitting. The U filter lets the highest-energy optical photons pass through whereas the I filter lets the least-energy optical photons pass through. All our target sources emit in all these optical wavebands and are observed for  $\sim 45 - 90$  sec in the R band. The exposure time for a source in a particular waveband increases as we go to higher-frequency bands, with it becoming up to  $\sim 120 - 180$  sec for the U band.

The sources are observed in sets of UBVRI sequences, with each set lasting for  $\sim 1$  hour. If a particular object shows traces of intranight variability (microvariability) or is known to be in a flaring state, then this set is repeated a few times for as long as the object is up on the sky in order to get a dense and evenly-spaced sampling of the data. Each observation run lasts for about a week with  $\sim 12$  hours of night-time available for observing during winters and  $\sim 8$  hours for summers.

I have been on six of these one-week-long observation runs. I have observed almost all of our target blazar sources including the BL Lac object 3C 66A. The data for 3C 66A, obtained from these runs are used for carrying out microvariability studies on 3C 66A to better understand the dominant mode of acceleration mechanism in this object.

### **2.2.2 Data Reduction**

The raw data obtained from each object needs to be refined in order to be used for the science. This is carried out by using the software Image Reduction and Analysis Facility (IRAF). The basic reduction involves removing variations in sensitivity across the detector that are introduced from the electronics of the telescope. The reduction also includes removing cosmic ray hits from images with exposure time longer than  $\sim 10$  minutes. Figure 2.2 shows a comparison of the raw and the reduced image of the BL Lac object WComae. As can be seen in the figure, some unwanted pixels are



Figure 2.2: A comparison of the raw (left) and reduced (right) images of the BL Lac object WComae. The original (raw) image was taken in the R band with an exposure time of 60 seconds. The arrow indicates the location of the object in the image, as seen by the telescope.

absent from the reduced image and the image of every object in the reduced image is comparatively sharper and clearer.

Once the basic data reduction of all the images of an object from a particular night is over, we can carry out relative photometry on those images. This gives us a measure of the relative brightness of that object with respect to that of the well-calibrated stars present in the field of the object. The brightness is measured in terms of the magnitude of an object and is related to the received flux of the object according to the formula:

$$m_1 - m_2 = -2.5 \log_{10} \left( \frac{F_1}{F_2} \right). \quad (2.1)$$

Here,  $m_1$  and  $m_2$  stand for the magnitude of the object and the comparison star, respectively, and  $F_1$  and  $F_2$  are the corresponding received fluxes. A lower value of the magnitude of an object implies a brighter object and vice-versa. Using the DAOPHOT package of IRAF, we obtain the instrumental magnitude of an object in a particular filter. The instrumental magnitude of the object is then converted into its physical magnitude by calibrating the instrumental magnitude of the object with the magnitudes of the standard stars present in the field of view. Using the physical magnitudes we plot the lightcurve of the object for that particular band over the entire observation time. Lightcurves of the object in all the rest of the optical bands can also be plotted using the same techniques. These graphs, which are essentially plots of magnitude and time of observation, are used to study the short- and long-term variability of the source from our observing runs. An example of one such plot for the BL Lac object 3C 66A is shown in Fig. 2.3. This figure is a compilation of the lightcurves in the UBVRI bands obtained from our observations starting from the year 2005 until 2007. As can be seen from the figure, the source is in a flaring state during the end of 2007, in all the bands, as compared to rest of the previous years shown in the plot.

I have reduced part of the data obtained from these runs for various blazars, using IRAF. The reduction included the basic image reduction and photometry in order to obtain the calibrated fluxes of blazars and plot their respective lightcurves.

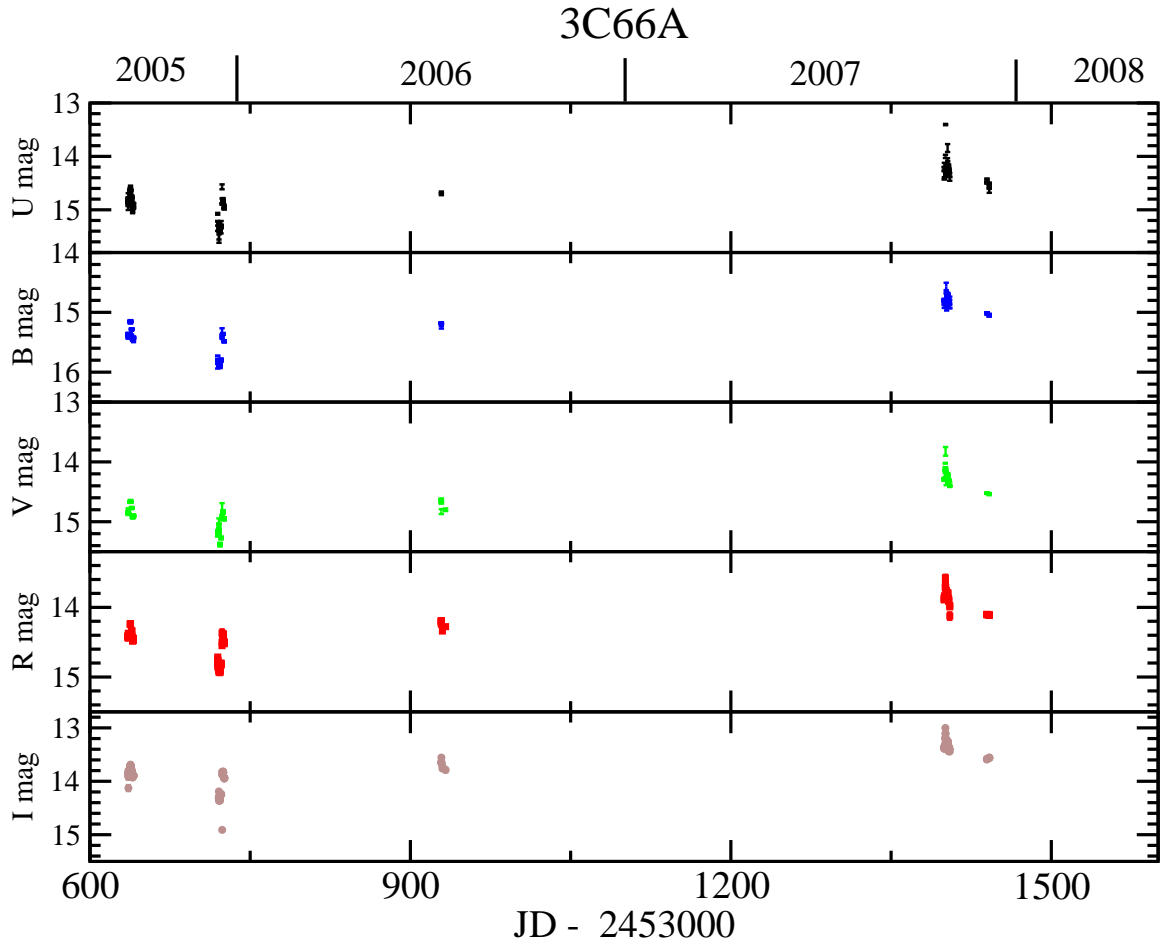


Figure 2.3: Lightcurves of 3C 66A obtained from the long-term blazar monitoring program being carried out at the 1.3 m McGraw-Hill telescope at the MDM observatory. The time of observations covered for this object is from September 2005 until end of 2007, as can be seen from the top x-axis. The y-axis indicate the magnitude value for 3C 66A in all the 5 optical bands. The bottom x-axis stands for the Julian date, which is a continuous count of days and fractions that have elapsed since the initial epoch. The initial epoch is defined as noon Universal Time (UT) Monday, January 1, 4713 BC in the proleptic Julian calendar [http://en.wikipedia.org/wiki/Julian\\_day](http://en.wikipedia.org/wiki/Julian_day). Credits for photo: Markus Böttcher <http://www.phy.ohiou.edu/~mboett/agn.html>

### 2.2.3 Gamma-Ray Burst Afterglows

Gamma-ray bursts (GRBs) are sudden and intense flashes of  $\gamma$ -rays, which for a few seconds go off in an otherwise fairly dark  $\gamma$ -ray sky. A GRB can outshine any other source of  $\gamma$ -rays in the sky, including the sun, at the time when the burst is on. GRBs are detected at a rate of about one per day from any direction in the sky. The nature of GRB progenitors and the primary driving mechanism of GRB explosions are still largely unknown, but the discovery of slowly fading x-ray, optical and radio afterglows of GRBs have given way to comprehend the mystery of GRBs. Studying afterglows in these frequencies helps us identify the location of a GRB event, measure its distance from us, identify the host galaxy, and confirm that GRBs are extragalactic events at cosmological distances of billions of light-years, just like some of the AGNs. The afterglows also help us understand the type of progenitor responsible for the burst and the afterglow emission in the form of jets. Many of the afterglows, discovered so far, have been linked to massive young stars, and in some cases, to the sudden collapse of a massive star's core in the form of supernovae. This linkage is called the hypernova model and was first suggested by Woosley and Paczyński (Woosley 1993). An artist's conception of this model is shown in Fig. 2.4. The other possible progenitors could be a merger of two neutron stars or a neutron star and a black hole. This material has been adapted from the website of Peter Mészáros (<http://www.astro.psu.edu/users/nnp/grbphys.html>).

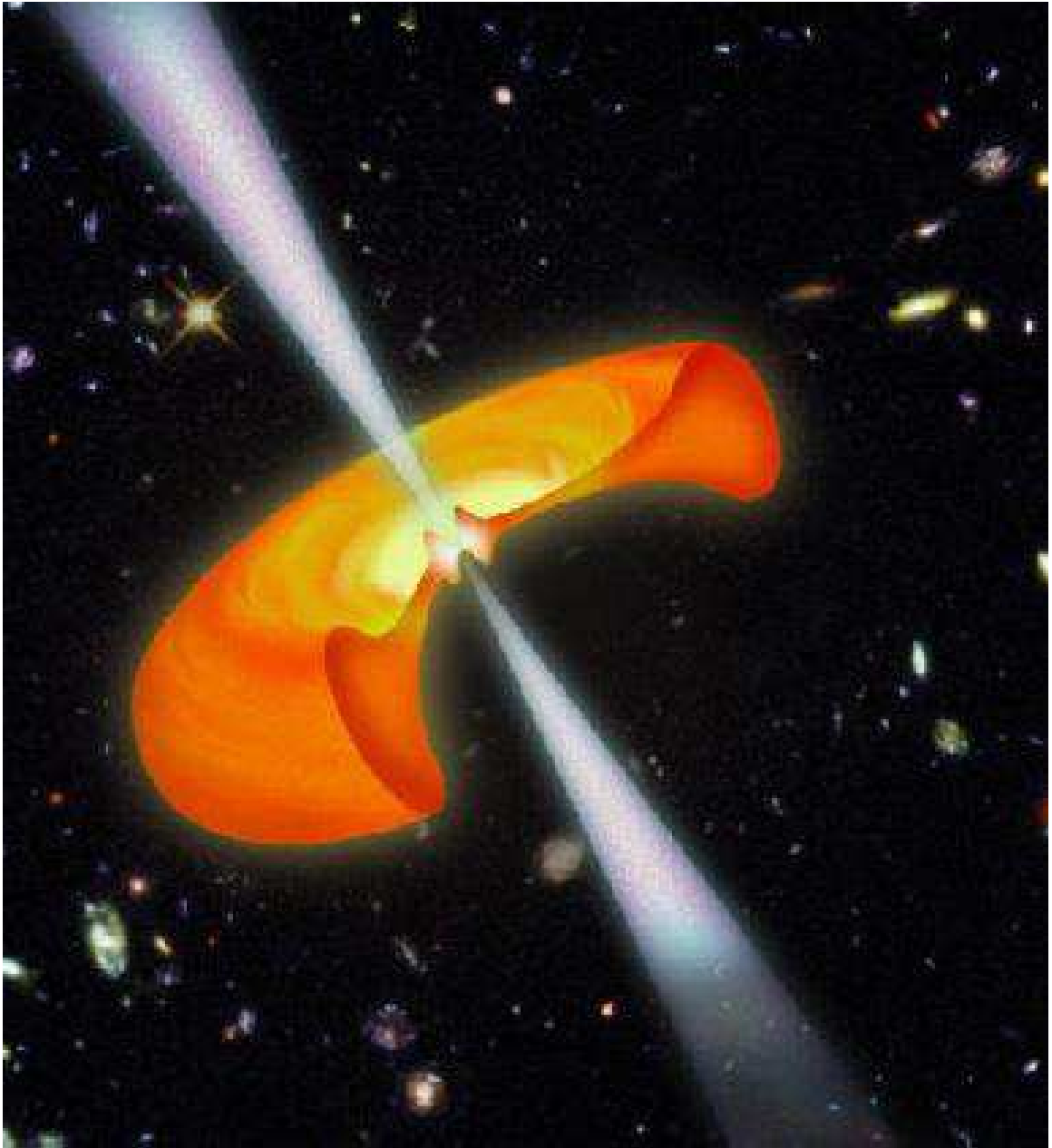


Figure 2.4: An artist's conception of a GRB in a hypernova model. The bright center harbors a black hole of several solar masses that rapidly accretes from the debris torus around it, shown in orange. This accretion feeds the assumed electron-positron-baryon or a magneto-hydrodynamic (MHD) jet that comes out of this central engine in a direction perpendicular to the plane of the accretion disk. Credit for the photo: <http://www.astro.psu.edu/users/nnp/grbphys.html>

Our group has successfully observed three GRB afterglows in the past, and I had contributed toward the observations and basic data-reduction for two of them, GRB 050502A and GRB 051221A (Yost et al. 2006; Böttcher and Joshi 2005; Mirabal et al. 2005). For GRB 050502A, we followed its afterglow from  $\sim 1.8$  to  $\sim 8.2$  hours after the burst in 21 R-band exposure frames. The exposure time for the frames varied from  $\sim 600$  - 1800 seconds. I have also combined these 21 frames, after carrying out basic data reduction, into an animation of the fading afterglow as observed by us. The animation can be found on the website,

<http://www.manasvita.com/grb.html>

We followed the optical afterglow of GRB 051221A from  $\sim 2.1$  to  $\sim 2.6$  hours after the burst in 3 R-band exposure frames, each lasting for  $\sim 600$  seconds. In this case, we could detect the host galaxy, and provided the apparent magnitude of the GRB afterglow in the R band. In order to do that, I carried out the basic data reduction of all the three frames and relative photometry of the source with respect to six comparison stars. Only those comparison stars were chosen that were present in our field of view at the time of observation and their corresponding calibrated R-band magnitudes were obtained from an interactive sky atlas, called ALADIN (<http://aladin.u-strasbg.fr/>).

## 2.3 Summary

I have been a part of the long-term ongoing project that was designed to monitor the optical spectral variability of a sample of  $\gamma$ -ray loud blazars on various time scales and carry out follow-up observations of the afterglows of GRBs, should the occasion arise. In this project, I have been able to observe  $\sim 10$  blazars and 2 GRB afterglows in the 6 one-week-long observing runs that were carried out at the 1.3 m McGraw-Hill telescope at MDM observatory. These observing efforts have resulted in a number of publications, of which I have been an author for some of them ([Raiteri et al. 2008](#); [Böttcher et al. 2007](#); [Ciprini et al. 2007](#); [Akerlof et al. 2006](#); [Yost et al. 2006](#); [Böttcher and Joshi 2005](#); [Mirabal et al. 2005](#)). Overall, being a part of this project has helped me gain a better understanding of observational astronomy and how it can be linked to theory and modeling of the physical processes of a source.

## CHAPTER 3

# The BL Lac object 3C 66A

### 3.1 Introduction

3C 66A is an LBL, with a redshift of  $z = 0.444$  although this determination is precise but not accurate (Bramel et al. 2005; Finke et al. 2008). It is generally observed as a point source, with no indication of the host galaxy. Although Wurtz et al. (1996) had resolved its host galaxy marginally having a magnitude of 19.0 in the R band they could not determine its shape. 3C 66A has exhibited rapid microvariability at optical and near infrared in the past and has been suggested as a promising candidate for detection by the new generation of atmospheric Čerenkov telescope facilities like HESS, MAGIC or VERITAS (Costamante and Ghisellini 2002). Detection of LBLs in the  $\gamma$ -ray energy range of  $\sim 40 - 100$  GeV provides an opportunity to probe the intrinsic high-energy cutoff of their spectral energy distributions (SEDs). This is because, at such energies, the  $\gamma - \gamma$  absorption due to the intergalactic infrared background is still expected to be small (de Jager and Stecker 2002). The information regarding the intrinsic high-energy cutoff of the SED plays an important role in determining the contribution of the inverse Compton (IC) processes in producing the high-energy component of the SED and also in understanding the environment around the jet of the source. This is important because, LBLs mark the transition

between FSRQs and HBLs in the controversial blazar sequence, and hence can shed light on the environment around the jets of blazars, in general.

The low-energy component of 3C 66A is known to peak in the infrared (IR) - ultraviolet (UV) region whereas the high-energy component generally peaks at multi MeV - GeV energies. 3C 66A was first identified as a blazar in an optical observation in 1974 (Wills and Wills 1974). Since then, the object has been observed in all wavebands (radio, IR, optical, X-ray,  $\gamma$ -ray). Intensive two-year optical and IR observations of 3C 66A by Takalo et al. (1996) revealed evidence for rapid microvariability with a 0.2 magnitude decline in the brightness in 6 hours. Microvariability in the source was also observed by Carini and Miller (1991) and de Diego et al. (1997) in the IR band on a time scale of a few hours although other similar efforts could not detect that feature in 3C 66A (e.g., Takalo et al. 1992; Xie et al. 1992). The source has exhibited large-amplitude variation in the soft X-ray regime ( $\lesssim 1$  keV to  $\sim 10$  keV) as well (see e.g., Worrall and Wilkes 1990; Sambruna et al. 1994; Fossati et al. 1998; Croston et al. 2003; Perri et al. 2003). 3C 66A has also been detected by the space-based  $\gamma$ -ray telescope, Energetic Gamma Ray Experiment Telescope (EGRET), on several occasions in the  $\gamma$ -ray energy range ( $> 100$  MeV) (Hartman et al. 1999). Despite the considerable amount of observational efforts spent on 3C 66A, the multiwavelength SED and correlated broadband spectral variability behaviour of this object have been very poorly understood. For this reason, Böttcher et al. (2005) organized an intensive simultaneous multiwavelength campaign to observe this object

from July 2003 through April 2004, with the core campaign period from September - December 2003. The simultaneous multiwavelength campaigns have the advantage of providing well-sampled continuous data on an object, which help constrain theoretical models geared towards understanding the broadband SED and spectral variability of the object.

My very first project has been on the BL LAC object 3C 66A. I have carried out extensive theoretical analysis of this object in order to understand the interplay between various physical processes responsible for producing its observed SED. In Section 3.2 of this chapter, I will describe, briefly, the observational results obtained from the campaign and the need to theoretically understand the observations. The time-dependent leptonic jet model used to reproduce the observed SED and simultaneously model the optical spectral variability observed during the multiwavelength campaign is discussed in Section 3.3 of the chapter. The parameters that were used to model the observed results are described in Section 3.4. Results of modeling and VHE  $\gamma$ -ray predictions are described in Section 3.5 and the chapter concludes with Section 3.6.

## 3.2 3C 66A Observations

The BL Lac object 3C 66A was the target of an intensive multiwavelength campaign organized to monitor the source continuously and simultaneously during the core campaign period of September - December 2003. The entire campaign lasted

for almost 10 months from July 2003 until April 2004. The object was observed by the WEBT-ENIGMA collaboration in the radio, IR, and optical regimes. In the X-rays, the object was observed by the X-ray telescope RXTE (Rossi X-ray Timing Explorer). In the VHE  $\gamma$ -ray regime, the object was observed by the ground-based  $\gamma$ -ray telescopes STACEE (Solar Tower Air Čerenkov Effect Experiment) and Whipple. In addition to these telescopes, the object was also observed 9 times during the entire campaign period by a Very Large Baseline Array (VLBA) of 10 radio telescopes. These telescopes are spread all across the United States starting from Mauna Kea, Hawaii to St. Croix in the U.S. Virgin Islands.

In the radio, the object was observed from 2.3 -  $86 \times 10^9$  Hz (GHz). In the IR, the object was observed at near-infrared wavelengths in the bands J, H, and K. The object was observed in all 5 optical bands (U, B, V, R, and I) and was most densely sampled in the R- and B- band due to the observing strategy laid out by the WEBT-ENIGMA collaboration to observe 3C 66A. In the X-ray regime, photons in the energy range of 3 - 10 keV (soft X-rays) were extracted using the RXTE's Proportional Counter Array (PCA). PCA is an array of 5 proportional counters (detectors) that span an energy range of 2 - 60 keV (<http://heasarc.gsfc.nasa.gov/docs/xte/PCA.html>). At VHE  $\gamma$ -rays, observations were carried out and an upper limit on the energy of photons with  $E > 100$  GeV was obtained. For a detailed description of the observing strategy of 3C 66A in all wavebands, see [Böttcher et al. \(2005\)](#). In conjunction with the campaign, I carried out a literature survey on 3C 66A to determine the historical

flux levels displayed by the source as a guide to new observations. I had a significant role in combining disparate data sets from different optical observatories and placing them on a common photometric scale, and de-reddening the optical data to obtain the intrinsic broadband spectral shape. The reddening of the optical data is a result of Galactic interstellar dust absorption.

As described in [Böttcher et al. \(2005\)](#), the object exhibited only moderate variability in the IR bands with variations in the magnitude (mag) on the order of  $\Delta\text{mag} \sim 0.2$  within  $\sim$  a few days in all three J, H, and K bands. 3C 66A exhibited several outbursts in the optical. The variations were on the order of  $\Delta\text{mag} \sim 0.3\text{-}0.5$  over a timescale of several days. A plot of the light curves at all optical bands is shown in [Fig. 3.1](#). The figure illustrates the variability observed in the object during the entire campaign period in all optical bands. As can be seen from the figure, the various optical bands seem to trace each other very well without a significant time lag between different bands although not much can be said about the U band lightcurve as that was the most sparsely sampled one. The object reached its maximum brightness on Feb. 18, 2004 with the R-band magnitude reaching  $\approx 13.4$ . This brightening was followed by a sharp decline by  $\Delta R \sim 0.4$  mag within  $\sim 15$  days.

We also found evidence for intraday microvariability with a variation in the R-band magnitude to be  $\Delta R \sim 0.05$  mag over a time period of  $\sim 2$  hours. The RXTE PCA data indicated a transition between the low-energy component and the high-energy component at photon energies of  $\gtrsim 10$  keV, in the soft X-ray regime. No

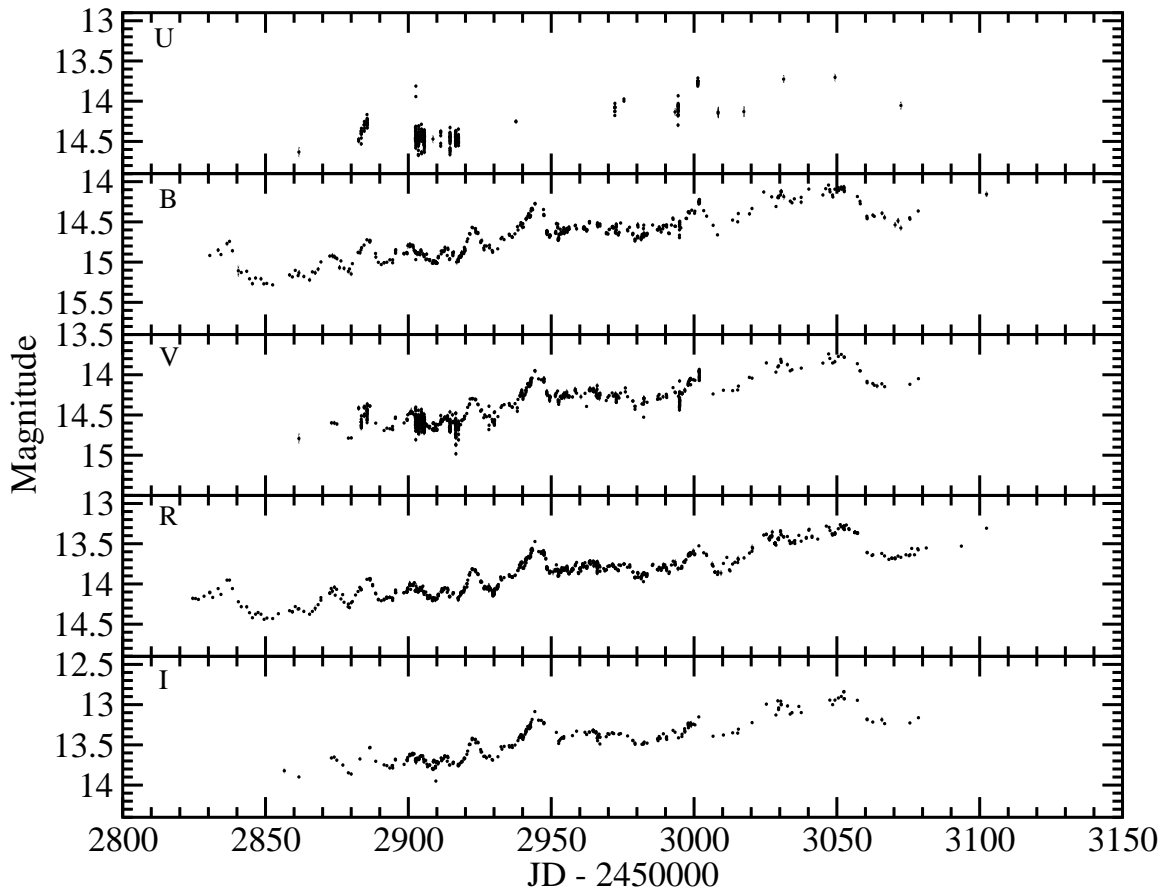


Figure 3.1: Observed lightcurves of 3C 66A in the optical U, B, V, R, and I bands over the entire duration of the campaign (Böttcher et al. 2005).

variability in either the flux or the spectral shape of the source in the X-ray band could be detected by RXTE. In the VHE  $\gamma$ -ray regime, STACEE provided an upper limit at  $E_\gamma \gtrsim 150$  GeV whereas an upper limit at  $E_\gamma > 390$  GeV resulted from simultaneous observations by the Whipple telescope of the VERITAS collaboration. The broadband SED of 3C 66A suggested that the low-energy component peaked in the optical. As far as the high-energy component of the SED was concerned, a precise statement could not be made regarding the  $\gamma$ -ray emission level during

the campaign owing to the lack of simultaneous GeV  $\gamma$ -ray coverage and of a firm detection at  $> 100$  GeV. Figure 3.2 shows the observed SED of 3C 66A obtained from our campaign. All the non-contemporaneous data are indicated by dotted curves and are shown for comparison along with the archival year from which they are taken. EINSTEIN, ROSAT, EXOSAT, BeppoSAX, and XMM-Newton are all X-ray telescopes. EGRET was a space-based  $\gamma$ -ray telescope on board the Compton Gamma Ray Observatory (CGRO) that covered an energy range of 30 MeV - 10 GeV. CGRO was de-orbited in the year 2000 and has now been followed by the space-based Italian  $\gamma$ -ray observatory, Astrorivelatore Gamma ad Immagini LEggero (AGILE), and NASA initiated Gamma-ray Space Telescope, Fermi. Fermi will study the cosmos in the energy range 10 keV to  $> 300$  GeV and is 30 times more sensitive than EGRET.

As described earlier, only moderate variability in the IR and no variability in the X-ray band was observed, hence, we concentrated only on the optical spectral variability as indicated by a change in the magnitude in the optical band. In particular, as the sampling was good for the B- and R-bands, we focused on the variation in the magnitudes of these two optical bands with time. This was carried out by plotting the color-magnitude diagram for the object in the two bands. A color-magnitude diagram is a plot of the magnitude of the object in a particular waveband and the difference of the magnitudes of the object in the same waveband and a comparison waveband. This diagram is then used to investigate any kind of correlation that

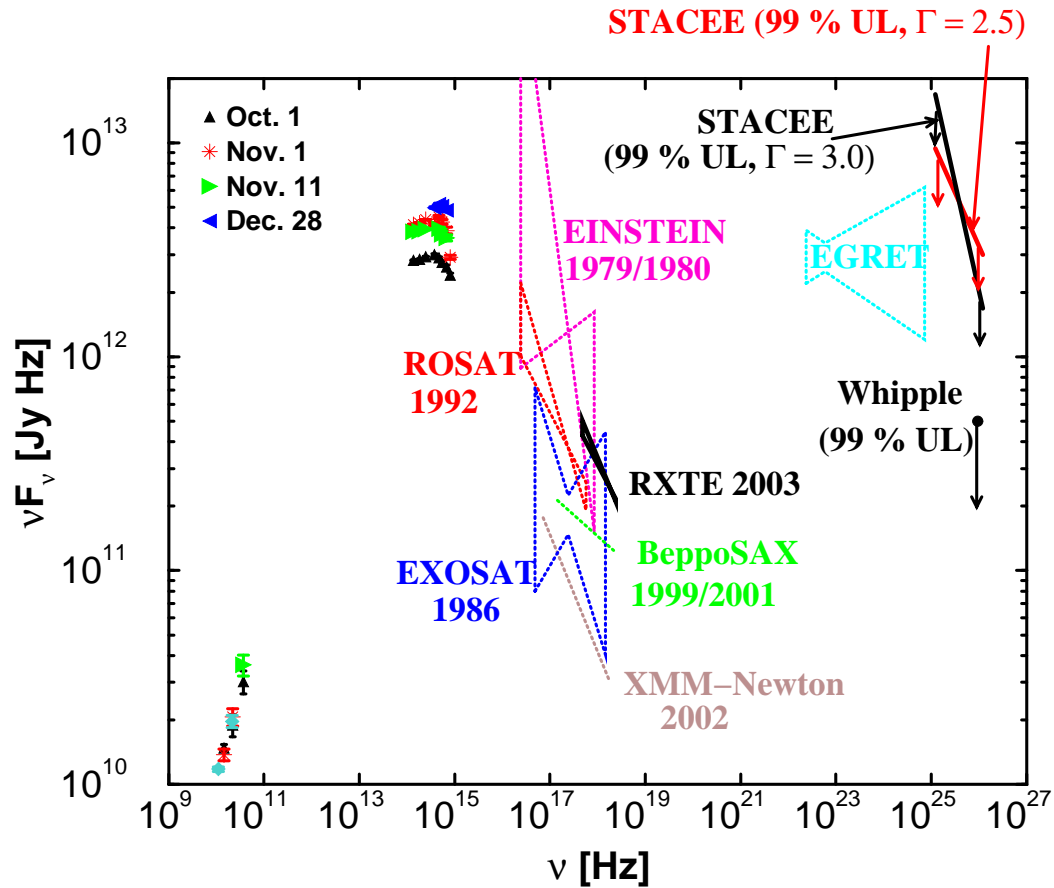


Figure 3.2: Observed SED of 3C 66A at various epochs during the core campaign period in 2003. The turquoise diamonds indicate the average of radio observations from Oct. 11 and 14, 2003. The hard X-ray spectrum labelled “RXTE 2003” is the result of a power-law fit to the RXTE PCA data and denotes the time-averaged X-ray data points from the entire campaign. All the dotted curves indicate archival data and are there for comparison. The historical average of the 5 EGRET pointings is also included to provide a guideline for our simulated VHE emission (Böttcher et al. 2005). A Jansky (Jy) is a unit of specific flux and is defined as  $1 \text{ Jy} = 10^{-23} \text{ ergs s}^{-1} \text{ cm}^{-2} \text{ Hz}^{-1}$  (Peterson 1997). Thus,  $1 \text{ Jy Hz} = 10^{-23} \text{ ergs s}^{-1} \text{ cm}^{-2}$ .

might exist between the two optical bands as far as variability is concerned. The color-magnitude diagram for the B- and R-band is shown in Fig. 3.3. As shown in the figure, the object tends to get brighter in both the bands while getting spectrally

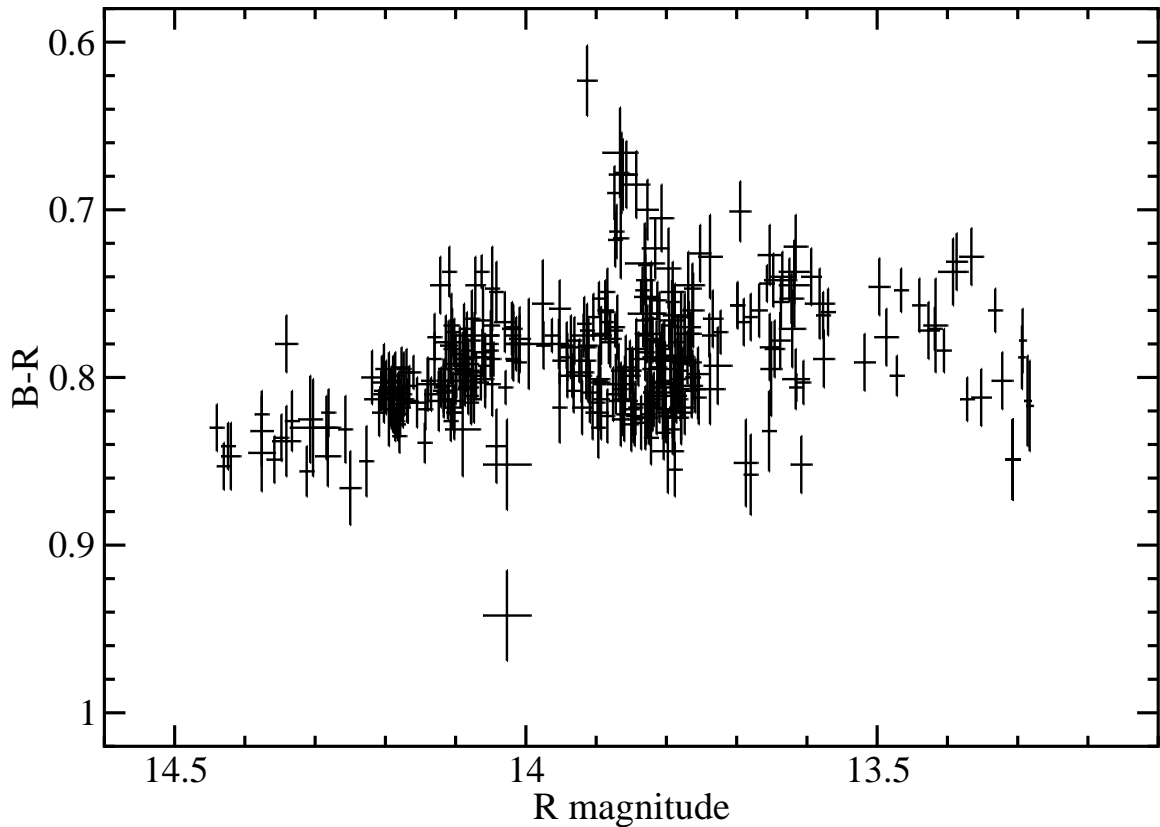


Figure 3.3: Color- magnitude or hardness-intensity diagram for the B- and R-bands for the complete data set over the entire campaign period. A positive correlation seems to be present between the hardness and intensity at low brightness,  $R \gtrsim 14.0$ , but no such clear correlation can be seen at higher flux states (Böttcher et al. 2005).

harder in B - R, for low flux states of the R-band ( $R \gtrsim 14.0$ ). On the other hand, no clear correlation could be found for high flux states of the R-band ( $R \lesssim 14.0$ ).

A few questions had arisen from the observational results of 3C 66A. How was the observed OVP originating that was responsible for the B - R correlation at low fluxes? What could be said about the spectral variability pattern at higher energies that could not be observed? Where does the high-energy component peaks, and what predictions could be made that would assist in future VHE observations of the source?

Thus, a theoretical understanding of the interplay between various physical processes responsible for producing the observed SED was essential to answer such questions. In order to obtain a detailed description of the various radiative processes in 3C 66A, I used the time-dependent radiation transfer code of [Böttcher and Chiang \(2002\)](#) to develop a model that reproduced the broadband SED and the observed OVP.

### 3.3 Time-dependent Leptonic Jet Model

In this model, a population of ultrarelativistic non-thermal electrons and positrons is injected into a spherical emitting volume (the “blob”). The radius of the blob in its rest frame (comoving frame) is  $R_b$  and the particles are injected into the blob having a single power-law distribution with a spectral index,  $q$ . Since the positrons lose equal amount of energy as the electrons through the same radiative loss mechanisms, I will not distinguish between them through the rest of this chapter. The evolution of the electron and photon population is followed inside this single blob in a time-dependent manner and along the radial direction of the blob as the blob travels further out along the jet. The photon and electron density is considered to be homogeneous inside the emitting region. [Figure 3.4](#) delineates the schematic of the jet coming out of the central engine and the blob moving relativistically out along the jet, as seen by an observer from the side standing in a stationary frame of reference. The blob will appear Lorentz contracted to this stationary observer.

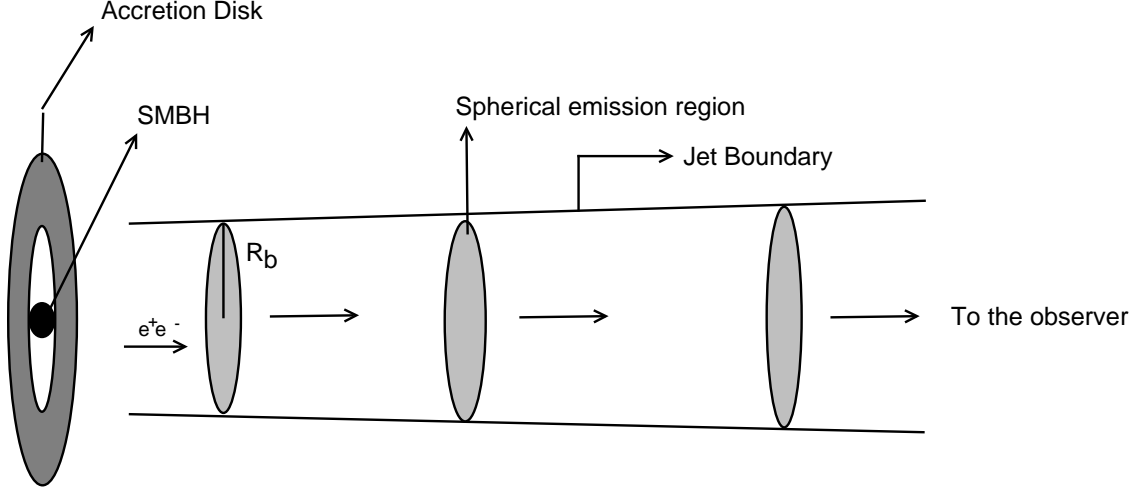


Figure 3.4: Schematic diagram of the relativistic outflow (jet) coming out of the central engine of a blazar. Ultrarelativistic electrons are injected into the spherical emission region at a time-dependent rate as the blob moves outwards along the jet.

The low- and high-energy cutoffs of the co-moving electron distribution are  $\gamma_1$  and  $\gamma_2$ , respectively. The comoving injection function is given by,  $Q_e^{\text{inj}}(\gamma) = Q_0^{\text{inj}}(t)\gamma^{-q}$  for  $\gamma_1 \leq \gamma \leq \gamma_2$ , where  $Q_0^{\text{inj}}(t)$  ( $\text{cm}^{-3}\text{s}^{-1}$ ) is the normalization and is given by

$$Q_0^{\text{inj}}(t) = \begin{cases} \frac{L_{\text{inj}}(t)(2-q)}{V'_b m_e c^2 (\gamma_2^{2-q} - \gamma_1^{2-q})} & \text{if } q \neq 2 \\ \frac{L_{\text{inj}}(t)}{V'_b m_e c^2 \ln(\gamma_2/\gamma_1)} & \text{if } q = 2 . \end{cases} \quad (3.1)$$

Above,  $L_{\text{inj}}$  specifies the power of the injected pair population and  $V'_b$  is the blob volume in the comoving frame.

The randomly oriented magnetic field  $B$  has uniform strength throughout the blob and is determined by an equipartition parameter  $\epsilon_B \equiv U_B/U_e$  (in the comoving frame). Here,  $U_B = B^2/8\pi$  is the magnetic field energy density and  $U_e$  is the electron

energy density. The initial injection of the electron population into the blob takes place at a height  $z_0$  above the plane of the central engine. The blob moves with a relativistic speed of  $v/c = \beta_\Gamma = (1 - 1/\Gamma^2)^{1/2}$  along the jet, where  $\Gamma$  is the bulk Lorentz factor of the blob. The jet is directed at an angle  $\theta_{obs}$  with respect to our line of sight.

As the blob moves outward along the jet, the injected particles continuously lose their energy via radiative losses. These losses occur by synchrotron emission, Compton upscattering of synchrotron photons (SSC), and Compton upscattering of external photons (EC). The external seed photons are comprised of UV and soft X-ray photons coming from the disk and entering the jet directly (Dermer et al. 1992; Dermer and Schlickeiser 1993) and/or after getting reprocessed in the BLR or other circumnuclear material (Sikora et al. 1994; Dermer et al. 1997).

The low-energy component of the SED is due to synchrotron radiation. Synchrotron radiation is the result of acceleration of charged particles, having relativistic velocities, in the presence of a magnetic field. The synchrotron power, averaged over all pitch angles (angle between the field and the velocity vector of the charged particles), resulting from a single electron is given by (Rybicki and Lightman 1979)

$$P_{\text{syn}} = \frac{4}{3} \sigma_T c \beta^2 \gamma^2 U_B , \quad (3.2)$$

where  $\sigma_T = 6.65 \times 10^{-25} \text{cm}^2$  is the Thomson cross section, and  $\beta = v/c$  is the speed of the relativistic electron and is close to 1 for ultra-relativistic particles. The high-

energy component, in leptonic models, arises due to inverse Compton (IC) scattering of photons. In this case, an incoming photon gets scattered by a single electron, moving with ultrarelativistic speed and in the process gains energy from the electron.

The IC power for a single electron is given by (Rybicki and Lightman 1979),

$$P_{\text{IC}} = \frac{4}{3} \sigma_{\text{T}} c \beta^2 \gamma^2 U_{\text{ph}} , \quad (3.3)$$

where  $U_{\text{ph}}$  is the seed photon energy density available for scattering.

The time-dependent evolution of the electron and photon populations in the emission region are, respectively, given by

$$\frac{\partial n_e(\gamma, t)}{\partial t} = -\frac{\partial}{\partial \gamma} \left[ \left( \frac{d\gamma}{dt} \right)_{\text{loss}} n_e(\gamma, t) \right] + Q_e(\gamma, t) - \frac{n_e(\gamma, t)}{t_{\text{e,esc}}} \quad (3.4)$$

and

$$\frac{\partial n_{\text{ph}}(\epsilon, t)}{\partial t} = \dot{n}_{\text{ph,em}}(\epsilon, t) - \dot{n}_{\text{ph,abs}}(\epsilon, t) - \frac{n_{\text{ph}}(\epsilon, t)}{t_{\text{ph,esc}}} . \quad (3.5)$$

Here,  $(d\gamma/dt)_{\text{loss}}$  is the radiative energy loss rate, due to synchrotron, SSC and/or EC emission, for the electrons. The quantity  $Q_e(\gamma, t)$  is the sum of external injection and intrinsic  $\gamma - \gamma$  pair production rate and  $t_{\text{e,esc}}$  is the electron escape time scale. The quantities  $\dot{n}_{\text{ph,em}}(\epsilon, t)$  and  $\dot{n}_{\text{ph,abs}}(\epsilon, t)$  are the photon emission and absorption rates, and  $t_{\text{ph,esc}} = (3/4)R_b/c$  is the photon escape timescale. The time-dependent evolution of the electron and photon population inside the blob is followed and radiative en-

ergy loss rates as well as photon emissivities are calculated using the time-dependent radiation transfer code of [Böttcher and Chiang \(2002\)](#).

For the purposes of my study, I am using the radiation transfer code to follow the evolution of the emission region out to sub-pc scales only. As a result, only the early phase of the blob evolution has been simulated during which high energy emission is produced. Since the radiative cooling is strongly dominant over adiabatic cooling during this phase and the emission region is highly optically thick out to GHz radio frequencies, the simulated radio flux is well below the actual radio data. I do not simulate the phase of the jet components in which they are expected to gradually become transparent to radio frequencies as that would require the introduction of several additional, poorly constrained parameters.

### 3.4 Model Parameters

I used the multiwavelength data from the 2003-2004 campaign to estimate key physical properties of the source by employing fundamental physical arguments. This analysis included using the observed minimum variability timescale of 2 hours observed in the R-band to estimate the size of the blob. Also, I used the location of the low-energy SED maximum to estimate the comoving magnetic field and thus, estimate the synchrotron cooling timescale of electrons in the observer's frame ([Böttcher et al. 2005](#)). These parameters describe the sub-parsec scale outflow, which is closest to the central engine. The resulting values served as crucial input for detailed numer-

ical models for the blazar source. The model independent parameters that were used to develop an initial set of input parameters are:

$$\begin{aligned}
 D &\approx 15 \\
 R_b &\approx 3.3 \times 10^{15} \text{ cm} \\
 B &\approx 2.9 \epsilon_B^{2/7} \text{ G} \\
 \gamma_1 &\approx 3.1 \times 10^3 \\
 \gamma_2 &\approx 1.5 \times 10^5 \\
 p &\approx 4
 \end{aligned} \tag{3.6}$$

Here,  $p$  is the equilibrium spectral index that determines the optical synchrotron spectrum and  $p = q + 1$  for strongly cooled electrons. I modified the initial set of parameters to reproduce the quiescent as well as the flaring state of 3C 66A. I carried out approximately 350 simulations to study the effects of varying various parameters, such as  $\gamma_1$ ,  $\gamma_2$ ,  $q$ ,  $B$  and  $\Gamma$ , on the resulting broadband spectra and light curves. The set of model parameters that provided a satisfactory fit to the quiescent state of 3C 66A involved a value of the Doppler boosting factor,  $D \equiv \Gamma = 24$  and a viewing angle of  $\theta_{\text{obs}} = 2.4^\circ$ . I chose these parameters on the basis of VLBA observations that provided limits on the superluminal motion and indicated bending of the jet towards our line of sight. As a result of this bending, a smaller viewing angle and a higher Doppler boosting of the emission region, at sub-pc scales, was chosen as compared to the values inferred from the superluminal measurements for the emission region with

a  $\beta_{\text{app}} \leq 20.1$  and  $\theta_{\text{obs}} \leq 27.2$  deg on parsec scales (Jorstad et al. 2005; Böttcher et al. 2005). Here  $\beta_{\text{app}}$  refer to the transverse velocity of the source. I carried out the fitting of the SED both in the quiescent as well as the flaring state of 3C 66A in such a way that the simulated quiescent state does not overpredict the X-ray photon flux. This is because the X-ray photons are expected to be dominated by the flaring episodes. For simulating the flaring state, I made sure that the resulting time-averaged spectrum passes through the observed time-averaged optical as well as X-ray data points. The various simulations were carried out by adjusting the time profiles and the values of individual parameters, such as,  $\gamma_1$ ,  $\gamma_2$  and  $q$  between the values for quiescent and flaring states. A value of  $\gamma_1 = 2.1 \times 10^3$ ,  $\gamma_2 = 4.5 \times 10^4$  and  $q = 2.4$  provided a satisfactory fit to the flaring state. I kept  $\epsilon_{rmB}$  constant so that the magnetic field value changes according to the evolving electron energy density value as determined by equation 3.4. I used the flux upper limits at multi-GeV - TeV energies to get upper limits on the respective parameters governing the EC component. The various model parameters used to simulate the two states of 3C 66A are listed in Table 3.1 (Joshi and Böttcher 2007).

Fits 1 and 2 of Table 3.1 correspond to a pure SSC emission process, as far as the high-energy component is concerned, by artificially setting  $L_D = 0$ , where  $L_D$  is the bolometric disk luminosity. Fit 1 delineates the parameters for the simulation of the quiescent state only whereas Fit 2 refers to the combined quiescent + flaring state of 3C 66A. Fit 3 of Table 3.1 refers to an EC+SSC case with  $L_D = 1.0 \times 10^{45}$  ergs s<sup>-1</sup>

Table 3.1. Model Parameters used to reproduce the quiescent and flaring state of 3C 66A as shown in Figures 3.5 and 3.6, respectively.

Fit	$L_{inj}$ [ $10^{41}$ ergs/s]	$\gamma_1$ [ $10^3$ ]	$\gamma_2$ [ $10^4$ ]	q	Profile	B [G]	$\Gamma$	$R_b$ [ $10^{15}$ cm]	$\theta_{obs}$ [deg]	$\tau_{T,BLR}$
1	2.7	1.8	3.0	3.1	—	2.4	24	3.59	2.4	0
2	8.0	2.1	4.5	2.4	Gaussian	2.8	24	3.59	2.4	0
3	8.0	2.1	4.5	2.4	Gaussian	2.8	24	3.59	2.4	0.3

Note. — The  $L_{inj}$  is the luminosity with which electron population is injected into the blob,  $\gamma_{1,2}$  are the low- and high-energy cutoffs of electron injection spectrum, and q is the particle spectral index. Profile stands for the flare profile used to reproduce the optical variability pattern, the magnetic field B is the equipartition value.  $\Gamma$  is the bulk Lorentz factor,  $R_b$  is the comoving radius of the blob,  $\theta_{obs}$  is the viewing angle and  $\tau_{T,BLR}$  is the radial Thomson depth of the BLR.

and is shown in Figure 3.13. For the fit 3 simulation, I chose the value of  $L_D$  such that it is more than the value of the jet luminosity used in the simulations and at the same time does not produce a blue bump in the simulated SED. The blue bump corresponds to the thermal emission of the disk that is sometimes seen in the SED of a blazar. In order to assess the possible effect of EC emission in 3C66A, I had first determined an upper limit to the optical depth of the BLR using XSTAR. The optical depth of a medium is the measurement of its opaqueness or transparency towards radiation. A medium is said to be optically thick or opaque if its optical depth  $\tau > 1$ , and optically thin if  $\tau < 1$ , where  $\tau$  has been integrated along a typical path through the medium (Rybicki and Lightman 1979). XSTAR is a software that

returns the ionization balance, temperature, opacity, emitted lines (e.g.,  $H_\alpha$ ,  $H_\beta$ ) and continuum fluxes of photoionized gases. For this simulation, I had modeled the BLR as a spherical shell with  $r_{\text{BLR,in}} = 0.045$  pc and  $r_{\text{BLR,out}} = 0.050$  pc. The  $r_{\text{BLR,in}}$  and  $r_{\text{BLR,out}}$  stand for the inner and outer radii of the BLR. A Thomson optical depth of 0.3 for the BLR was chosen as a reasonable upper limit such that the line emission is weak enough to be consistent with the observed featureless continuum.

I had reproduced the flaring above the quiescent state of 3C 66A using a flaring profile for the electron injection power ( $L_{\text{inj}}(t)$ ) that was Gaussian in time (see Figure 3.8), and is given by

$$L_{\text{inj}}(t) = L_{\text{inj}}^{\text{qu}}(t) + \frac{(L_{\text{inj}}^{\text{fl}} - L_{\text{inj}}^{\text{qu}})}{\exp\left[\frac{(z-r_c)^2}{2\sigma^2}\right]}. \quad (3.7)$$

Here, qu and fl stand for the quiescent and flaring state respectively,  $z$  determines the position of the emission region in the jet at time  $t$ ,  $r_c$  indicates the position of the center of the simulated flare and  $\sigma$  stands for the Gaussian width of the flare.

As described earlier, parameters such as  $\gamma_1$ ,  $\gamma_2$ , and  $q$  were also changed accordingly. In order to simulate the observed optical flare, I allowed the system to first come to an equilibrium and once the equilibrium was set, I introduced the flare with a Gaussian width,  $\sigma$ , corresponding to 14 days in the observer's frame. Although the flare was introduced in order to simulate the observed major optical outbursts lasting for 10 days, the choice of 14 days for the Gaussian width was made such that the width of the simulated flare matches that of the observed flare. The parameter  $r_c$  was

adjusted such that the centre of the simulated flare aligns with that of the observed one and the value of  $L_{\text{inj}}$  was varied between  $L_{\text{inj}}^{\text{qu}}$  and  $L_{\text{inj}}^{\text{fl}}$  such that the peak of the simulated flare matches that of the observed one.

### 3.5 Results

Figures 3.5 and 3.6, respectively, show the simulated SED of 3C 66A, for both the quiescent and flaring states observed during the campaign period. The quiescent state is a reproduction of the state observed around 1st October 2003 whereas the flaring state is the reproduction of a generic 10 day flaring period that corresponds to the timescale of several of major outbursts observed during the campaign.

Figure 3.7 shows the simulated time-averaged spectrum of 3C 66A for fit 2. As can be seen from the figure, the low-energy component of the spectrum passes through the time-averaged optical data points. The high energy end of the synchrotron component passes through the time-averaged X-ray data indicating the dominance of synchrotron emission in the production of such photons in case of flaring. For hard X-ray photons with energy beyond 10-12 keV, the data are less reliable due to low count rates and possible source confusion with a nearby radio galaxy, 3C 66B. The transition from synchrotron to SSC emission takes place at  $\geq 7$  keV, indicating that SSC mechanism is responsible for producing hard X-ray photons. Also, the presence of this component cannot be suppressed because in order to suppress it the population of seed photons would have to be diluted, which can be done by increasing the size of the emission

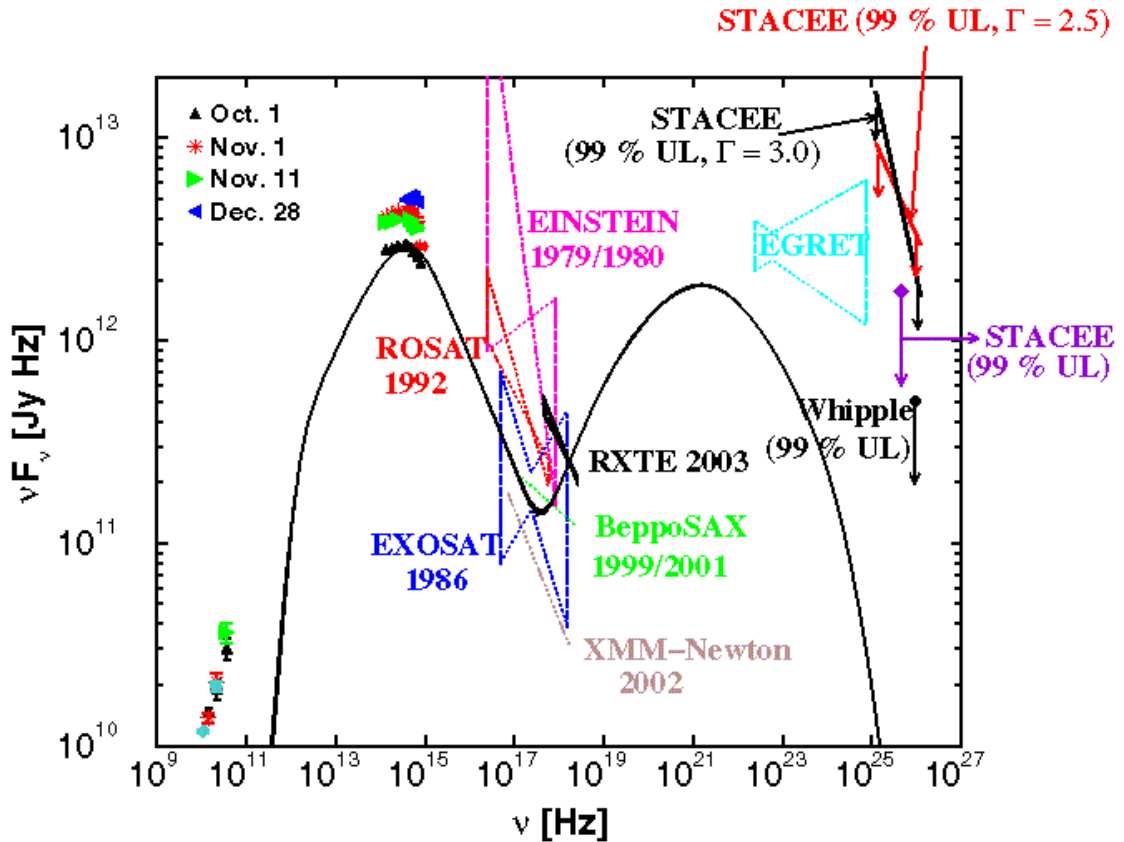


Figure 3.5: Simulation of the quiescent state of 3C 66A observed around October 1st 2003 (Joshi and Böttcher 2007). This state was reproduced using parameters that do not overpredict the X-ray photon flux. The black colored solid line indicates the instantaneous spectrum generated by the simulation after the system (blob + injected electron population) attains equilibrium. The low-energy component peaks in the optical at  $\nu_{\text{syn}}^{\text{peak}} \approx 4.8 \times 10^{14}$  Hz whereas the high-energy SSC component peaks in the MeV regime at  $\nu_{\text{SSC}}^{\text{peak}} \approx 1.6 \times 10^{21}$  Hz. The synchrotron cooling timescale in the observer's frame is  $\approx 1.2$  hours, which is on the order of observed minimum optical variability timescale of 2 hours. The diamond shaped STACEE upper limit is a new addition and is provided by Lindner (2007).

region. But the size of the emission region cannot be increased any further because of the strict constraint on the maximum size of the blob that comes from the observed minimum variability timescale in the optical region, which is 2 hours. Hence, the

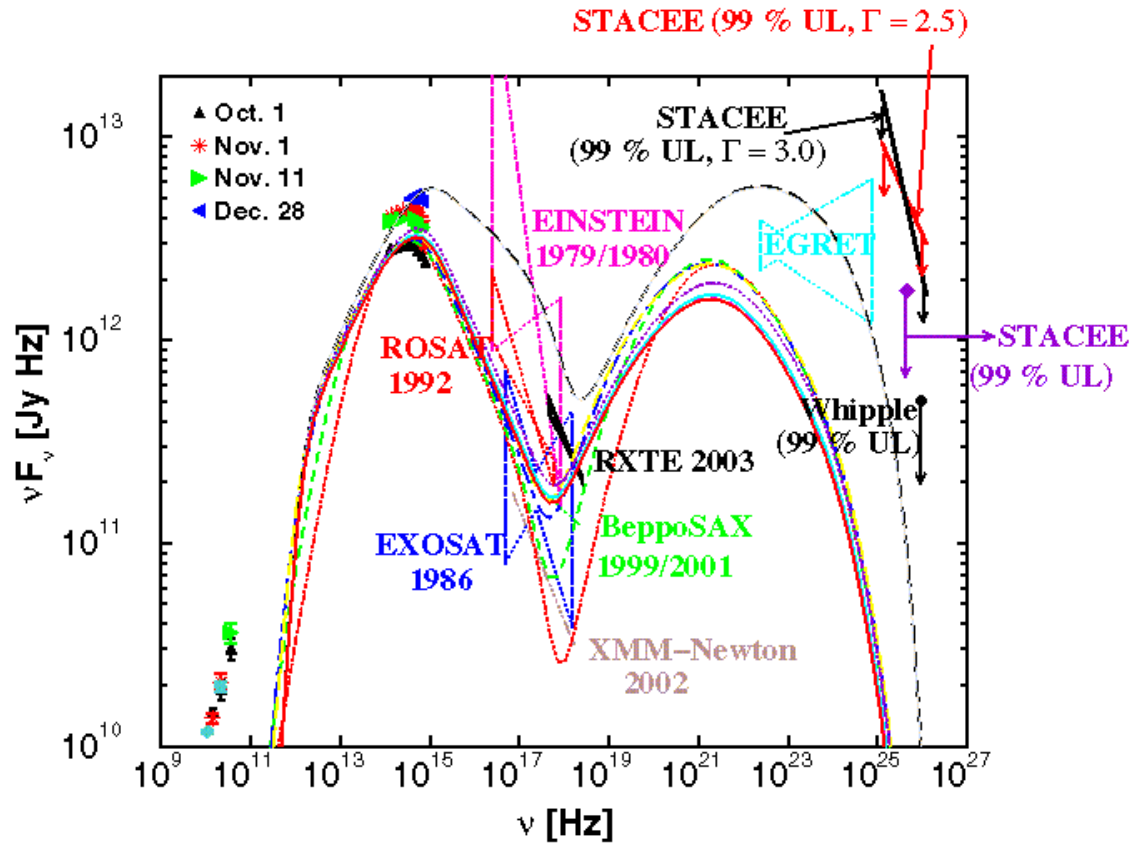


Figure 3.6: Simulation of the flaring state for a generic 10 day flare corresponding to the timescale of several major outbursts that were observed in the optical regime during our campaign. The various curves show the instantaneous spectral energy distribution of 3C 66A at several different times in the observer's frame: red dotted line ( $\sim 5$ th hour), green dashed line ( $\sim 8$ th hour), blue dot-dashed line ( $\sim 14$ th hour), yellow long-dashed line ( $\sim 20$ th hour), long-dashed black line ( $\sim 8$ th day, highest state attained by the system during flaring), gray solid line ( $\sim 9$ th day), dotted violet line ( $\sim 16$ th day), cyan solid line ( $\sim 18$ th day), dashed magenta line ( $\sim 20$ th day) and red solid line ( $\sim 22$ nd day, equilibrium state reached by the system after the flaring episode is over). The synchrotron component of the flaring state peaks at  $\nu_{\text{syn}}^{\text{peak}} \approx 1.1 \times 10^{15}$  Hz and the SSC component peaks at  $\nu_{\text{SSC}}^{\text{peak}} \approx 2.7 \times 10^{22}$  Hz. The SSC component of this state cuts off at  $\nu_{\text{SSC,cutoff}} \approx 2.3 \times 10^{24}$  Hz. The synchrotron cooling timescale in the optical regime is  $\approx 37$  minutes for the flaring state (Joshi and Böttcher 2007).

emission region size cannot exceed  $3.6 \times 10^{15} (D/24)$  cm. Thus, this model suggests that the harder X-ray photons come from the SSC and not the synchrotron mechanism with the expected spectral hardening taking place at  $\sim 7$  keV. The high energy component, due to the SSC emission, for the time-averaged spectrum cuts off at  $\sim 1.0 \times 10^{24}$  Hz or 4 GeV (Figure 3.7).

Using the simulated level of VHE emission I could also predict that the object is well within the observational range of MAGIC, VERITAS (if EC component is dominant), and Fermi (Figure 3.7) whose sensitivity limit is 50 times lower than that of EGRET at 100 MeV and even more at higher energies and its two year limit for source detection in an all-sky survey is  $1.6 \times 10^{-9}$  photons  $\text{cm}^{-2} \text{s}^{-1}$  (at energies  $> 100$  MeV). This prediction recently came true when VERITAS detected 3C 66A in an active state emitting  $> 100$  GeV  $\gamma$ -ray emission (Swordy 2008). Such predictions can guide future observations of the source with these facilities, which provide an important means to improve a model's physical constraints at such high energies.

The simulated SEDS for both the states of 3C 66A show that the total energy output of the two components is comparable to each other, as is typical for LBLs (see Section 1.2.1). The observed lightcurves did not agree well with a flaring profile that was top-hat or triangular in time as can be seen in the Fig. 3.8. The presence of a flare that is Gaussian in time might represent an initial injection of particles into the emission region at the base of the jet. The particles slowly get accelerated as a shock wave ploughs through the region and finally dies out (in time). Crucial

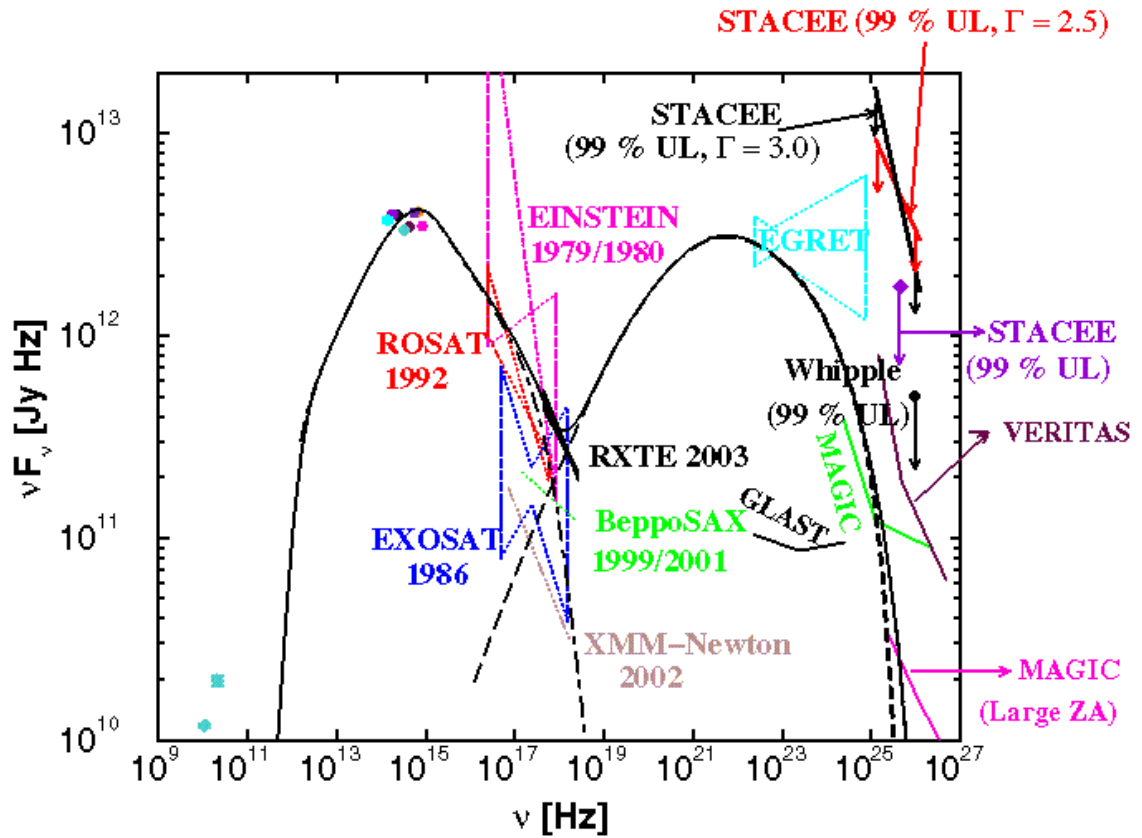


Figure 3.7: Time- averaged SED of 3C 66A for a period of 23 days around a flare as shown in Figure 3.6. The filled colored circles are the time-averaged optical and IR data points for the entire campaign period. The dot-dashed black line is the contribution from the synchrotron component only whereas the long-dashed black line indicates the contribution of the SSC component only. The time-averaged synchrotron component peaks at  $\nu_{\text{syn}}^{\text{peak}} \approx 7.2 \times 10^{14}$  Hz whereas the time-averaged SSC component peaks at  $\nu_{\text{SSC}}^{\text{peak}} \approx 5.3 \times 10^{21}$  Hz. The synchrotron component cuts off near 7 keV whereas the SSC component cuts off at  $\sim 4$  GeV. The black colored dashed line indicates the attenuation due to the optical depth at VHE energies. The  $\gamma - \gamma$  absorption effect becomes significant at  $\sim 200$  GeV. The green, maroon and magenta lines indicate the sensitivity limits for an observation time of 50 hours for MAGIC, VERITAS and MAGIC (Large Zenith Angle) and for GLAST for an observation time of 1 month (Joshi and Böttcher 2007).

information on the dominant acceleration mechanism comes from the change in the shape of the particle injection spectral index with time, which might also indicate a

possible change in the B-field orientation. According to the current understanding of acceleration mechanisms, parallel shocks (see Section 5.2) generally produce electron spectra of  $Q_e(\gamma) \propto \gamma^{-q}$  with  $2.2 \lesssim q \lesssim 2.3$  (Achterberg et al. 2001; Gallant et al. 1999), whereas oblique shocks (see Section 5.2) produce much softer injection spectral indices. On the other hand, 2nd order Fermi acceleration (see Section 5.2) behind the shock front might give rise to a harder injection index of the order of  $q \sim 1$  or beyond (Virtanen and Vainio 2005).

In order to reproduce the flaring state, the simulation first starts out in the quiescent state with quiescent state parameters and then the value of these parameters is changed to the flaring state parameters as the flaring is introduced in the simulation. Since, the value of  $q$ , in our simulations, changes from 3.1 (quiescent state) to 2.4 (flaring state) it might indicate a possible change in the orientation of the B-field from oblique to parallel during the flaring episode or an interplay between the 1st and 2nd order Fermi acceleration thereby making the particle spectra harder. The contribution from such acceleration mechanisms and the shear acceleration (Rieger and Duffy 2004) might play an important role in accelerating the particles to higher energies.

The simulated optical variability in the R band (0.55 mag) matches the observed value (0.3-0.5 mag) for a 10 day period outburst. The predicted variability in the B band is more than that of R by  $\sim 0.15$  mag as also observed, which indicates that

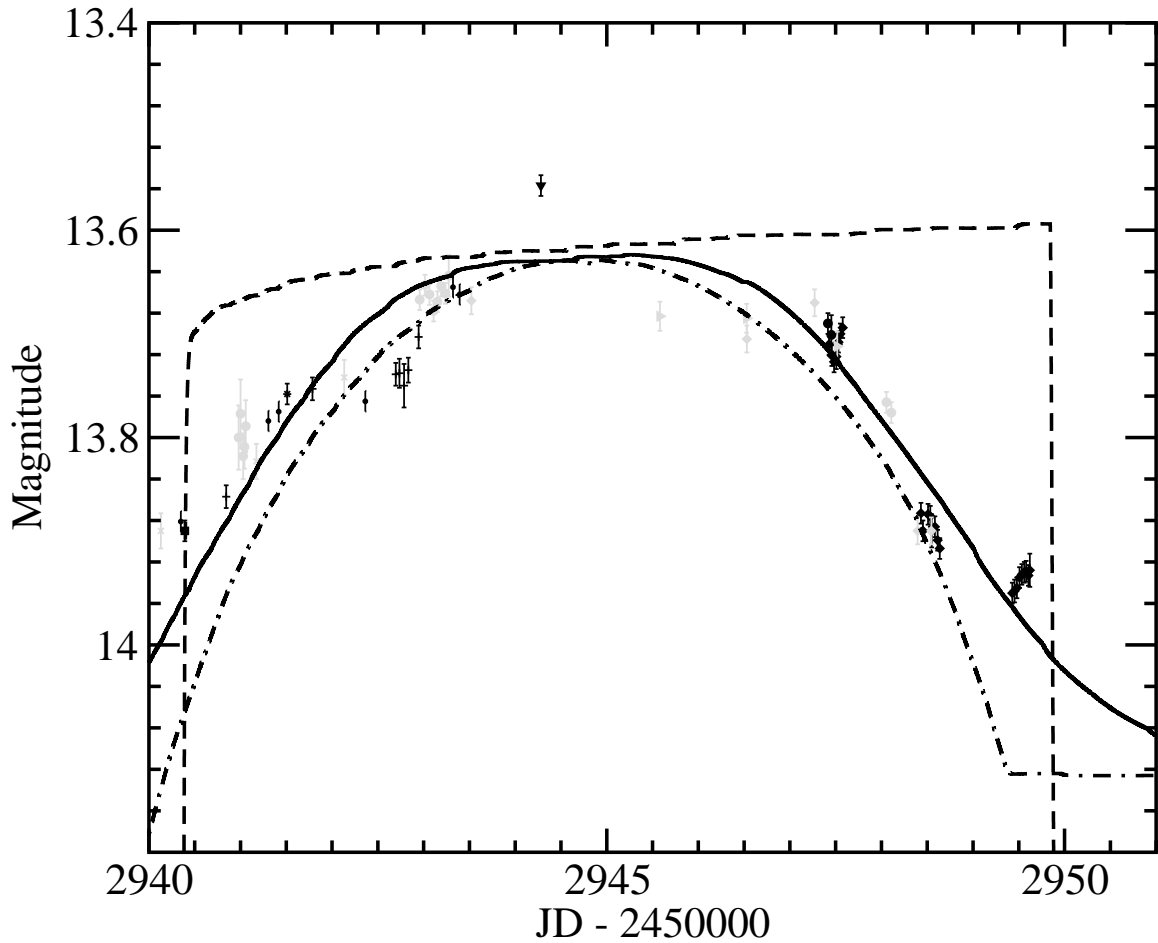


Figure 3.8: The simulated lightcurves for various flaring profiles that have been superimposed on the observed R-band lightcurve (representative points, Figure 7 of [Böttcher et al. \(2005\)](#)) for an outburst on  $\sim$  November 1st 2003. The solid black line denotes a flaring profile that is Gaussian in time as used for the flare in Figure 3.6, the dash-dotted black line is a triangular flaring profile whereas the dashed black line is a flaring profile that is top-hat in time. As can be seen, the Gaussian flaring profile closely matches the width as well as the profile of the observed flare ([Joshi and Böttcher 2007](#)).

the spectrum is becoming harder (Figure 3.9) with the spectral upturn occurring at  $B-R \approx 0.72$  mag as shown in Figure 3.10.

Figure 3.10 is a hardness intensity graph that shows that the object follows a positive correlation of becoming harder in B-R while getting brighter in both the

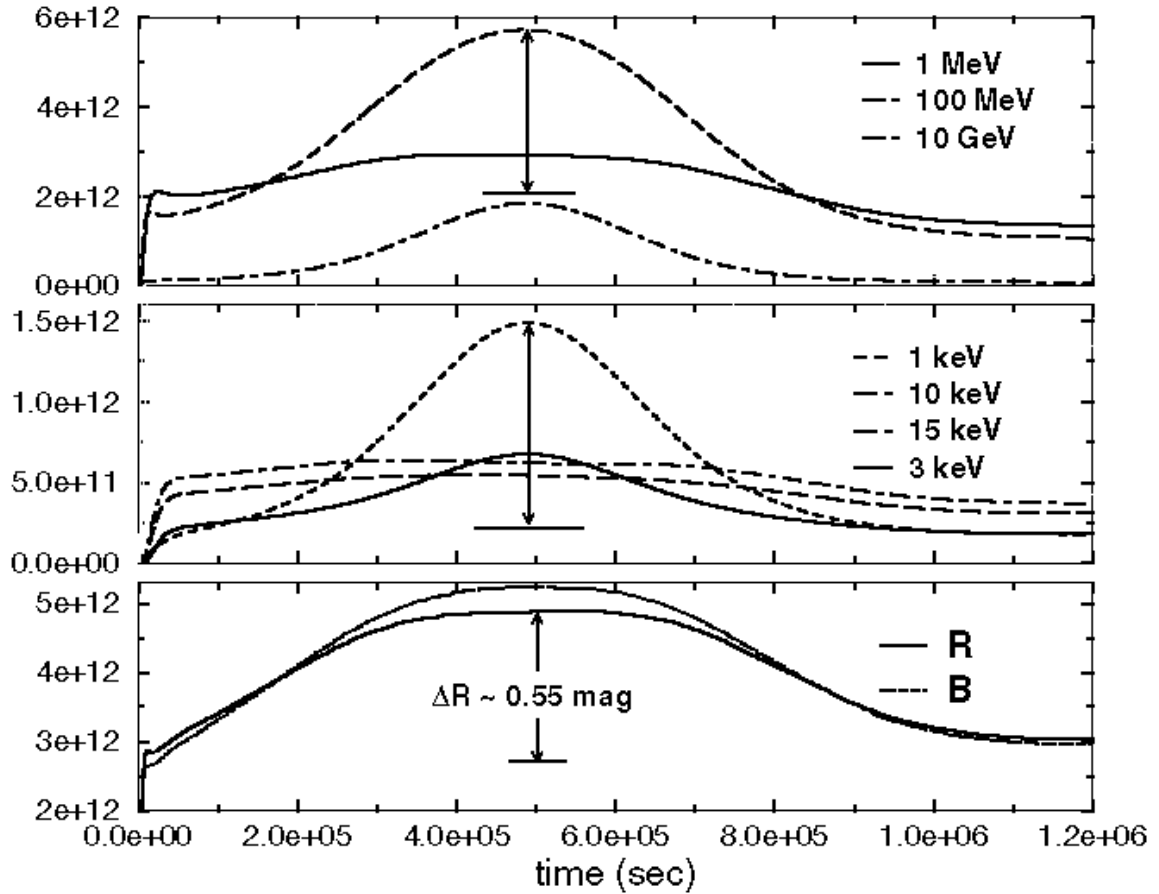


Figure 3.9: Simulated lightcurves for the optical, X-rays and  $\gamma$ -ray energy regimes shown in the three panels respectively. The plot is between time (sec.) on the x-axis and  $\nu F_\nu$  (Jy Hz) on the y-axis (cannot be seen here). The simulated variability in the R band is  $\approx 0.55$  mag as indicated by the arrows. The B band, denoted by the black dotted line exhibits a higher variability of  $\approx 0.7$  mag, in the simulation, than that in the R band, which is consistent with our observations. The simulated lightcurve at 1 keV is indicated by a black dashed curve and exhibits an amplitude variation of  $\approx 1.4 \times 10^{12}$  Jy Hz. The 3, 10 and 15 keV lightcurves, denoted by the black solid line, black long-dashed line and the black dot-dashed curve, respectively, on the other hand do not exhibit much variability. In the VHE regime, the 1 MeV lightcurve is denoted by a black solid line. The 100 MeV lightcurve is indicated by a black long-dashed curve and the simulated variability amplitude in this energy regime is on the order of  $10^{12}$  Jy Hz. The black dot-dashed line indicates the lightcurve at 10 GeV (Joshi and Böttcher 2007).

bands, at low fluxes in R, during the 10-day flare simulated in Figure 3.6. This agrees well with the observed optical variability pattern. In this study, I have not addressed the microvariability that was observed in the optical band as that analysis would open up an even larger parameter space, which cannot be reasonably well constrained without any variability information in the X-ray regime.

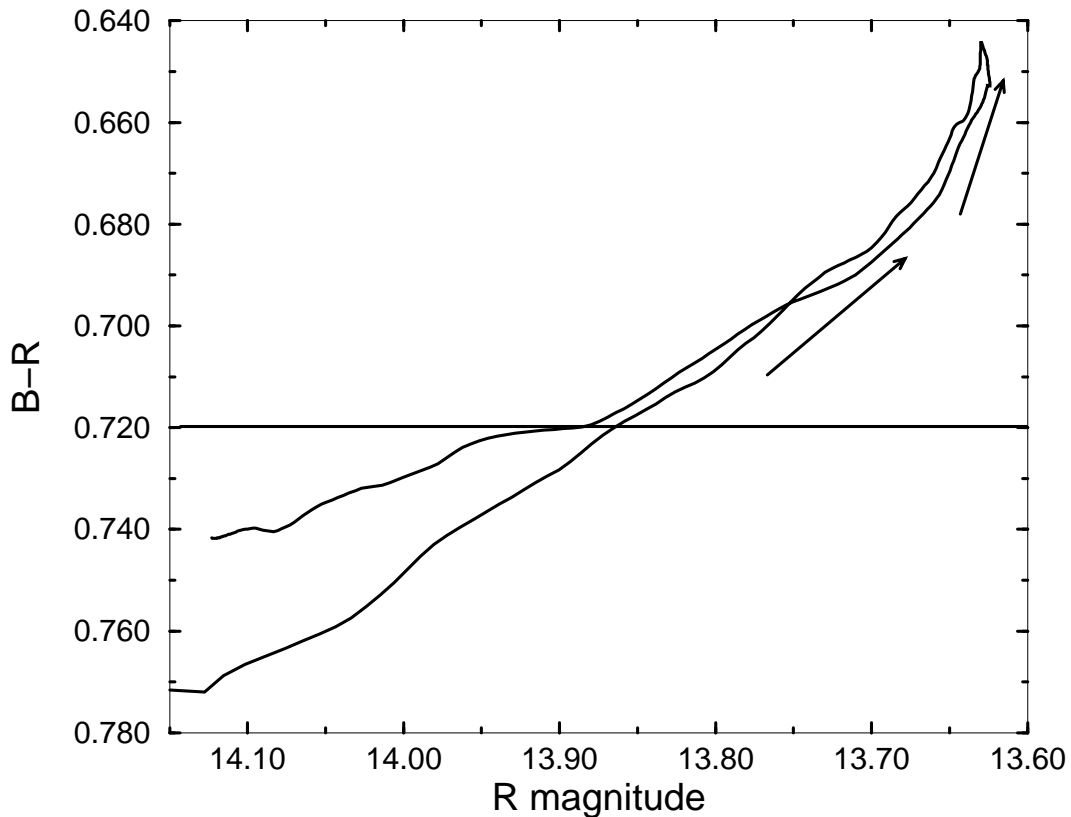


Figure 3.10: The simulated hardness-intensity diagram indicates a positive correlation between R- and B-band for an outburst lasting for  $\sim 10$  days. The object becomes brighter in R and harder in B-R as shown by the arrows. The spectral upturn takes place at  $B-R \approx 0.72$  mag where the flux in B equals that in R (corresponding to  $\alpha_{BR} = 0$ ) (Joshi and Böttcher 2007).

As can be seen from Figures 3.8 and 3.9, the flare declines faster than the time taken by the flare to rise. This might indicate that the particle's synchrotron cooling timescale in the optical regime is less than or equal to the light crossing time (dynamical time scale), which determines the shortest observed variability time scale. This condition can be used to obtain a Doppler-dependent lower limit on the magnetic field. Thus we can write the observed synchrotron cooling timescale,  $\tau_{\text{cool, syn}}^{\text{obs}}$ , in the optical regime to be

$$\tau_{\text{cool, sy}}^{\text{obs}} \approx 2.8 \times 10^3 \left( \frac{D}{15(1+z)} \right)^{-1/2} \left( \frac{B}{2.9\text{G}} \right)^{-3/2} \nu_{15,\text{R}}^{-1/2} \text{ s}, \quad (3.8)$$

where  $\nu_{15,\text{R}} = 0.429$  is the frequency in the R band in units of  $10^{15}$  Hz. The observed dynamical time scale is given by

$$\tau_{\text{dyn}}^{\text{obs}} \approx \left( \frac{R_b}{c} \right) \left( \frac{1+z}{D} \right). \quad (3.9)$$

Since  $\tau_{\text{cool, syn}}^{\text{obs}} \leq \tau_{\text{dyn}}^{\text{obs}}$ , we can write

$$\tau_{\text{cool, syn}}^{\text{obs}} = 8.18 \times 10^4 \left( \frac{1+z}{D} \right)^{1/2} B_G^{-3/2} \leq \left( \frac{R_b}{c} \right) \left( \frac{1+z}{D} \right) \text{ s}, \quad (3.10)$$

where  $B_G$  is magnetic field strength in Gauss. This time scale gives a lower limit on the value of the magnetic field in the jet that can be used for simulations:

$$B_G \geq 1.88 \times 10^3 \left( \frac{D}{1+z} \right)^{1/3} \left( \frac{c}{R_b} \right)^{2/3}. \quad (3.11)$$

Putting in values of  $z = 0.444$ ,  $D = 24$ , and  $R_b = 3.59 \times 10^{15}$  cm in equation 3.11 we obtain the lower limit of  $B_G \geq 1.98$ . Thus, in order to obtain meaningful results from the modeling of 3C 66A the magnetic field value used in the simulations should be higher than 1.98 G. I allowed the magnetic field value to evolve in time by keeping  $\epsilon_B = 1$ . This yielded an average value of 2.4 G in the simulated quiescent state and 2.8 G in the simulated flaring period, which conforms with the lower limit obtained from equation 3.11. The observed synchrotron cooling timescale,  $\tau_{\text{cool, syn}}^{\text{obs}}$  in the optical regime can be calculated from equation 3.8 using  $B = 2.4$  G for the quiescent state and  $B = 2.8$  G and for the flaring state. This yields a value of  $\tau_{\text{cool, sy}}^{\text{obs}} \sim 1.5$  hours for the quiescent state whereas for the flaring state it reduces to 1.2 hours. These values are smaller than that of the observed minimum variability timescale, which was  $\sim 2$  hours, thus supporting the observational results of lack of frequency dependent spectral variability.

From Figure 3.9, it can be seen that the X-ray lightcurves tend to cross over each other. This is because hard X-ray photons are produced from SSC scattering always whereas soft X-ray photons are dominated by synchrotron component during flaring. The lightcurve of soft X-ray photons of energy 1 keV exhibits a greater variability of  $\sim 1.4 \times 10^{12}$  Jy Hz in its flux as compared to their optical counterpart. This is expected because the soft X-ray photons, during the flaring episode, are produced from synchrotron emission of electrons that are accelerated to very high energies and as a result have a very short cooling timescale and thus greater variability. In case

of hard X-rays no significant variability is predicted. This is because such photons are produced from Compton upscattering of synchrotron photons off the low-energy electrons and as a result the cooling timescale is much longer as compared to the cooling timescale of their soft X-ray and optical counterparts. Hence, the variability information gets washed out. The predicted X-ray spectral variability pattern of large variability in the low X-ray energy band and negligible variability in the high X-ray energy band is similar to what has also been observed in the BL Lac object BL Lacertae on several occasions (see for e.g., [Ravasio et al. 2003, 2002](#)).

From Figure 3.11, it can be seen that no spectral hysteresis patterns are present for the optical and soft X-ray photons. This is expected because the cooling timescale of their parent electron population is so short that what is observed is the average effect of this cooling over the dynamical timescale and hence any hysteresis pattern gets smeared out.

On the other hand, one expects to see these patterns at higher energies (not VHE) because as explained earlier, this photon population comes from Compton upscattering off low-energy electrons, which have a longer cooling timescale and as a result the photon population gradually builds up over time and then dies away giving rise to a hysteresis pattern (Figure 3.12). The slight spectral softening at 10 keV seen in its hysteresis pattern (Figure 3.11) for higher values of  $\nu F_\nu$  indicates a small synchrotron contribution near the peak of the flare.

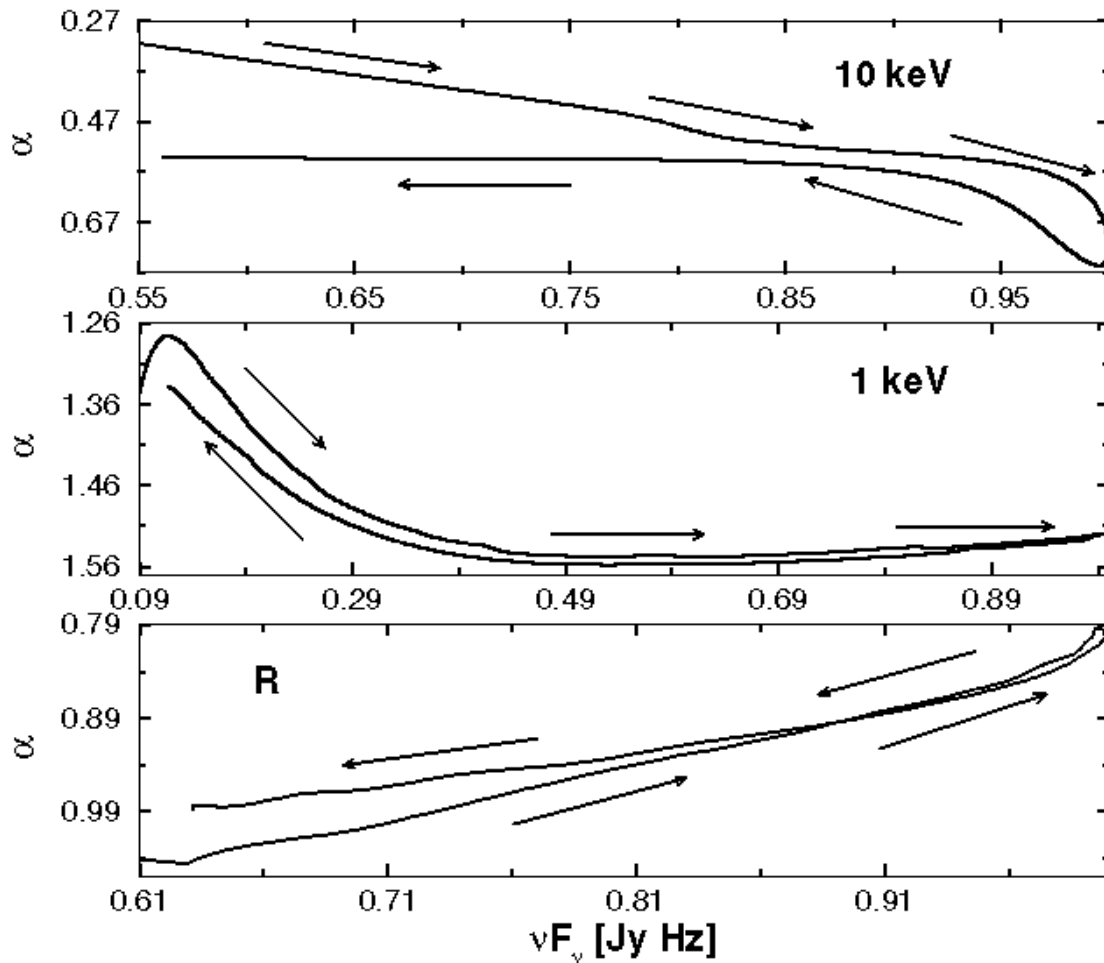


Figure 3.11: Simulated spectral hysteresis pattern in the R-band, 1 keV and 10 keV energy regimes, shown in the three panels respectively. As can be seen, the hysteresis pattern starts to show up in the 10 keV energy regime (Joshi and Böttcher 2007).

The simulated instantaneous SED, for a pure SSC model, shows a definite presence of  $\gamma$ -ray emission in 3C66A, in the quiescent as well as the flaring state (Figures 3.5 and 3.6). The VHE emission, according to the simulations for the time averaged spectrum, cuts off at  $\sim 1.0 \times 10^{24}$  Hz or 4 GeV. According to the simulations, SSC mechanism is responsible for the emission of VHE  $\gamma$ -ray photons in both the quiescent

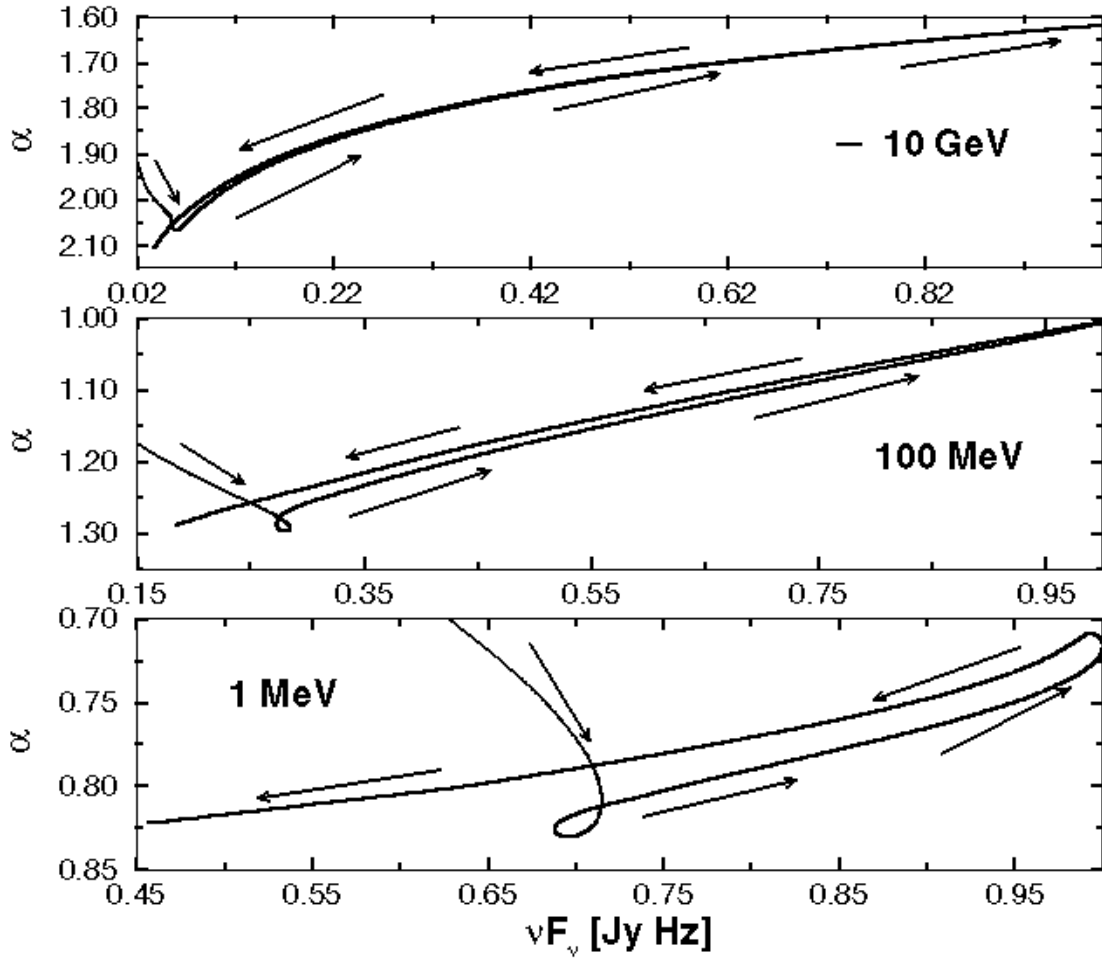


Figure 3.12: Simulated hysteresis pattern for 1 MeV, 100 MeV and 10 GeV energy regimes, shown in the three panels respectively. The hysteresis pattern is prominent for the 1 MeV energy regime but starts to become absent at higher energies (Joshi and Böttcher 2007).

and the flaring states. As can be seen from Figure 3.9, the  $\nu F_\nu$  value for the simulated lightcurves of VHE photons changes by  $\sim 4.0 \times 10^{12}$  Jy Hz at 100 MeV. The variability in VHE photons is expected as they are the result of Compton upscattering off the higher energy electrons and due to this the hysteresis pattern is not seen at such high

energies as the cooling timescale of such high energy electrons is very short (Figure 3.12).

I had also investigated for a possible presence of the EC component in the high-energy part of the SED of 3C 66A. From Figure 3.13, it can be seen that the high-energy component of 3C 66A, in the flaring state, could start out with a dominant contribution of the EC emission, shown by the red solid line. But as the blob travels further out and passes the outer edge of the BLR, the EC contribution becomes less significant and the SSC emission takes over. This is indicated by the black long-dashed line in the figure. This might indicate that this maximum contribution from the EC component would be just enough to explain the historical EGRET flux and that there could be GeV flaring due to early external Comptonization.

I had also evaluated the effect of an optical depth due to the Intergalactic Infrared Radiation Background (IIRB) on the spectra of 3C 66A, and found it to be insignificant in the energy range we are interested in (Figure 3.7). In order to determine the optical depth due to the IIRB, I had used the analytic expression given in [Stecker et al. \(2006\)](#). The  $\gamma - \gamma$  absorption at  $\sim 100$  GeV becomes important as  $\tau_{\gamma\gamma} \sim 1$  and becomes slightly observable at  $\sim 200$  GeV as the optical depth takes a value of,  $\tau_{\gamma\gamma} \sim 2.9$ . Hence, the SSC emission exponential cutoff value at  $\sim 4$  GeV is indeed intrinsic.

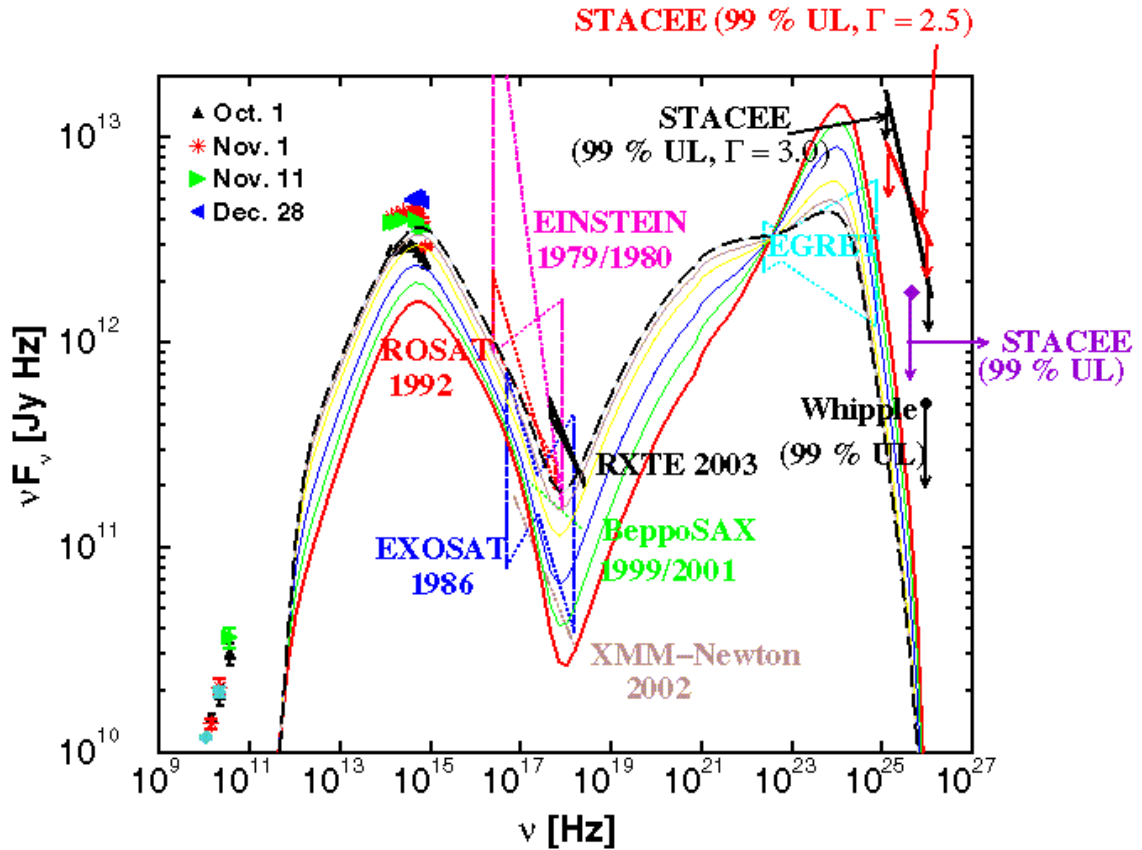


Figure 3.13: Simulation of the effect of the BLR on the instantaneous SED of 3C 66A for the first 3 days of a simulation similar to Figure 3.6. The curves in the figure denote the instantaneous spectra obtained from the simulation. The red solid line denotes one of the initial instantaneous spectra at the beginning of the simulation whereas the black long-dashed line indicates the last spectrum obtained from the simulation (Joshi and Böttcher 2007).

### 3.6 Summary

A recent WEBT campaign to obtain multiwavelength data was carried out for 3C 66A, organized by Böttcher et al. (2005) from July 2003 until April 2004. It is a LBL with an uncertain redshift determination of  $z = 0.444$  (Bramel et al. 2005; Finke et al. 2008). It has exhibited rapid microvariability in the optical and near

infrared in the past and has been suggested as a promising candidate for detection by the new generation of atmospheric Čerenkov telescope facilities like VERITAS or MAGIC (Costamante and Ghisellini 2002). In conjunction with this project, I carried out a literature survey on 3C 66A to determine the historical flux levels displayed by the source as a guide to new observations. I had a significant role in combining disparate data sets from different optical observatories and placing them on a common photometric scale. I used the resulting multiwavelength data to estimate key physical properties of the source by employing fundamental physical arguments. These properties describe the sub-parsec scale outflow, which is closest to the central engine. The resulting values served as crucial input for detailed numerical models for the blazar source.

I carried out an extensive analysis of the data of 3C 66A, obtained from this campaign, using a time-dependent leptonic jet model. The analysis involved theoretical understanding of the dominant radiation mechanism in the production of the high-energy component of the SED of 3C 66A in the quiescent as well as the flaring state, and predictions regarding the variability patterns in the X-ray and the VHE energy regimes where such patterns could not be detected during the campaign. The object was well sampled in the optical, especially in the R-band, during the campaign. It had exhibited several major outbursts ( $\sim 10$  days) in this regime with a variability of  $\Delta m \sim 0.3-0.5$ . The X-ray data covered the 3-10 keV range with the onset of the

high-energy component expected at  $\geq 10$  keV photon energies. Only upper limits in the VHE regime were obtained from the campaign.

The simulations could successfully reproduce the observed SED as well as the optical spectral variability patterns. The model suggests the dominance of the SSC mechanism in the production of hard X-ray as well as VHE photons. On the other hand, soft X-ray photons exhibit spectral softening during flaring indicating the onset of the synchrotron component in this energy range. According to the simulated time-averaged spectrum, the synchrotron component is expected to cut off near 7 keV whereas the SSC component cuts off at  $\sim 4$  GeV.

A flaring profile that was Gaussian in time could successfully reproduce the observed flaring profile for a timescale of  $\sim 10$  days. The simulated variability in R ( $\Delta m \sim 0.55$ ) agreed well with the observed variability. According to the simulations, the object flares up in R and B simultaneously with  $\tau_{\text{cool, syn}}^{\text{obs}}$  (1.2 hours) being less than the light crossing time (2 hours) during flaring. No significant variability is predicted in the hard X-ray regime. This is due to the production of such photons from Compton upscattering off low-energy electrons with cooling timescales much longer than the light crossing time,  $3R_b/4c$ . On the other hand, the simulated lightcurves of VHE  $\gamma$ -ray photons exhibit significant variability and should be observable by future VHE observations of the source. The reason for the presence of a significant variability in the VHE photons is that such photons are produced from the Compton upscattering off higher energy electrons, which have shorter cooling timescales than the

light crossing time and thus the variability information gets carried in the resultant radiation.

The effect of the optical depth due to  $\gamma - \gamma$  absorption by the IIRB on the SED of 3C 66A was also evaluated. The simulations do not predict a significant effect on the SED due to the optical depth. The SSC emission cutoff predicted to be at  $\sim 4$  GeV can be taken as the intrinsic SSC emission exponential cutoff value for this object. We predict the object to be well within the observational range of MAGIC and Fermi. Finally, the EC emission for this object was also calculated and it appears that the EC emission could be dominant in the high-energy component initially, but as the emission region travels further away from the BLR, the EC contribution becomes less significant and the SSC emission takes over. It is highly probable that this maximum contribution of the EC component might explain the historical EGRET flux and that there could be GeV flaring due to early external Comptonization. The object could also be detected by VERITAS if the EC contribution is dominant in the high-energy component of the SED.

## CHAPTER 4

# Internal Shock Model for Blazar

## Jets

### 4.1 Introduction

The SEDs of blazars provide valuable information regarding the acceleration of jet particles and the dominant mechanism in the production of the resulting radiation in a time-dependent manner. Understanding the acceleration of relativistic particles and the geometrical structure of the acceleration region at sub-parsec scales inside a relativistic jet is highly crucial to the development of a code that is capable of explaining the radiation as well as the acceleration mechanisms of high-energy particles in the jets of blazars. Many authors have carried out similar studies in the past of the blazar jets ([Böttcher and Schlickeiser 1997](#); [Georganopoulos and Marscher 1998](#); [Böttcher and Chiang 2002](#); [Joshi and Böttcher 2007](#)) in which a spherical emission region was considered and a power-law energy distribution of injected electrons and positrons was assumed. Since positrons lose the same amount of energy as electrons via the same radiative loss mechanisms, I do not distinguish between them throughout this chapter. The evolution of the particle population and the subsequent photon emission was then solved numerically in a time-dependent manner in order to gener-

ate the theoretical light curves, spectral variability patterns, SED, and other features to obtain a satisfactory fit with the observed data of a given source.

Even though such theoretical approaches have successfully reproduced the observed SED and the spectral variability patterns of various blazars, and have provided the relevant physical parameters of the emission region, the location and the mode of particle acceleration in the jets of such systems remain open questions. Most of these theoretical approaches have assumed a spherical geometry for the emission region, continuous injection of particles, and homogeneous population of both electrons and photons throughout the emission region (Sikora et al. 1994; Bloom and Marscher 1996; Böttcher and Bloom 2000; Joshi and Böttcher 2007). Such assumptions are good only to a first approximation and do not completely account for the observations. Thus, a more advanced theoretical approach is needed that can explain the acceleration as well as radiative processes taking place inside such jets as accurately as possible. The main benefit of using such an approach would be to treat the characteristics of the energized plasma, such as electron energy distribution and magnetic field, not as free parameters but as products of the underlying acceleration mechanism. This, as a result, would enable us to link the observed emission properties to the physics of energy transport inside a jet.

As far as particle acceleration is concerned, significant progress has been made in this direction in recent years. In the case of leptonic jet models, the electrons' accel-

eration and their subsequent injection has been treated in various ways by different authors.

[Sokolov et al. \(2004\)](#) consider a collision between a moving shock and a stationary shock, namely the Mach disk, to accelerate the background plasma electrons to highly relativistic energies. Such electrons then start to radiate via synchrotron and inverse Compton processes and result in the observed emission. [Spada et al. \(2001\)](#) (hereafter S01) and [Mimica et al. \(2004\)](#), on the other hand, consider an internal shock model to accelerate the particles inside a jet. In such a scenario, shells of plasma with different mass, energy, and velocity are ejected intermittently by the central engine. The faster moving shells then catch up with the slower moving ones, ejected at earlier times, to result in collisions that produce the shocks internal to the jet. These shocks accelerate the plasma electrons to ultrarelativistic energies. The energized electrons then lose their energies via various radiative processes to produce the observed radiation.

All of the above mentioned approaches consider the formation of reverse and forward shocks inside the jet, that lead to particle acceleration in a region resulting from the collision. The injection of particles into the emission region continues as long as it takes for the shocks to cross the entire region. The population of electrons and photons has been assumed to be homogeneous in density throughout the emission region. The geometry of the region has been assumed to be cylindrical (cubic geometry in case of [Chiaberge and Ghisellini \(1999\)](#)) instead of being spherical. This type of a geometry closely represents the real structure of the emission region when it is

closer to the central engine. It also represents the radio core observed in Very Large Baseline Interferometry (VLBI) images that tends to have a more elongated structure as compared to a spherical one.

In a recent approach, [Graff et al. \(2008\)](#) invoke the standing or propagating shock in a collimated jet to accelerate the particles and adopt a multi-zone pipe geometry for the emission region to simulate the resultant radiation and variability of blazars via synchrotron and SSC processes. Their model considers the inhomogeneity in the particle and photon population throughout the emission region and also takes into account the non-local, time-delayed SSC emission of the source.

Other acceleration scenarios, such as, isolated shocks propagating along the jet ([Marscher and Gear 1985](#); [Kirk et al. 1998](#); [Sikora et al. 2001](#)), oblique shocks propagating through a pre-existing jet ([Ostrowski and Bednarz 2002](#)) or particle acceleration in shear flows ([Rieger and Duffy 2004](#)) have also been shown to work for blazar jets.

In this chapter, I will describe the use of the internal shock scenario to develop a code that is capable of explaining the acceleration as well as radiation mechanisms in relativistic blazar jets at sub-parsec scales. I have used this method to calculate the relevant physical parameters of a cylindrical emission region that would result in the production of the observed radiation. In this approach, I am taking into account the inhomogeneity in the photon and electron population throughout the region, which automatically addresses the non-local, time-delayed SSC emission of the source.

In Section 4.2, I will briefly describe shocks and their propagation through a medium. In Section 4.3, I will describe the interaction between two shells of plasma resulting in internal shocks and the subsequent treatment of the collision in a relativistic hydrodynamic manner. Section 4.4 deals with the calculation of the volume and angle averaged photon escape timescale for a cylindrical geometry that I have carried out independently of any previous work. Section 4.5 is dedicated to the description of the numerical approach that I have used for calculating the various radiative energy loss rates as well as photon emissivities by taking into account the inhomogeneity in the density of the photon and electron population throughout the emission region. In Section 4.6, I describe the relevant light-travel time delays that are required to accurately register the radiation in the observer's frame of reference. I discuss the numerical approximation that has been used to calculate the synchrotron photon density in the simulations in Section 4.7 and I summarize in Section 4.8.

## 4.2 Shocks

The fundamental equations of fluid dynamics are conservation of mass, momentum, and energy. In case of the hydrodynamic motion of an ideal fluid (fluid in which thermal conductivity and viscosity are unimportant), the conservation of mass is described by the *continuity equation*. According to this equation, the rate of change in the local density,  $\rho$ , of a fluid material is equal to the difference in the rate of flow

of that material into and out of a given test volume along the direction of its motion (Dopita and Sutherland 2003). The *continuity equation* is given by

$$\frac{\partial \rho}{\partial t} + \nabla \cdot (\rho \mathbf{v}) = 0 , \quad (4.1)$$

where  $\mathbf{v}$  is the velocity of the fluid material. The conservation of momentum and energy is described by the *Euler's force equation*. According to this equation, the rate of change of momentum of a fluid material is equal to the flux of momentum of the material into a given volume plus the forces acting upon that material. The forces are composed of external forces ( $\mathbf{F}$ ), like gravitational forces, and internal forces due to pressure gradients ( $\nabla P$ ) (Dopita and Sutherland 2003). The *Euler's force equation* is given by

$$\rho \left[ \frac{\partial \mathbf{v}}{\partial t} + (\mathbf{v} \cdot \nabla) \mathbf{v} \right] = \mathbf{F} - \nabla P . \quad (4.2)$$

In addition to the conservation equations, the Maxwell equations must also be satisfied along with an equation of state for the flow of the fluid material that relates pressure to other thermodynamic variables, such as density and temperature. For nonrelativistic fluids, the equation of state is given by

$$P = K \rho^{\hat{\gamma}} , \quad (4.3)$$

where  $K$  is the proportionality constant and is a function of entropy, and  $\hat{\gamma} = C_P/C_V$  is the adiabatic index, which is the ratio of the specific heats at constant pressure,  $P$ , and at constant volume,  $V$ .

Now, if a disturbance propagates through such a stationary fluid at a speed greater than the speed of sound in the fluid the resultant changes in the flow variables, such as  $v$ ,  $\rho$ ,  $P$ , and temperature  $T$ , are communicated in a discontinuous manner over space. This discontinuity in the flow variables is what is termed as a shock. In such cases, the information regarding the change in flow variables does not propagate backwards in the spatial coordinates. In case of AGN jets the shocks tend to be relativistic in nature. Across the shock, equations 4.1 and 4.2 still apply. These equations are used to calculate the changes in the flow variables across the shock front, which is defined as a region over which the flow variables undergo sudden changes (Kwok 2006). The equations that define these changes in such physical quantities are called the Rankine-Hugoniot jump conditions. A schematic of the shock propagation through a medium is shown in Fig. 4.1.

For non-relativistic, hydrodynamic, strong shocks (shocks with Mach number,  $M_o$ , approaching infinity), the jump conditions (in the frame of the shock) for density, velocity, and pressure are given by (Kwok 2006)

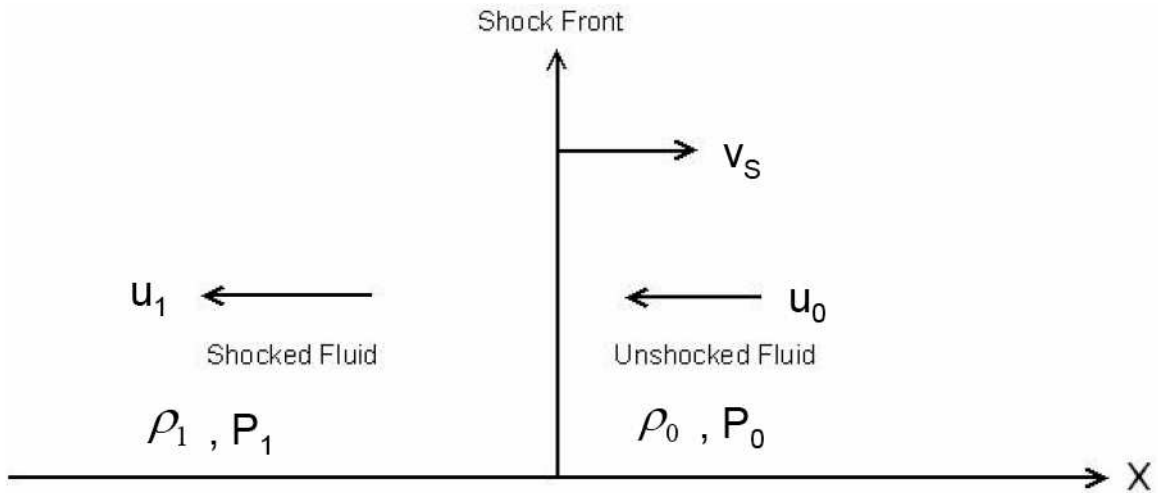


Figure 4.1: Schematic of the shock propagating through a medium at rest. The shock travels with a speed  $v_s$  in the frame of the medium. In the frame of the shock, the medium enters the shock front with a speed  $u_o = -v_s$  and leaves the front with a speed  $u_1$ . The quantities  $\rho_o$  and  $P_o$  are the density and pressure of the unshocked gas and  $\rho_1$  and  $P_1$  are that of the shocked gas in the frame of the shock.

$$\begin{aligned}
 \frac{\rho_1}{\rho_o} &= \frac{\hat{\gamma} + 1}{\hat{\gamma} - 1}, \\
 \frac{u_1}{u_o} &= \frac{\hat{\gamma} - 1}{\hat{\gamma} + 1}, \\
 \frac{P_1}{P_o} &= \frac{2\hat{\gamma}}{\hat{\gamma} + 1} M_o^2 - \frac{\hat{\gamma} - 1}{\hat{\gamma} + 1}.
 \end{aligned} \tag{4.4}$$

All astrophysical outflows eventually interact with the surrounding medium, which could either be a preexisting interstellar gas, galactic medium, or a circumstellar medium. As a result of this interaction, the high pressured expanding gas of the outflow that is travelling either supersonically (supernova outflows, stellar winds, outflows from newly born low-mass stars) or relativistically (AGN outflows) starts to push against the medium it has encountered. This drives a shock into the medium,

which heats it, increases its pressure, and makes it move outward. The energy needed to heat the medium and make it moving outward comes at the expense of the kinetic energy of the expanding outflow. This abruptly slows down the gas of the outflow, and as a result of this another shock is transmitted into the outflow. This inner shock, also referred to as the reverse shock (RS), appears to move in the opposite direction of the shock that is travelling outward into the medium (forward shock (FS)) in the frame of the shocked medium (comoving frame). In the frame of the central engine (lab frame) that is ejecting the outflow, both the shocks appear to move in the forward direction. The two shocks generally have unequal velocities. As a result, the temperatures of the respective gases shocked by the two shocks are not the same but the pressures of these two shocked gases are the same. Thus, at the point of interaction of the outflowing gas and the medium, there is a jump in the density and temperature of the gas such that the product  $nT$  remains constant. This point of interaction is called a *contact discontinuity* (CD) (Dopita and Sutherland 2003) and the velocity of the gases across the discontinuity also remains equal.

### 4.3 Collision Hydrodynamics

In the internal shock scenario, the central engine produces shells of plasma with different mass and energy travelling with different relativistic velocities. As a result of this disparity, the faster moving shells catch up with the slower moving ones, released at earlier times, resulting in an inelastic collision. The collision results in the

formation of the two shocks, FS that propagates into the slower moving outer shell and RS that propagates into the faster moving inner shell. The shocks are separated by a CD across which the pressure and the velocity of the shocked fluids stay constant, as explained in Section 4.2. As the shocks propagate into their respective shells, they convert the ordered bulk kinetic energy of the plasma into magnetic field energy and random kinetic energy of the electrons. As a result, the electrons get accelerated to extremely high energies and start to radiate to produce the radiation observed at all wavelengths from radio through VHE  $\gamma$ -rays.

For the purposes of my study, I am considering a single inelastic collision, at sub-pc scales of the jet, between a slower moving outer shell and a faster moving inner shell. Figure 4.2 shows a schematic diagram of the inner and outer shells propagating through the jet with bulk Lorentz factors (BLFs)  $\Gamma_i$  and  $\Gamma_o$  ( $\Gamma_i > \Gamma_o$ ). I study the dynamics of the collision and the subsequent photon emission from non-thermal relativistic particles after the interaction between the two shells has started. I assume that the magnetic field is generated during the collision and hence does not play a role in the dynamics of the collision. The entire treatment of shell collision and shock propagation is hydrodynamic and relativistic in nature. The expansion of the individual shells as well as the merged shell has not been taken into account as the jet is well collimated at sub-pc scales.

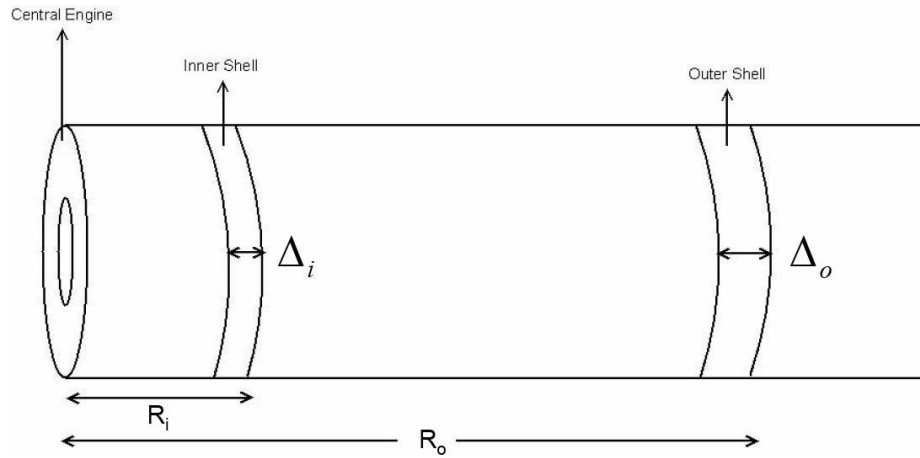


Figure 4.2: Schematic of two cylindrical shells located at different distances from the central engine. The outer shell propagating through the jet with BLF  $\Gamma_o$  was ejected from the engine at an earlier time. The inner shell with a BLF  $\Gamma_i$  is a faster moving shell that eventually catches up with the outer shell resulting in an inelastic collision. The widths of the inner and outer shells are  $\Delta_i$  and  $\Delta_o$ , respectively.

### 4.3.1 Collision Parameters

I assume the ejection of an outer shell with mass  $M_o$ , width  $\Delta_o$  and a BLF  $\Gamma_o$ , and an inner shell of mass  $M_i$ , width  $\Delta_i$  and BLF  $\Gamma_i$  separated by a time interval  $t_s$ . The radius,  $R$ , of both the shells has been assumed to be equal to each other and to that of the collimated jet. Assuming the  $z$ -axis to be along the axis of the jet and the radius of the jet to be perpendicular to this axis, I consider that at time  $t = 0$ , the outer shell is at a distance  $z_o$  and the inner shell is at a distance  $z_i$  from the central engine. Here, the distances are being measured from the base of the jet to the outer side of each shell. Then, the time of collision,  $\delta t$  is given by (Kobayashi et al. 1997)

$$\delta t = \frac{(z_o - z_i - \Delta_i)}{c(\beta_i - \beta_o)} \quad (4.5)$$

and the position at which the two shells collide, which also defines the location of the CD, is given by

$$z_c = z_i + c\beta_i\delta t . \quad (4.6)$$

Considering the collision of these two shells to be an inelastic one, the BLF and the total internal energy of the merged shell can be obtained by using the conservation of momentum and energy. This yields

$$\Gamma_m = \sqrt{\frac{M_i\Gamma_i + M_o\Gamma_o}{\frac{M_i}{\Gamma_i} + \frac{M_o}{\Gamma_o}}} \quad (4.7)$$

and

$$E_{\text{int}} = M_i c^2 (\Gamma_i - \Gamma_m) + M_o c^2 (\Gamma_o - \Gamma_m) . \quad (4.8)$$

I am assuming the internal energy of an individual shell to be negligible and all the energy is stored as the bulk kinetic energy of the shell. The efficiency of conversion of the bulk kinetic energy of the shells into the internal energy of the merged shell from a single collision, that is the ratio of the internal energy of the merged shell to the total kinetic energy of the two shells, is given by

$$\eta = 1 - \left[ \frac{(M_i + M_o)\Gamma_m}{(M_i\Gamma_i + M_o\Gamma_o)} \right] . \quad (4.9)$$

As a result of shock propagation, the emission regions keep increasing until the two shocks reach the respective boundaries of the merged shell as shown in Figure 4.3.

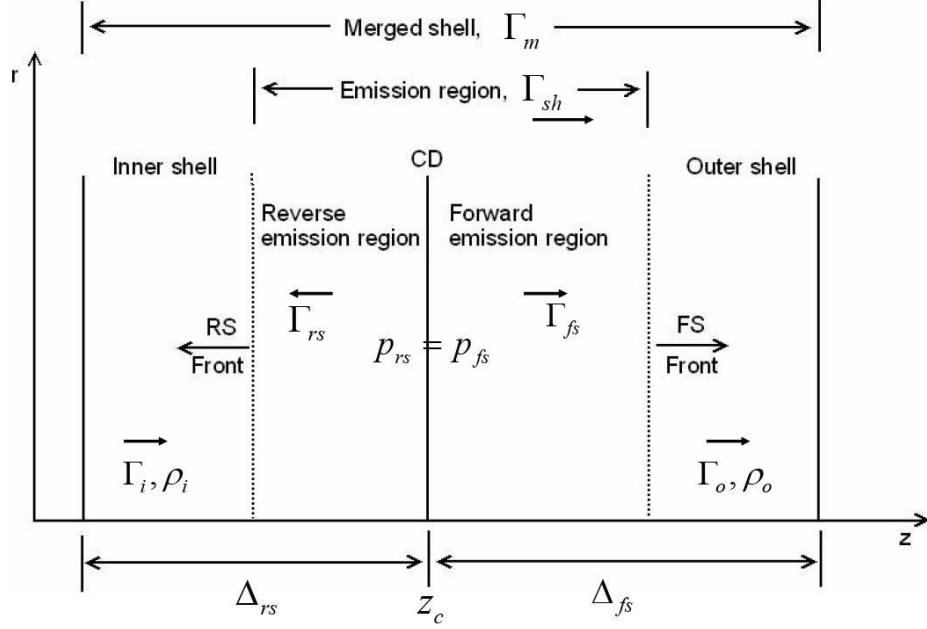


Figure 4.3: Diagram of the two-shell inelastic collision resulting in a merged shell of BLF  $\Gamma_m$ . The FS and RS fronts start to propagate in the outer and inner shells, respectively, creating the forward and reverse emission regions. In the comoving frame, the shock fronts move with a BLF  $\Gamma_{fs}$  and  $\Gamma_{rs}$ . The CD is located at a distance  $z_c$  from the central engine. The comoving pressures  $p_{fs}$  and  $p_{rs}$  and velocities of the shocked fluids across the CD are equal. Only the forward and reverse emission regions are filled up with ultra-relativistic electrons. The emission regions keep expanding sideways until the FS and RS reach the boundary of forward and reverse regions, respectively.

The BLF of the entire emission region in the lab frame,  $\Gamma_{sh}$ , is calculated by using relativistic hydrodynamic Rankine-Hugoniot jump conditions, for energy and particle density across both the shock fronts and the condition of equal pressure and velocity of the shocked fluids across the CD (S01). Since the jump equations for both the FS

and RS regions are similar, I will mention the jump equations for the forward region only. The Rankine-Hugoniot jump equations for the internal energy,  $E_{\text{fs}}$ , and the matter density of baryons,  $\rho_{\text{fs}}$ , in the comoving frame of the forward region are given by (S01)

$$\frac{E_{\text{fs}}}{\rho_{\text{fs}}} = c^2 (\Gamma_{\text{sh,o}} - 1) \quad (4.10)$$

and

$$\frac{\rho_{\text{fs}}}{\rho_{\text{o}}} = \frac{(\hat{\gamma}\Gamma_{\text{sh,o}} + 1)}{(\hat{\gamma} - 1)} . \quad (4.11)$$

Here,  $\rho_{\text{o}}$  is the baryon density of the preshocked fluid in the comoving frame of the forward region,  $\hat{\gamma}$  is the adiabatic index whose value has been assumed to be  $4/3$ , (typical value for a plasma in relativistic hydrodynamics), and  $\Gamma_{\text{sh,o}}$  is the BLF of the emission region in the frame of the outer shell. The  $\Gamma_{\text{fs}} = \Gamma_{\text{sh,o}}$  in the comoving frame of the shocked fluid.

The pressure of the forward region is obtained from equations 4.10 and 4.11 and is given by

$$p_{\text{fs}} = (\Gamma_{\text{sh,o}} - 1) (\hat{\gamma}\Gamma_{\text{sh,o}} + 1) \rho_{\text{o}} c^2 . \quad (4.12)$$

The condition of equal pressures and velocities of the shocked fluids across the CD yields a quartic equation in  $\Gamma_{\text{sh}}$ . The following equation is solved numerically to obtain the value of  $\Gamma_{\text{sh}}$  (S01):

$$\begin{aligned} & \hat{\gamma} (g^4 - Y) x^4 + 2g (\hat{\gamma} - 1) (Y - g^2) x^3 + 2g^2 (2 - \hat{\gamma}) (Y - 1) x^2 \\ & + 2g (\hat{\gamma} - 1) (g^2 Y - 1) x + \hat{\gamma} (1 - g^4 Y) = 0 , \end{aligned} \quad (4.13)$$

where  $x = \Gamma_{\text{sh}}/\sqrt{\Gamma_o\Gamma_i}$ ,  $g = \sqrt{\frac{\Gamma_i}{\Gamma_o}}$  ( $1/g < x < g$ ), and  $Y = \rho_o/\rho_i$ .

The widths of the forward as well as the reverse region in the lab frame are obtained using equation 4.11, and are given by (S01)

$$\Delta_{\text{fs}} = \Delta_o \left( \frac{\rho_o}{\rho_{\text{fs}}} \right), \Delta_{\text{rs}} = \Delta_i \left( \frac{\rho_i}{\rho_{\text{rs}}} \right) . \quad (4.14)$$

Similarly, the internal energies, in the lab frame, of both the shocked regions are obtained using the equality of velocities of the two shocks across the CD and is given by (S01)

$$E_{\text{fs}} = \frac{E_{\text{int}}}{\left(1 + \frac{\Delta_{\text{rs}}}{\Delta_{\text{fs}}}\right)}, E_{\text{rs}} = \frac{\Delta_{\text{rs}} E_{\text{int}}}{\Delta_{\text{fs}} \left(1 + \frac{\Delta_{\text{rs}}}{\Delta_{\text{fs}}}\right)} . \quad (4.15)$$

The time of crossing the forward or reverse region by the FS or RS, in the comoving frame, can then be obtained by using the corresponding comoving shell width ( $\Delta'$ ) and shock velocity, and is given by

$$t'_{\text{cr,fs(rs)}} = \frac{\Delta'_{\text{fs(rs)}}}{c\beta_{\text{fs(rs)}}} . \quad (4.16)$$

### 4.3.2 Emission region parameters

The calculation of radiative processes is dependent of the values of various parameters, such as the magnetic field ( $B$ ), minimum ( $\gamma_{\min}$ ) and maximum ( $\gamma_{\max}$ ) random Lorentz factor (RLF) of the electrons, and the normalization factor,  $Q_0^{\text{inj}}$  ( $\text{cm}^{-3}\text{s}^{-1}$ ) of the electron injection function  $Q_e^{\text{inj}}(\gamma, t) = Q_{0,\text{fs}}^{\text{inj}}(t)\gamma_{\text{fs}}^{-q}$  ( $\text{cm}^{-3}\text{s}^{-1}$ ). In order to proceed with the calculation of the radiative processes, I first derive the values of these parameters from the shock dynamics (see below) for each of the shocked regions separately. I then calculate the radiative energy loss rates of electrons and corresponding photon emissivities for both the regions separately and then add their respective contributions to the observed spectrum accordingly. Since the equations for both the regions are similar, I will mention the equations for the forward region only, in this as well as in the rest of the sections of this chapter, unless otherwise stated. Primed quantities are all calculated in the comoving frame of the shocked fluid. Quantities like the particle spectral index of the injected electron population,  $q$ ,  $\gamma_{\min}$ , and  $\gamma_{\max}$ , although unprimed, also refer to the comoving frame, and the rest of the unprimed quantities all refer to the lab frame.

Since some of the bulk kinetic energy of the colliding shells gets converted into the magnetic and electron energy by the resulting shocks, the value of the magnetic field in the forward region is obtained using the equation

$$U'_{\text{B,fs}} = \varepsilon_{\text{B}} U'_{\text{fs}} , \quad (4.17)$$

where  $U'_{\text{fs}} = E_{\text{fs}}/(\Gamma_{\text{sh}}^2 \pi R^2 \Delta_{\text{fs}})$  is the internal energy density of the shocked fluid in the forward region, and  $R$  is the radius of this cylindrical region. The  $U'_{\text{B,fs}} = B_{\text{fs}}'^2/8\pi$  is the magnetic energy density and  $\varepsilon_{\text{B}}$  is the fraction of  $U'_{\text{fs}}$  stored in  $U'_{\text{B,fs}}$ . Equation 4.17 yields the value of the magnetic field, which is assumed to be randomly oriented in space:

$$B'_{\text{fs}} = \left( \frac{1}{\Gamma_{\text{sh}}} \right) \sqrt{\frac{8\varepsilon_{\text{B}} E_{\text{fs}}}{R^2 \Delta_{\text{fs}}}} . \quad (4.18)$$

The maximum RLF of the injected electrons, on the other hand, is obtained by balancing the power gained from the acceleration from both the shock and the gyroresonant processes with the synchrotron losses as these losses are expected to dominate at the highest energies (Chiang and Dermer 1999; de Jager and Harding 1992). This condition yields

$$\gamma_{\text{max,fs}} = 4.6 \times 10^7 \sqrt{\frac{\alpha}{B'_{\text{fs}}}} , \quad (4.19)$$

where  $\alpha \leq 1$  is the electron acceleration rate parameter.

The minimum RLF of the injected electrons in the forward region resulting from the propagation of the FS through the region is obtained by using the equation

$$U'_{\text{e,fs}} = \varepsilon_{\text{e}} U'_{\text{fs}} . \quad (4.20)$$

Here,  $U'_{\text{e,fs}} = n'_{\text{e,fs}} \langle \gamma_{\text{fs}} \rangle m_e c^2$  is the electron energy density,  $n'_{\text{e,fs}} = \zeta_e \frac{\rho_{\text{fs}}}{m_p}$  is the number density of non-thermal electrons injected by the FS into the forward shock region,

and  $\varepsilon_e$  is the fraction of  $U'_{\text{fs}}$  stored in  $U'_{e,\text{fs}}$ . The average electron energy  $\langle \gamma_{\text{fs}} \rangle$  for the energy range  $\gamma_{\text{min,fs}} < \gamma_{\text{fs}} < \gamma_{\text{max,fs}}$ , in the comoving frame, is given by

$$\langle \gamma_{\text{fs}} \rangle = \frac{\int_{\gamma_{\text{min,fs}}}^{\gamma_{\text{max,fs}}} n'_{e,\text{fs}}(\gamma_{\text{fs}}) \gamma_{\text{fs}} d\gamma_{\text{fs}}}{\int_{\gamma_{\text{min,fs}}}^{\gamma_{\text{max,fs}}} n'_{e,\text{fs}}(\gamma_{\text{fs}}) d\gamma_{\text{fs}}} . \quad (4.21)$$

Here,  $n'_{e,\text{fs}}(\gamma_{\text{fs}}) = n'_o \gamma_{\text{fs}}^{-q}$  is the injected electron number density per unit  $\gamma_{\text{fs}}$ . Substituting all the above expressions along with the equation 4.19 in equation 4.20 and writing  $U'_{\text{fs}} = n'_{p,\text{fs}} \Gamma_{\text{fs}} m_p c^2$ , as most of the internal energy of the shock is stored in the baryons, I obtain the expressions for  $\gamma_{\text{min,fs}}$  to be

$$\begin{aligned} 1837 \frac{\varepsilon_e}{\zeta_e} \Gamma_{\text{fs}} \ln(\gamma_{\text{min,fs}}) - \gamma_{\text{min,fs}} + \gamma_{\text{max,fs}} - 1837 \frac{\varepsilon_e}{\zeta_e} \Gamma_{\text{fs}} \ln(\gamma_{\text{max,fs}}) &= 0 \quad \text{if } q = 1, \\ \ln(\gamma_{\text{min,fs}}) + 1837 \frac{\varepsilon_e}{\zeta_e} \frac{\Gamma_{\text{fs}}}{\gamma_{\text{min,fs}}} - \ln(\gamma_{\text{max,fs}}) - 1837 \frac{\varepsilon_e}{\zeta_e} \frac{\Gamma_{\text{fs}}}{\gamma_{\text{max,fs}}} &= 0 \quad \text{if } q = 2, \\ \gamma_{\text{min,fs}}^{2-q} - C \gamma_{\text{min,fs}}^{1-q} - \gamma_{\text{max,fs}}^{1-q} (\gamma_{\text{max,fs}} - C) &= 0 \\ &\text{if } q \neq 1 \text{ or } 2 , \end{aligned} \quad (4.22)$$

where  $C = 1837 \left( \frac{q-2}{q-1} \right) \left( \frac{\varepsilon_e \Gamma_{\text{fs}}}{\zeta_e} \right)$ , and  $\zeta_e$  is the fraction of electrons that are effectively accelerated. Equation 4.22 is solved numerically to obtain the value of  $\gamma_{\text{min,fs}}$ . In case of  $\gamma_{\text{max}} \gg \gamma_{\text{min}}$  and  $q > 2$ , the above expressions reduce to

$$\gamma_{\text{min}} = 1837 \frac{q-2}{q-1} \frac{\varepsilon_e}{\zeta_e} \Gamma_{\text{fs}} \quad (4.23)$$

The normalization factor of the injection function is determined by requiring that the electrons are accelerated as long as the shock is present in the region. The electrons that are closer to the shock front are accelerated behind the shock. The value of  $Q_{0,\text{fs}}^{\text{inj}}(t)$  for a zone is obtained by assuming that the energy density available per unit time to accelerate the non-thermal electrons is a fraction of the rate of change of internal energy stored in the shock (Mimica et al. 2004). This yields

$$\frac{\zeta_e E'_{\text{fs}}}{t'_{\text{cr,fs}}} = V'_{\text{fs}} \int_{\gamma_{\text{min,fs}}}^{\gamma_{\text{max,fs}}} Q_{e,\text{fs}}^{\text{inj}}(\gamma_{\text{fs}}, t) \gamma_{\text{fs}} m_e c^2 d\gamma_{\text{fs}} . \quad (4.24)$$

Using equation 4.24, I obtain the expression for  $Q_{0,\text{fs}}^{\text{inj}}(t)$  as

$$Q_{0,\text{fs}}^{\text{inj}}(t) = \begin{cases} \frac{\zeta_e E'_{\text{fs}} (2-q)}{V'_{\text{fs}} m_e c^2 t'_{\text{cr,fs}} (\gamma_{\text{max,fs}}^{2-q} - \gamma_{\text{min,fs}}^{2-q})} & \text{if } q \neq 2 \\ \frac{\zeta_e E'_{\text{fs}}}{V'_{\text{fs}} m_e c^2 t'_{\text{cr,fs}} \ln(\gamma_{\text{max,fs}}/\gamma_{\text{min,fs}})} & \text{if } q = 2 . \end{cases} \quad (4.25)$$

where  $E'_{\text{fs}} = \frac{E_{\text{fs}}}{\Gamma_{\text{sh}}}$  is the internal energy, and  $V'_{\text{fs}} = \pi R^2 \Delta'_{\text{fs}}$  is the volume of the forward region.

## 4.4 Photon Escape Timescale

In the case of a cylindrical region, the volume and angle averaged photon escape timescale is not the same as that of a spherical one. This quantity is important for numerical computation of the evolution of the particle and photon population inside

the emission region. The average photon escape timescale also yields an estimate of the mean free path for photons in the case of synchrotron self absorption (SSA) as well as  $\gamma - \gamma$  absorption. Thus, the need to find an expression for the average photon escape timescale for a cylindrical region is evident. To carry out this work, I have derived an analytical expression for the escape timescale of a photon for a cylindrical region, which to the best of my knowledge has been derived for the first time ever.

In order to obtain the expression for the escape timescale in the comoving frame, I consider three possible directions, namely, forward, sideways and backward, in which a photon can possibly escape out of a cylindrical region. All the quantities in this section refer to the comoving frame only, hence the prime notation is not being used. Figure 4.4 depicts the angle considerations for the three possible directions of escape for a photon from a cylindrical region of height (width)  $h$  and radius  $R$ .

As stated earlier, the  $z$ -axis is along the axis of the cylinder. Considering  $l_{\text{esc}+}$  and  $l_{\text{esc}-}$  to be the distance that needs to be covered by a photon travelling in the forward or backward direction to escape out of the region and  $\theta_+$  and  $\pi - \theta_-$  to be the corresponding angles in the two directions respectively. The volume averaged photon escape timescale can then be written as

$$\langle t_{\text{ph,esc,V}} \rangle = \frac{1}{V_{\text{cyl}}} \int_0^R \int_0^h \int_0^{2\pi} \langle t_{\text{ph,esc}}(r, z) \rangle r d\phi dz dr , \quad (4.26)$$

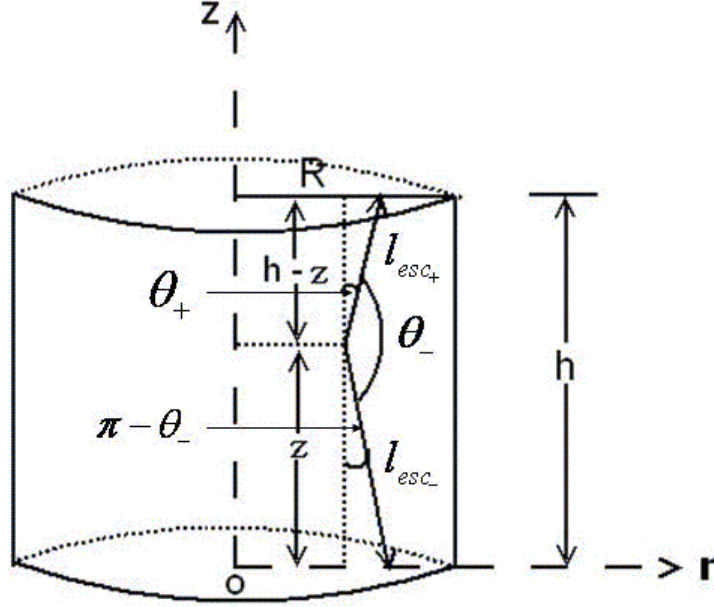


Figure 4.4: Illustration of the three possible directions of escape for a photon from a cylindrical region. The radius,  $R$ , of the cylinder is assumed to be greater than its height,  $h$ . The quantities  $l_{esc+}$  and  $l_{esc-}$  refer to the escape path lengths for a photon in the forward and backward directions, and  $\theta_+$  and  $\pi - \theta_-$  are the corresponding angles.

where the angle averaged escape timescale is written as

$$\langle t_{\text{ph,esc}}(r, z) \rangle = \frac{1}{4\pi c} \int_0^{2\pi} \int_{-1}^{+1} l_{\text{esc}}(\mu, \phi; r, z) d\mu d\phi. \quad (4.27)$$

Here,  $l_{\text{esc}}$  is the distance required to escape from the region in any direction, and  $\mu = \cos \theta$ . I have solved the above integral analytically to obtain the final expression for the volume and angle averaged photon escape timescale for a cylindrical region. The intermediate steps needed to obtain the final expression are given in Appendix

A of this dissertation. The photon escape timescale for a cylindrical region was found to be

$$\langle t_{\text{ph,esc,V}} \rangle = \left( \frac{h}{4c} \right) \ln \left( 1 + \frac{R^2}{h^2} \right) - \left( \frac{R^2}{4ch} \right) \ln \left( 1 + \frac{h^2}{R^2} \right) + \left( \frac{R}{c} \right) \arctan \left( \frac{h}{R} \right). \quad (4.28)$$

Figure 4.5 shows a comparison of the photon escape timescale for cylindrical and spherical geometries as a function of  $(h/R)$ .

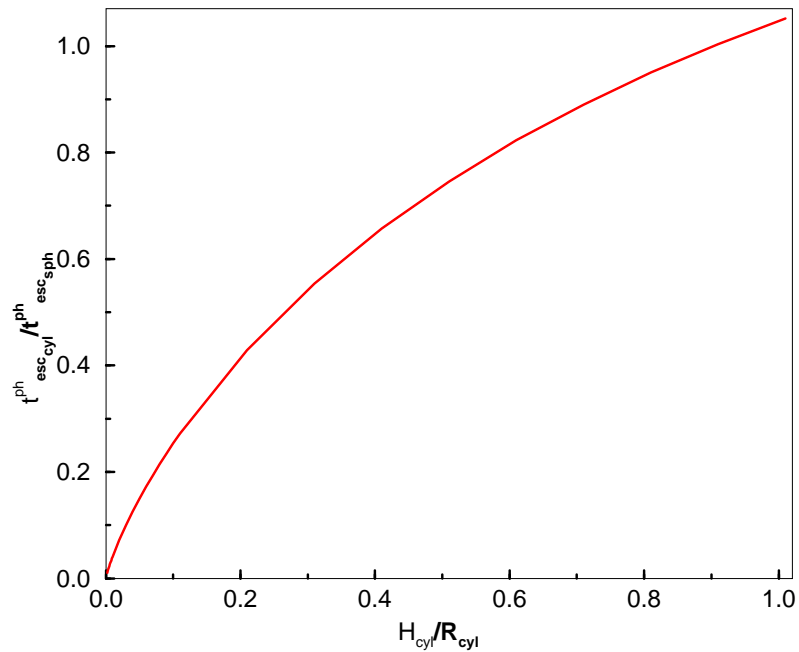


Figure 4.5: Comparison of the volume and angle averaged photon escape timescales for a cylindrical and spherical geometry.

As can be seen from equation 4.28, if  $h = R$ ,  $\langle t_{\text{ph,esc,V}} \rangle = R\pi/4c$ , which is  $\approx (3/4)R/c$ , the photon escape timescale for a spherical region. In the asymptotic limits, the expression for the average photon escape timescale reduces to

$$\langle t_{\text{ph,esc,V}} \rangle = \begin{cases} \left( \frac{h}{4c} \right) [3 + \ln(1 + (\frac{R}{h})^2)] & \text{if } h \ll R \\ \left( \frac{R\pi}{2c} \right) - \left( \frac{R^2}{4ch} \right) [3 + \ln(1 + (\frac{h}{R})^2)] & \text{if } h \gg R \end{cases} \quad (4.29)$$

Equation 4.28 gives the volume and angle averaged photon escape timescale for the entire cylindrical region in any direction. From symmetry consideration, the time needed to escape the region from the backward direction is the same as that of the upward direction. Using the geometry of a cylinder, the probability of escape for a photon in the forward direction, only, is  $P_{\text{fwd}} = \pi R^2 / (2\pi R(R+h))$ . The probability for a photon to go in the backward direction is,  $P_{\text{back}} = P_{\text{fwd}}$ . Similarly, the probability of escape in the sideways direction, only, is  $P_{\text{side}} = 2\pi Rh / (2\pi R(R+h)) = h / (R+h)$ . These probabilities are used to calculate the photon escape rates in the three directions, as described in the next section.

## 4.5 Numerical Method

The emission region parameters and the average photon escape timescale form the necessary set of input parameters required to carry out the calculation of radiative energy loss rates and photon emissivities and follow the evolution of electron and photon populations inside the emission region in a time-dependent manner. All the quantities mentioned in this section refer to the comoving frame and hence the prime notation has not been used. In this model, I consider instantaneous acceleration of

relativistic particles behind the shock front, which are then injected into the region with a single-power-law distribution described by  $Q_e^{\text{inj}}(\gamma) = Q_0^{\text{inj}}\gamma^{-q}$  for  $\gamma_{\text{min}} \leq \gamma \leq \gamma_{\text{max}}$ , where  $Q_0^{\text{inj}}$  is given by equation 4.25,  $\gamma_{\text{min}}$  by equation 4.22, and  $\gamma_{\text{max}}$  by equation 4.19. The acceleration of the particles and the longitudinal expansion of the emission region continues until the shock reaches the respective boundary of the merged shell. As the shock propagates in the region, the more energetic electrons are located at the shock front as that is where they are accelerated while the cooled particles are progressively more distant from the front thereby automatically forming an energy gradient within the emission region.

Once the acceleration sets in, the particles begin to lose their energy via various radiative processes such as synchrotron, SSC, and/or Compton upscattering of external photons (EC). The time-dependent evolution of the electron and photon populations in the emission region is followed by using equations 3.4 and 3.5 of Chapter 3. In order to obtain the temporal evolution of the electron distribution in the emission region, equation 3.4 is rearranged in such a way that it forms a tridiagonal matrix, which is then solved numerically (Chiaberge and Ghisellini 1999; Press et al. 1992).

The synchrotron photon emission rate in the energy interval  $[\epsilon, \epsilon + d\epsilon]$  is calculated using the formula (Crusius and Schlickeiser 1986)

$$\dot{n}_{\text{syn}}(\epsilon) = \frac{\sqrt{3}e^3B}{2\pi h^2\nu} \int_1^\infty R(x)n_{\text{ep}}(\gamma)d\gamma, \quad (4.30)$$

where  $n_{\text{ep}}(\gamma)$  is the particle density in the energy interval  $[\gamma, \gamma + d\gamma]$ .

Synchrotron emission is accompanied by absorption for low-energy photons. In this process, termed as SSA, the photon interacts with an electron of the same population producing the synchrotron radiation and is absorbed, giving up its energy to the electron. As a result, a particular source remains optically thick to its own synchrotron radiation for frequencies below a low-frequency cutoff with the spectrum being  $\propto \nu^{5/2}$  if  $\nu_{\text{SSA}} > \nu_{\text{syn}}$ . Here  $\nu_{\text{SSA}}$  is the frequency of SSA photons in units of  $m_e c^2/h$  and  $\nu_{\text{syn}} = \frac{eB}{2\pi m_e} \gamma_{\text{min}}^2 = 2.8 \times 10^6 B \gamma_{\text{min}}^2$  is the characteristic frequency of synchrotron photons produced from electrons with a Lorentz factor of  $\gamma_{\text{min}}$ . The optically thin part of the synchrotron spectrum of a source, on the other hand, remains  $\propto \nu^{-(q-1)/2}$  (Figure 6.12 [Rybicki and Lightman 1979](#)). I have incorporated this feature of the synchrotron radiation in my calculations. The SSA optical depth is calculated using the formula

$$\tau_{\text{SSA}} = \frac{-l_{\text{ph,esc}} \sqrt{3} e^3 B}{16\pi^2 (m_e c \nu)^2} \int_1^\infty R(x) \gamma^2 \frac{d}{d\gamma} \left( \frac{n_{\text{ep}}(\gamma)}{\gamma^2} \right) d\gamma, \quad (4.31)$$

where  $l_{\text{ph,esc}} = t_{\text{ph,esc}} c$  is the mean free path for a photon escaping from a cylindrical region. The synchrotron emission from a cylindrical region is then obtained using the expression

$$\dot{n}_{\text{syn}}(\epsilon) = \dot{n}_{\text{syn}}(\epsilon) \frac{(1 - \exp^{-\tau_{\text{SSA}}})}{\tau_{\text{SSA}}}. \quad (4.32)$$

I have also used a simplified version of the synchrotron emission formula in the simulations to save CPU time. This version of the synchrotron emission formula is discussed in detail in Section 4.7.

The electron energy loss rate due to scattering an isotropic, monochromatic radiation field of photon energy  $\epsilon$  and density  $n_{\text{ph}}$  ( $\text{cm}^{-3}$ ), including the effects of Klein-Nishina scattering cross section, is calculated using equation 4 of (Böttcher et al. 1997). The SSC photon emission rate of an isotropic SSC emission in the region is calculated by (Jones 1968; Böttcher et al. 1997)

$$\dot{n}_{\text{SSC}}(\epsilon_s, \Omega_s) = \frac{1}{4\pi} \int_1^\infty d\gamma n_{\text{ep}}(\gamma) \int_0^\infty d\epsilon n_{\text{ph}}(\epsilon) g(\epsilon_s, \epsilon, \gamma), \quad (4.33)$$

where  $\epsilon_s$  is the energy of the scattered photon,  $n_{\text{ph}}(\epsilon)$  is the radiation field of photon energy  $\epsilon$  available for SSC scattering in the region, and  $g(\epsilon_s, \epsilon, \gamma)$  is a function that includes the probability of regular Compton scattering, and is given by (Jones 1968)

$$g(\epsilon_s, \epsilon, \gamma) = \begin{cases} \frac{3c\sigma_{\text{T}}}{16\gamma^4\epsilon} \left( \frac{4\gamma^2\epsilon_s}{\epsilon} - 1 \right) & \text{for } \frac{\epsilon}{4\gamma^2} \leq \epsilon_s \leq \epsilon \\ \frac{3c\sigma_{\text{T}}}{4\gamma^2\epsilon} \left[ 2q \ln(q) + (1+2q)(1-q) + \frac{(4\epsilon\gamma q)^2(1-q)}{2(1+4\epsilon\gamma q)} \right] & \text{for } \epsilon \leq \epsilon_s \leq \frac{4\epsilon\gamma^2}{1+4\epsilon\gamma} \end{cases} \quad (4.34)$$

Here,  $q = \epsilon_s/4\epsilon\gamma^2(1 - \epsilon_s/\gamma)$ . The radiation field available for SSC scattering includes contributions from both the synchrotron photon density of the current time step of the simulation and the SSC photon density of the foregoing time step. This way, I have included the higher order SSC scattering in the code. In case of SSC emission,

the optical depth for a  $\gamma$ -ray photon of energy  $\epsilon_1$  due to interaction with lower energy radiation present in the emission region ( $\gamma - \gamma$  absorption) is calculated using the formula (Böttcher et al. 1997)

$$\tau_{\gamma\gamma}(\epsilon_1) = 2\pi l_{\text{ph,esc}} \int_{-1}^{+1} d\mu (1 - \mu) \int_{\frac{2}{\epsilon_1(1-\mu)}}^{\infty} d\epsilon \sigma_{\gamma\gamma}(\epsilon_1, \epsilon, \mu) n_{\text{ph}}(\epsilon) , \quad (4.35)$$

where  $n_{\text{ph}}$  is the photon density present in the emission region that provides the photon field for  $\gamma - \gamma$  absorption and  $\sigma_{\gamma\gamma}$  is the pair production cross-section. The subsequent pair production rate is obtained using equation 26 of Böttcher and Schlickeiser (1997). Using the radiative transfer equation, the high-energy emission that is able to escape from the region can be calculated as

$$\dot{n}_{\text{SSC}}^{\text{esc}}(\epsilon_s, \Omega_s) = \dot{n}_{\text{SSC}}(\epsilon_s, \Omega_s) \frac{(1 - \exp^{-\tau_{\gamma\gamma}})}{\tau_{\gamma\gamma}} . \quad (4.36)$$

The temporal evolution of the photon population inside the emission region, for synchrotron and SSC emission, is followed using equation 3.5. The time step used in the simulations is a fraction of the minimum timescale amongst all the relevant timescales (cooling, electron and photon escape, injection and shock crossing) of both the regions (FS and RS) and is common for the two emission regions. This entire numerical framework is what has been used to calculate the spectrum resulting from a cylindrical emission region with two shocks propagating in the opposite directions in the comoving frame of the region. I describe the method of applying this framework to an emission region divided into various numerical grids (zones) below.

### 4.5.1 The Zone Scheme

In order to reproduce the observed spectral variability patterns of a blazar as accurately as possible, it is important to consider the inhomogeneity in the particle as well as photon density throughout the emission region. Observations in the optical and higher energy bands indicate that the injection and/or cooling timescales can be shorter than the light crossing time for the region (Chiaberge and Ghisellini 1999). As mentioned earlier, the highly energetic electrons that have been accelerated freshly at the shock front evolve on a cooling time scale shorter than the light crossing time while the electrons that are further away from the shock front have had time to strongly cool off. This induces an energy gradient in the electron population within the region and creates an inhomogeneity in the particle as well as photon energy density throughout the emission region. As a result of this, the observer sees a combination of various spectra being produced in different parts of the region (Sokolov et al. 2004; Graff et al. 2008).

In this work, I incorporate the inhomogeneity in the particle and photon densities by dividing the emission region into multiple zones, each of width  $h_z$  and radius  $R$  (same as that of the jet itself). As shown in Figure 4.6, I start with a jet that is entirely devoid of relativistic particles and the first population of ultrarelativistic particles is injected by the shock very close to the CD.

The zone closest to the CD in the forward emission region will have the forward shock propagating through it first. As the shock advances, it injects particles into

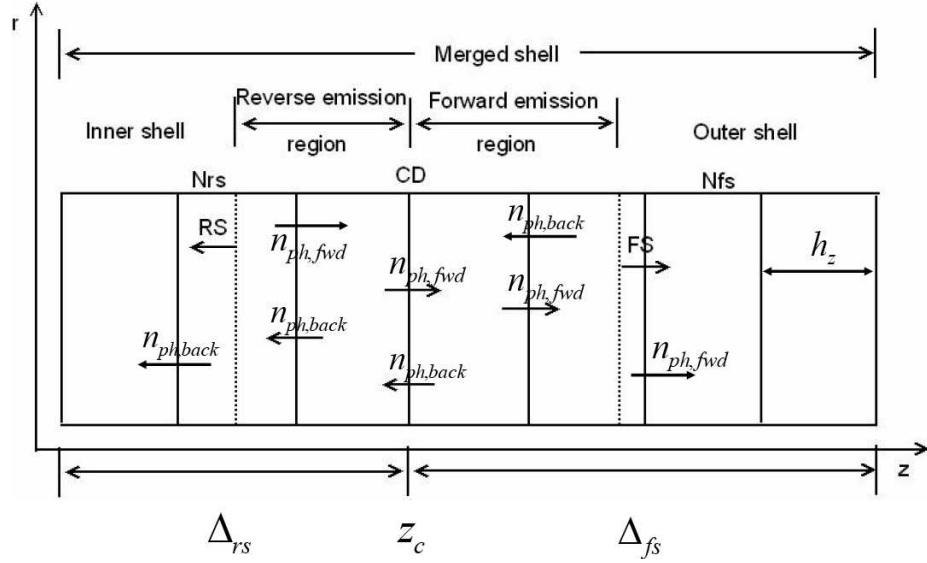


Figure 4.6: Illustration of the zone scheme used to calculate the entire radiation spectrum resulting from the emission regions shown in Fig. 4.3. The entire forward and reverse regions are divided into  $N_{fs}$  and  $N_{rs}$  zones, each of width  $h_z$ . The quantities  $n_{ph,fwd}$ ,  $n_{ph,back}$ , &  $n_{ph,side}$  are the photon escape densities in the forward, backward, and sideways directions delineating the transfer of photons in between the zones throughout the forward and reverse emission regions.

the zone with a power-law distribution dictated by the shock parameters. The normalization factor,  $Q_0^{inj}$  is calculated for every zone using equation 4.25 and replacing  $E'_{fs}$  by  $E'_{fs,zn} = \frac{E'_{fs}}{N_{fs}}$ ,  $V'_{fs}$  by  $V'_{fs,zn} = \frac{V'_{fs}}{N_{fs}}$ , and  $t'_{cr,fs}$  by  $t'_{cr,fs,zn} = \frac{h_z}{\beta_{rs}c}$ . The electrons are accelerated at the shock front and the subsequent electron and photon population is followed according to the method described above, at every time step. As the shock enters a new zone, it gradually populates that zone and the entire process of injection, acceleration and cooling is repeated. The injection and acceleration stops in the previous zone, which the shock had just left, and only the cooling continues. As shown in Figure 4.6, once the photon density of the zone closest to the CD is calculated for the current time step, the photon escape rates for the forward, backward, and

sideways directions are calculated for the same time step using  $P_{\text{fwd}}$ ,  $P_{\text{back}}$ , and  $P_{\text{side}}$ , as mentioned in Section 4.4, in the following manner

$$\frac{dn_{\text{ph,fwd}}(\epsilon, \Omega)}{dt} = \frac{n_{\text{ph}}(\epsilon, \Omega)}{t_{\text{ph,esc}}} P_{\text{fwd}} \quad (4.37)$$

and

$$\frac{dn_{\text{ph,side}}(\epsilon, \Omega)}{dt} = \frac{n_{\text{ph}}(\epsilon, \Omega)}{t_{\text{ph,esc}}} P_{\text{side}} \quad (4.38)$$

with  $dn_{\text{ph,back}}(\epsilon, \Omega) = dn_{\text{ph,fwd}}(\epsilon, \Omega)$ . The sideways propagating photon density becomes part of the observed spectrum originating from that zone. The forward and backward propagating photon densities are used to provide feedback to their neighbouring zones in both the directions. The following equation shows how the photon density rate of zone  $i$  is calculated for the current timestep using the photon density rates from equations 4.32 and 4.36 for the current time step and the feedback of photon density rates from zones  $i+1$  and  $i-1$  from the previous time step:

$$\dot{n}_{\text{ph}}(\epsilon, \Omega, i) = \dot{n}_{\text{syn}}(\epsilon, \Omega, i) + \dot{n}_{\text{ssc}}(\epsilon, \Omega, i) + \dot{n}_{\text{ph,fwd}}(\epsilon, \Omega, i-1) + \dot{n}_{\text{ph,back}}(\epsilon, \Omega, i+1) \quad (4.39)$$

The total photon density of zone  $i$  for the current time step is then given by

$$n_{\text{ph}}^{\text{curnt}}(\epsilon, \Omega, i) = n_{\text{ph}}^{\text{prev}}(\epsilon, \Omega, i) + (\dot{n}_{\text{ph}}(\epsilon, \Omega, i) \times dt) , \quad (4.40)$$

where  $dt$  refers to the current time step. The density of photons escaping from the region, in all the three possible directions, is subtracted from this total density for

the current time step according to the following equation

$$n_{\text{ph}}^{\text{curnt}}(\epsilon, \Omega, i) = n_{\text{ph}}^{\text{curnt}}(\epsilon, \Omega, i) - ((\dot{n}_{\text{ph},\text{fwd}}(\epsilon, \Omega, i) + \dot{n}_{\text{ph},\text{back}}(\epsilon, \Omega, i) + \dot{n}_{\text{ph},\text{side}}(\epsilon, \Omega, i)) \times dt) \quad (4.41)$$

The leftover density is then used for subsequent calculations in the next time step. The process of updating the photon density at every time step and using the updated density for calculations in the next time step continues for as long as the simulation runs. The process of providing photon feedback from a particular zone to its adjacent zones throughout the emission region (forward and reverse) at every time step accounts for the inhomogeneity in the photon density that is present in the jet. In this manner, the total photon density is calculated for all the zones at each time step by treating each zone in the region, individually as well as together with the other zones. The zone+feedback scheme automatically lets me incorporate the non-locality and the time-delayed effect of the photon population in the calculations of the SSC process without having to invoke the need for calculating the photon density rates at retarded times (see [Sokolov et al. 2004](#); [Graff et al. 2008](#)). As appropriately pointed out by [Graff et al. \(2008\)](#), calculation of the non-local, time-retarded SSC losses due to photons produced in other parts of the source is very important for blazars, especially for the SSC dominated sources, such as TeV blazars, and hence cannot be ignored. A similar analysis is carried out for the reverse emission region as well.

## 4.6 Time Delays

In order to calculate the radiation from a source in the observer's frame correctly, I have incorporated the time delays that are introduced because photons travel with a finite speed. As a result, in case of an extended source, different distances that the photons originating from the far end of the source would cover as compared to the photons coming from the near end of the source to reach the observer at the same time, need to be taken into account. Since the emission region under consideration is a cylinder with three possible directions of escape, I consider the time delays in all the three directions. But, in case of blazars, since the emission region is always moving towards us, with the axis of the jet making an angle  $\theta_{obs}$  with the observer's line of sight in the observer's frame, I do not consider the radiation emitted in any direction other than along  $\theta_{obs}$ . Thus, I am considering the time delays in the sideways direction for both the forward and reverse emission region and the time delays in the forward direction for only the forward emission region.

In case of the sideways direction, the time delay equation for the  $i_{fs}^{th}$  zone of width  $h'_{z,fs}$  in the forward emission region is

$$\Delta t'_{side,fs}(i_{fs}) = \frac{(N_{tot} - i_{fs} - 1)h'_{z,fs} \cos \theta'}{c} , \quad (4.42)$$

where the primed quantities refer to the comoving frame,  $N_{tot} = N_{fs} + N_{rs}$  is the total number of zones in the entire emission region, and  $\theta'$  is the orientation angle of the

jet with respect to the observer's line of sight in the comoving frame. In case of the reverse region, the equation for the  $i_{\text{fs}}^{\text{th}}$  zone of width  $h'_{z,\text{rs}}$  becomes

$$\Delta t'_{\text{side,rs}}(i_{\text{rs}}) = \frac{((N_{\text{rs}} - i_{\text{rs}} - 1)h'_{z,\text{rs}} + h'_{z,\text{fs}}N_{\text{fs}}) \cos \theta'}{c} . \quad (4.43)$$

The distance calculation in both the equations 4.42 and 4.43 becomes effective either when the shocks completely exit their respective regions or exit an accelerating zone. Until then, the distances in both the regions are calculated according to the formulae

$$l'_{\text{fs}} = N_{\text{fs}}h'_{z,\text{fs}} - c\beta_{\text{fs}}t' \quad (4.44)$$

and

$$l'_{\text{rs}} = N_{\text{fs}}h'_{z,\text{fs}} + c\beta_{\text{rs}}t' , \quad (4.45)$$

where  $t'$  is the total simulation time elapsed at the current time step,  $dt$ , in the comoving frame. I am doing this, primarily to incorporate the fact that during the injection and acceleration process, when the zones in front of the shock are still devoid of ultra-relativistic particles and hence are inactive, the photons originating from an accelerating zone are always going to stay ahead of the shock front until the shock front enters the consecutive zone making the previous zone non-accelerating. As a result, it is important to calculate the distance travelled by the photons originating from the current location of the shock front in the zone instead of the location of the zone in the region. Once the shock exits the accelerating zone and enters the consecutive inactive zone, the previous zone would start radiating from everywhere by

then and hence the distance travelled by a photon originating from such a zone could be calculated with respect to the zone position instead of the shock front position. I carry out this process for different zones at different times depending on the location of the shock front with respect to a zone for as long as the shock is present in a particular emission region.

Similarly, for the forward time-delay calculation, the distance is calculated according to equation 4.44 and the time-delay equation is given by

$$\Delta t'_{\text{up,fs}} = \frac{l'_{\text{fs}}}{c} . \quad (4.46)$$

I calculate the forward time-delay for as long as the shock is inside the forward emission region. Once the shock leaves the region, only the forward radiation originating from the zone closest to the observer's line of sight will be getting registered by the observer as the rest of the forward radiation from the previous zones will get used in providing the feedback to the adjacent zones.

In addition to the above mentioned time delays, the beaming of the radiation as observed in the observer's frame also needs to be included. The beaming effect is caused due to the overall motion of the entire emission region towards us as seen from our frame of reference. This effect is equivalent to the Doppler effect of a moving light source towards us and can be incorporated using the Doppler boosting factor that connects the comoving frame of the emission region to the observer's frame, by,  $D = [\Gamma_{\text{sh}}(1 - \beta_{\text{sh}} \cos \theta_{\text{obs}})]^{-1}$ . I assume that there is no time delay (forward or sideways) involved for the photons originating from the closest zone in reaching the observer

other than the Doppler boosting effect. The frequencies have been transformed into the observer's frame by multiplying by  $D$ , whereas the fluxes have been transformed by multiplying by  $D^2$ .

The total time-delay in the reception of the photons in either of the directions, in the observer's frame, for an  $i^{th}$  zone of an emission region is given by

$$t_{\text{side,fs(rs);up,fs}}^{\text{obs}} = \frac{1+z}{D} (t + \Delta t'_{\text{side,fs(rs);up,fs}}(i)) \quad , \quad (4.47)$$

where  $z$  is the redshift of a given source and the  $1+z$  term takes care of the cosmological redshift experienced by the radiation due to the physical distance of the source from the observer. In this manner, the total observed time is calculated and rounded off to its next integer value in seconds at every time step for each of the active zones in each of the region. The flux values of every zone are written into a file with the corresponding time value of that zone as its index. Since the different flux files contain information about their respective time values, the flux values of all those files having the same time indices are added and written into one common flux file having the same time index.

## 4.7 Synchrotron Function Fitting

As mentioned in Section 4.5, the synchrotron photon density can be calculated using equation 4.30 where  $R(x)$  is given by (Crusius and Schlickeiser 1986)

$$R(x) = \frac{\pi x}{2} [W_{0, \frac{4}{3}}(x)W_{0, \frac{1}{3}}(x) - W_{\frac{1}{2}, \frac{5}{6}}(x)W_{\frac{-1}{2}, \frac{5}{6}}(x)] . \quad (4.48)$$

Here,  $x = \frac{4.0\pi m_e c\nu}{3eB\gamma^2}$  and  $W_{\lambda, \mu}(x)$  denotes Whittaker's function (Abramowitz and Stegun 1970).

In order to save CPU time in the computation of synchrotron photon density, I have numerically approximated  $R(x)$  as follows:

$$R(x) = C1x^{p1}e^{-x} - C2x^{-p2}e^{-x} , \quad (4.49)$$

where  $C1 = 1.08895$ ,  $C2 = 2.35861 \times 10^{-3}$ ,  $p1 = 0.20949$ , and  $p2 = 0.79051$ . The above expression can be used for any value of  $x$  without having to use the asymptotic expansions of Whittaker functions given by Crusius and Schlickeiser (1986) for small ( $x \ll 1$ ) and large ( $x \gg 1$ ) values of  $x$ .

Since  $R(x)$  has been approximated for the expression given in equation 4.48, the approximation has to be normalized at lower values of  $x$  where  $R(x)$  is  $\propto x^{1/3}$  in order to obtain a good fit to the exact expression for the entire range of normalized frequency,  $x$ , values. This has been carried out by using the following equation to

normalize the approximation according to the  $\frac{1}{3}$ <sup>rd</sup> power-law for all those frequencies that are a fraction of the characteristic frequency,  $\nu_{\text{syn}}$ , at  $\gamma_{\text{min}}$ :

$$R(x) = \left( \frac{\nu}{\nu_{\text{norm}}} \right)^{1/3} R(x), \quad (4.50)$$

where  $\nu_{\text{norm}} = 0.01 \times \nu_{\text{syn}}$ . The fraction has been chosen such that beyond this value the fit to the exact expression remains unaffected. Figure 4.7 shows the comparison of a simulated SED of a blazar source obtained from using the approximation and the exact expression. As can be seen from the figure, the approximation is accurate to  $\sim 0.5\%$  for the entire frequency range.

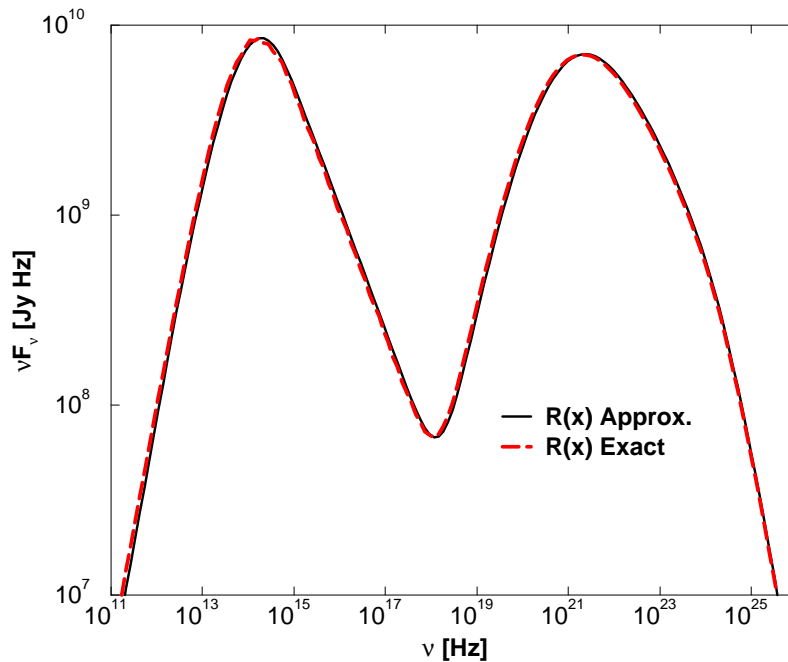


Figure 4.7: Comparison of the exact expression and numerical approximation of  $R(x)$ . The fit is accurate to  $\sim 0.5\%$  for the entire frequency range.

## 4.8 Summary

The aim of the work presented here is to understand the acceleration of relativistic particles and the geometrical structure of the acceleration region at sub-pc scales inside blazar jets. Eventually, the fully-developed code will be used to reproduce the SEDs and spectral variability patterns of blazars, especially those of the potential future TeV sources, with the aim of constraining the dominant acceleration mechanism in such objects.

In order to carry out with this work, the internal shock model was used to accelerate the particles in a generic relativistic jet. A single inelastic collision between two shells of plasma of different mass, velocity, and energy content, was invoked to result in the formation of two internal shocks, namely the FS and the RS, moving with relativistic velocities and separated by a CD. The FS, RS, CD, and the shocked plasma of the resultant emission region all move with the same speed in the forward direction, whereas the FS and RS move with different speeds and in opposite directions in the comoving frame of the shocked plasma. The characteristics of the shock dynamics were obtained by solving the hydrodynamic Rankine-Hugoniot jump conditions across the shock fronts for a relativistic case. The BLF of the emission region, in the lab frame, was obtained using the equality of pressures and velocities of the shocked fluids, of the RS and FS emission region, across the CD.

The BLF of the emission region along with other relevant shock parameters were used to obtain the parameters for the FS and RS emission region in the comoving

frame of the shocked fluid. The emission region parameters, such as  $\gamma_{\max}$ ,  $\gamma_{\min}$ , and  $B$  were then used to calculate the radiation spectrum resulting from the collision. In order to proceed with the calculation of the resultant spectrum, a cylindrical emitting region was assumed, which was divided into multiple zones. The reason for dividing the single emission region into multiple zones is primarily to facilitate the numerical computation of the inhomogeneity in the photon density and make it trackable throughout the region. The subsequent time-dependent radiation transfer within each zone and in between zones was then considered by including the appropriate photon escape probability functions of the zones in the code. I have calculated these functions, independent of any journal source, for a cylindrical region. The zone+feedback scheme used in this work inherently addresses the non-locality and time-delays of the SSC emission of a blazar source.

The radiation resulting from the RS and FS emission region was calculated separately and was added after accounting for the time-delay effect. The time-delay effect for an extended source with a cylindrical geometry arises due to the finiteness of the photon velocity and hence due to the different distances covered by the photons, originating from different points in the region, in reaching the observer at the same time. For the cylindrical emission region, time-delays in the forward and sideways directions were considered for the FS emission region whereas only the sideways direction was considered for the time-delay calculation of the RS emission region.

I have also worked with a numerical simplification of the synchrotron emission formula in order to speed up the computing time. The numerical expression that I obtained resulted in a very good match of the synchrotron component of the SED with the synchrotron component obtained from using the exact expression of  $R(x)$ , in the frequency range of interest. The numerical simplification also resulted in a good match of the overall SED of a generic blazar source, that included the SSC component, with that obtained from using the exact expression of  $R(x)$  to an accuracy of better than 1%.

## CHAPTER 5

# Modeling Results and Acceleration Scenarios

### 5.1 Parameter Study

The combination of shock, emission region, and jet parameters dictates the overall evolution of the radiation spectrum in the simulations. Thus, it is important to understand the effects of varying these parameters on the evolution of the SED and lightcurves of a source in order to reproduce the various observed features. The shock parameters that affect the overall evolution of the SED are the wind luminosity (i.e. the kinetic luminosity associated with bulk motion)  $L_w$ , the total duration of the wind  $t_w$ , the mass of the outer shell  $M_o$ , and the widths and BLFs of the inner and outer shells  $\Delta_i$  &  $\Gamma_i$  and  $\Delta_o$  &  $\Gamma_o$ . The emission region parameters that have an impact on the evolution of the radiation spectrum are the equipartition parameters  $\varepsilon_e$  &  $\varepsilon_B$  (see Section 4.3.2), the particle acceleration fraction  $\zeta_e$ , the acceleration timescale parameter  $\alpha$ , the particle spectral index  $q$ , the radius of the zones and the jet  $R$ . Finally, the jet parameter that plays a role in the evolution of the spectrum is the orientation angle of the jet in the observer's frame,  $\theta_{\text{obs}}$ .

The code was first tested and the effects of varying the values of each of the above mentioned parameters on the time-averaged simulated SEDs were studied. Approximately 30 simulations were carried out to test the code in various regimes. For all our simulations, I have calculated flux values for the frequency range  $\nu = (1.0 \times 10^7 - 1.0 \times 10^{27})$  Hz, in the comoving frame, and the electron energy distribution (EED) range  $\gamma = 10 - 1.0 \times 10^8$  (in the comoving frame) with both ranges divided into 200 grid points. The entire emission region has been divided into 20 zones with 10 zones in the forward and 10 in the reverse shock region. Before proceeding with the simulations, the values of some of the parameters are analytically tested to make sure that unphysical values are not used in the simulations. The acceleration time scale of the highest energy electron should be less than their corresponding synchrotron cooling timescale. This condition has been used to place an upper limit on the value of  $\gamma_{\max}$  for the particles in both the forward and reverse shock emission regions. The value should satisfy the following condition

$$\gamma_{\max} \leq \sqrt{\frac{3e}{B\sigma_{\text{T}}}}, \quad (5.1)$$

where  $e = 4.8 \times 10^{-10}$  esu is the electron's charge in cgs units. Also the value of  $\gamma_{\max}$  should not exceed the maximum value of the EED range, mentioned above. In case of  $\gamma_{\min}$ , the value should not fall below the lowest value of the EED range. As pointed out by [Mimica et al. \(2004\)](#), the Larmor radius,  $r_{\text{L}}$ , of the fastest moving (highest-energy) electron should be smaller than the zone width so that the magnetic

field strength exceeds a certain minimum value and the shock acceleration can take place. This condition has been used to make sure that the number of zones for both regions are selected in such a way that

$$\frac{r_L}{h_z} = \frac{m_e c^2}{eB} \frac{\sqrt{\gamma_{\max}^2 - 1}}{h_z} < 1 . \quad (5.2)$$

In order to carry out the parameter study I have used 30 simulations in which the value of each of the shock, emission region, and jet parameters have been varied twice. The goal of this exercise is to understand the effects of varying various input parameters on the flux level and the spectral hardness of the low-energy component of the simulated SED, the simulated lightcurves for different photon energies, and the time step of the simulation. Table 5.1 shows the values of the base set (run 1) parameters used to obtain the first simulation and Table 5.2 shows the values of each of the parameters that have been varied in the rest of the simulations. The effect on the simulated SED, and lightcurves have been studied with respect to that from the base set.

Table 5.1. Parameter list used to obtain the first simulation from run 1.

Parameter	Symbol	Value
Wind Luminosity	$L_w$	$1 \times 10^{52}$ erg/s
Wind Duration	$t_w$	$2 \times 10^2$ s
Outer Shell Mass	$M_o$	$1 \times 10^{32}$ g
Inner Shell BLF	$\Gamma_i$	22
Outer Shell BLF	$\Gamma_o$	18
Inner Shell Width	$\Delta_i$	$1 \times 10^{14}$ cm
Outer Shell Width	$\Delta_o$	$5 \times 10^{14}$ cm
Electron Energy Equipartition Parameter	$\varepsilon_e$	$2 \times 10^{-3}$
Magnetic Energy Equipartition Parameter	$\varepsilon_B$	$4 \times 10^{-4}$
Fraction of Accelerated Electrons	$\zeta_e$	$1 \times 10^{-3}$
Acceleration Timescale Parameter	$\alpha$	$1 \times 10^{-3}$
Particle Injection Index	q	3.4
Zone/Jet Radius	$R_z$	$3 \times 10^{16}$ cm
Observer Frame Observing Angle	$\theta_{\text{obs}}$	2.4 deg
Redshift	z	0.536

Table 5.2. Parameter list for various simulations used for the parameter study.

Run #	Parameter Value
2*	$t_w = 3 \times 10^2$
3	$\Gamma_i = 20$
4	$\Gamma_i = 24$
5	$\Gamma_o = 16$
6	$\Gamma_o = 20$
9*	$M_o = 6 \times 10^{31}$
10	$L_w = 1 \times 10^{51}$
11	$L_w = 1 \times 10^{53}$
12	$\Delta_i = 1 \times 10^{15}$
13	$\Delta_i = 1 \times 10^{13}$
14	$\Delta_o = 5 \times 10^{15}$
15	$\Delta_o = 5 \times 10^{13}$
16	$\Delta_i \& \Delta_o = 5 \times 10^{14}$
17	$\Delta_i = 1 \times 10^{15} \& \Delta_o = 5 \times 10^{15}$
18	$\Delta_i = 1 \times 10^{13} \& \Delta_o = 5 \times 10^{13}$
19	$\varepsilon_e = 2 \times 10^{-2}$
20	$\varepsilon_e = 2 \times 10^{-4}$
21	$\varepsilon_B = 4 \times 10^{-3}$
22	$\varepsilon_B = 4 \times 10^{-5}$
23	$\zeta_e = 1 \times 10^{-2}$
24	$\zeta_e = 1 \times 10^{-4}$
25	$\alpha = 1 \times 10^{-2}$
26	$\alpha = 1 \times 10^{-4}$
27	$q = 2.4$
28	$q = 4.4$

Table 5.2 (continued)

Run #	Parameter Value
29	$R_z = 3 \times 10^{15}$
30	$R_z = 3 \times 10^{17}$
31	$\theta_{\text{obs}} = 1.4$
32	$\theta_{\text{obs}} = 4.4$

The starred numbers in the table stand for those simulations where the value of the parameter was not changed twice because in doing so more than one parameter's value had to be changed to obtain non-negative and physically meaningful values of the calculated quantities. For example, decreasing the value of  $t_w$  *only* resulted in a negative value for  $M_i$  because  $M_i = \frac{L_w t_w - (M_o \Gamma_o c^2)}{\Gamma_i c^2}$ . On the other hand, increasing the value of  $M_o$  *only* such that the second term is still less than the first one made  $M_i > M_o$  when it has been assumed that the inner shell is the faster moving one and thus should have a lower mass than the slower moving outer shell. Simulations 7 and 8 are not shown as a part of the analysis because they involved changing  $\Gamma_i$  and  $\Gamma_o$  together that had the same effect on the simulated SED as simulations 5 and 6 respectively. Table 5.3 delineates the effects of changing the values of the input parameters according to Table 5.2 on the flux, and spectral hardness.

Table 5.3. Parameter study of the shock, emission-region, and jet parameters.

Input parameters	Value	$\nu F_\nu$ [Jy Hz]	Spectral hardness
$L_w$	↑	↑	↑ $\alpha_{\text{spec}} = 0.82$
	↓	↓	↓ $\alpha_{\text{spec}} = 1.35$
$t_w$	↑	↑	↑ $\alpha_{\text{spec}} = 0.90$
$M_o$	↓	↑	↑ $\alpha_{\text{spec}} = 1.05$
$\Gamma_i$	↑	↑	↑ $\alpha_{\text{spec}} = 1.15$
	↓	↓	↓ $\alpha_{\text{spec}} = 1.83$
$\Gamma_o$	↑	↓	↓ $\alpha_{\text{spec}} = 1.37$
$\Gamma_o$	↓	↑	↑ $\alpha_{\text{spec}} = 1.14$
$\Delta_i$	↑	↓	↓ $\alpha_{\text{spec}} = 1.32$
	↓	↑	↑ $\alpha_{\text{spec}} = 1.03$
$\Delta_o$	↑	↓	↓ $\alpha_{\text{spec}} = 1.34$
	↓	↑	↑ $\alpha_{\text{spec}} = 0.79$
$\Delta_i \& \Delta_o$	=	↓	↑ $\alpha_{\text{spec}} = 1.23$
	↑	↓	↓ $\alpha_{\text{spec}} = 1.40$
	↓	↑	↑ $\alpha_{\text{spec}} = 0.94$
$\varepsilon_e$	↑	↑	↑ $\alpha_{\text{spec}} = 0.20$
	↓	↓	↓ $\alpha_{\text{spec}} = 1.27$
$\varepsilon_B$	↑	↑	↑ $\alpha_{\text{spec}} = 0.78$
	↓	↓	↓ $\alpha_{\text{spec}} = 1.30$
$\zeta_e$	↑	↑	↓ $\alpha_{\text{spec}} = 1.54$
	↓	↓	↑ $\alpha_{\text{spec}} = -0.05$
$\alpha$	↑	↑	-
	↓	↓	-
$q$	↑	↑	↓ $\alpha_{\text{spec}} = 1.45$
	↓	↓	↑ $\alpha_{\text{spec}} = 1.07$

Table 5.3 (continued)

Input parameters	Value	$\nu F_\nu$ [Jy Hz]	Spectral hardness
$R_z$	↑	↓	↓ $\alpha_{\text{spec}} = 1.30$
	↓	↑	↑ $\alpha_{\text{spec}} = 0.77$
$\theta_{\text{obs}}$	↑	↓	↓ $\alpha_{\text{spec}} = 1.68$
	↓	↑	↑ $\alpha_{\text{spec}} = 0.99$

Note. — The slope of the low-energy component of the SED obtained from run 1 in the optical range (R band;  $4.0 - 6.0 \times 10^{14}$  Hz) is  $\alpha_{\text{spec}} = 1.40$ . The slope for run 1 and rest of the simulations has been obtained at the maximum value of the R band flux. The ↑ implies increase in the value of a particular quantity, ↓ refers to the decrease in the value, and - stands for no change in the value.

Figures 5.1 - 5.7 show the effect of varying various input parameters on the time-averaged simulated spectra of a generic blazar source. For the sake of brevity, the resultant SEDs have been clubbed into four groups, wind parameters, shell parameters, emission-region parameters, and jet parameter.

As can be seen from Figure 5.1 and Table 5.3, increasing  $L_w$  (run 11) or  $t_w$  (run 2) increases the overall flux of the spectrum. This is because in both the cases the internal energy of the shocks, the magnetic field value, the  $\gamma_{\text{min}}$  value, and the density of injected electrons in the region increase. The photon number density, due to synchrotron and SSC scattering, in the region consequently increases along with the value of peak synchrotron frequency,  $\nu_{\text{syn}}^{\text{peak}}$  (location of the low-energy SED maxi-

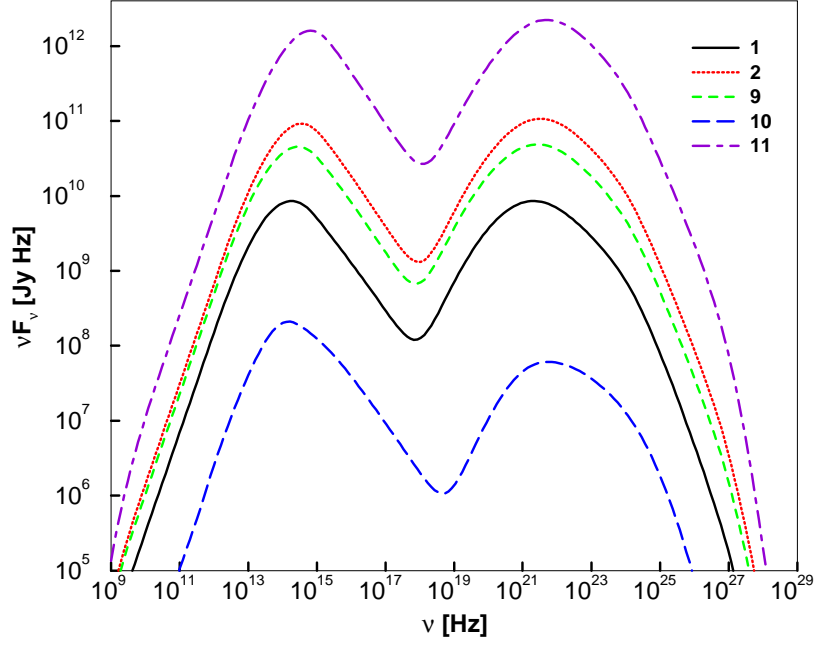


Figure 5.1: Simulated time-integrated SED of a generic source illustrating the effects of varying the wind parameters,  $L_w$  (runs 10 & 11),  $t_w$  (run 2), and  $M_o$  (run 9), according to Table 5.2.

num). Consequently, the electrons will lose more of their energy due to synchrotron and SSC processes and as a result will produce low-energy photons making the overall spectrum softer. The value of  $\alpha_{\text{spec}}$  in Table 5.3 shows otherwise. This is because the  $\alpha_{\text{spec}}$  has been calculated in the R-band frequency range at the time the flux peaks. If this range happens to lie in the turnover part of the low-energy component, the  $\alpha_{\text{spec}}$  will not pertain to the power-law part of the synchrotron spectrum and will have a lower value. This can also be verified from the fact that  $\nu_{\text{syn}}^{\text{peak}}$  for both runs is located in that part of the frequency range that contains the R-band. The ratio of SSC to

synchrotron flux also increases with increase in overall flux level of the SED because more electrons are able to upscatter the synchrotron photons thereby increasing the SSC flux level.

On the other hand, decreasing  $L_w$  (run 10) results in a spectrally harder spectrum with a lower flux. The effect of decreasing  $M_o$  (run 9) is similar to that of runs 11 (increasing  $L_w$ ) and 2 (increasing  $t_w$ ). The shocks' internal energies, magnetic field value, and the number of particles injected into the region increase. As a result, the electrons lose more of their energy producing a photon flux but a softer spectrum. Here also, the  $\alpha_{\text{spec}}$  value for run 9 (low  $M_o$ ) from Table 5.3 shows the opposite effect because of the same reason given earlier. Since the increase in the magnetic field value and the density of injected electrons is not as much as in the case of runs 2 ( $\uparrow t_w$ ) and 11 ( $\uparrow L_w$ ), the shift in  $\nu_{\text{syn}}^{\text{peak}}$  to higher frequencies and the ratio of SSC to synchrotron flux with respect to that of run 1 is not as prominent as in the previous two cases.

From Figure 5.2 and Table 5.3, it can be seen that the flux level of the simulated SED goes up for a higher value of  $\Gamma_i$  (run 4) and a lower value of  $\Gamma_o$  (run 5). This is because, in these cases the relative velocity of the two shells increases along with the value of the internal shock energies, magnetic field,  $\gamma_{\text{min}}$ , and the density of electrons injected into the region. This makes the acceleration much more efficient and thus increases the level of photon flux and makes the spectrum harder. Again, the value of  $\nu_{\text{syn}}^{\text{peak}}$  and the ratio of SSC to synchrotron flux relative to run 1 increases slightly.

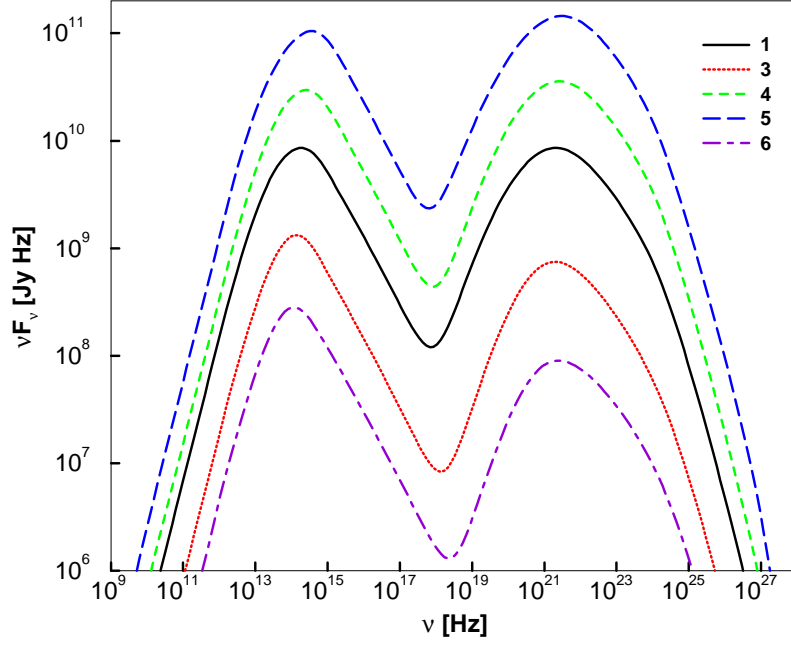


Figure 5.2: Simulated time-integrated SED of a generic source illustrating the effects of varying the 1st set of shell parameters,  $\Gamma_i$  (run 3 & 4), and  $\Gamma_o$  (run 5 & 6), according to Table 5.2.

On the other hand,  $\Gamma_i$  and  $\Gamma_o$  values from runs 3 and 6, respectively, result in a lower relative velocity of the two shells thereby decreasing the acceleration efficiency and making the SED lower in flux and spectrally softer. In case of run 6 ( $\uparrow \Gamma_i$ ), the value of  $\alpha_{\text{spec}}$  from Table 5.3 shows otherwise because of the same reason of R-band peak flux frequency range not falling in the part of the synchrotron spectrum that follows the power-law. Also, the value of  $\nu_{\text{syn}}^{\text{peak}}$  in both the cases shifts toward slightly lower frequencies and the ratio of SSC to synchrotron flux also decreases relative to that of run 1.

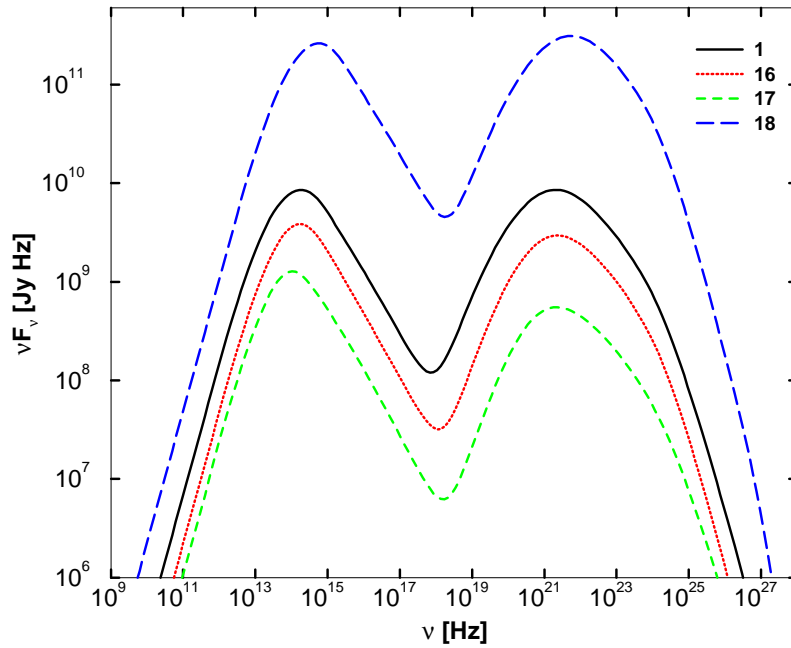


Figure 5.3: Simulated time-integrated SED of a generic source illustrating the effects of varying the 3rd set of shell parameters,  $\Delta_i$  and  $\Delta_o$  together (runs 16, 17 & 18), according to Table 5.2.

As shown in Figure 5.3, and Table 5.3, increasing the shell widths (run 17) decreases the magnetic field value and the density of injected electrons in the region. As a result the flux of the spectrum decreases along with the ratio of the SSC to synchrotron peak flux and the  $\nu_{\text{syn}}^{\text{peak}}$  also shifts toward slightly lower frequency relative to that of run 1. On the other hand, the spectral hardness increases because, as explained before, the energy loss time scale of the electrons increases and the spectrum is produced by a fairly energetic population of electrons. A counter argument can be applied to understand the behaviour of the spectrum and the spectral hardness

resulting from decreasing the shell widths (run 18). The  $\alpha_{\text{spec}}$  values from Table 5.3 for both runs shows otherwise because of the same reason stated earlier.

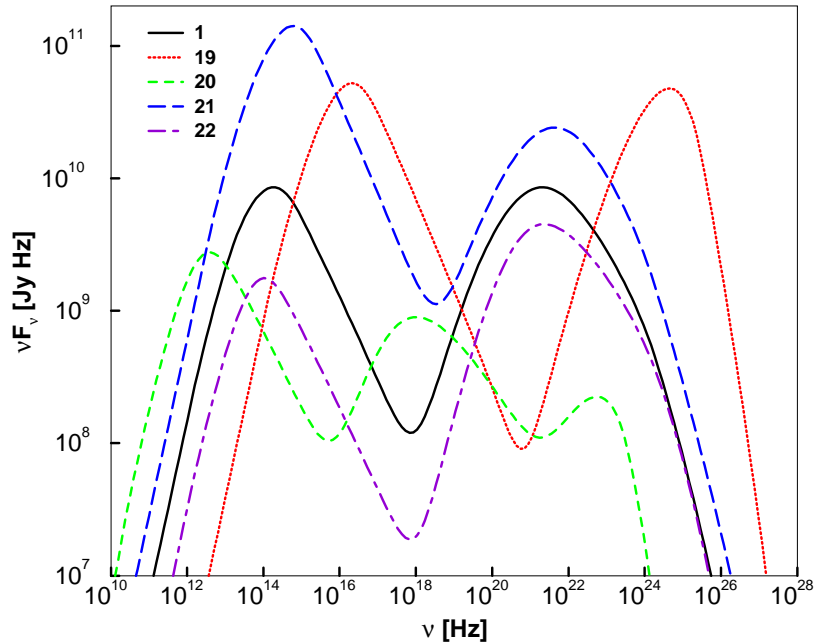


Figure 5.4: Simulated time-integrated SED of a generic source illustrating the effects of varying the 1st set of emission-region parameters,  $\varepsilon_e$  (runs 19 & 20), and  $\varepsilon_B$  (run 21 & 22), according to Table 5.2.

Increasing the value of  $\varepsilon_e$  (Fig. 5.4, run 19), increases the  $\gamma_{\text{min}}$  value of the injected electron distribution thereby shifting the resultant spectrum towards higher frequencies. The overall flux of the spectrum increases because the density of injected electrons in the region increases but this decreases the spectral hardness of the SED because the energy loss time scale due to SSC scattering decreases and the spectrum is produced by a less energetic population of electrons. The value of  $\alpha_{\text{spec}}$  again shows

the opposite effect because of the same reason stated earlier. The ratio of SSC to synchrotron flux remains the same because although the density of injected electrons increases the magnetic field value relative to that of run 1 does not change thereby keeping the two flux levels same.

On the other hand, decreasing  $\varepsilon_e$  (run 20) results in a lower value of  $\gamma_{\min}$  due to which the spectrum shifts leftwards and starts to show the presence of a higher order SSC component (3rd bump from the left) as well. This is because for such low energies of electrons, the Klein-Nishina (KN) effects no longer suppress the higher-order SSC component. The overall flux of the spectrum decreases and the spectral hardness increases because of less electrons being injected into the region. Increasing  $\varepsilon_B$  (run 21) increases the magnetic field, which decreases the synchrotron cooling time scale. Thus, the resultant spectrum comes from a cooled population of electrons and is hence, spectrally softer. The value of  $\alpha_{\text{spec}}$  from Table 5.3 again does not show the same effect because of the reason given before. Since the same number of electrons as that of run 1 is injected into the region with a higher magnetic field value, the electrons lose their energy primarily due to synchrotron losses. This increases the number of synchrotron photons along with the  $\nu_{\text{syn}}^{\text{peak}}$  value but decreases the photon flux due to SSC scattering. As a result, the flux of the overall spectrum increases but the SSC to synchrotron flux ratio decreases. The opposite reason can be applied to understand the effect of decreasing  $\varepsilon_B$  (run 22).

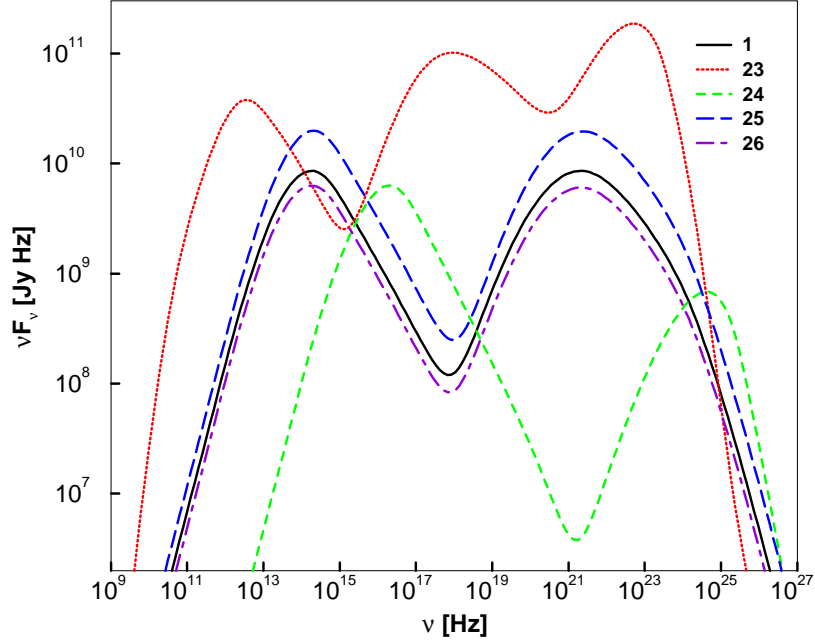


Figure 5.5: Simulated time-integrated SED of a generic source illustrating the effects of varying the 2nd set of emission-region parameters,  $\zeta_e$  (runs 23 & 24), and  $\alpha$  (runs 25 & 26), according to Table 5.2.

As shown in Figure 5.5 and Table 5.3, increasing  $\zeta_e$  (run 23) increases the fraction of accelerated electrons in the region thereby increasing the overall flux of the spectrum. At the same time, it also decreases  $\gamma_{\min}$  as a result of which the higher order SSC component becomes prominent in the spectrum as explained earlier; the Thomson depth of the region increases as well, facilitating higher order SSC scatterings. This brings down the synchrotron flux level and shifts the spectrum to lower frequencies. The overall flux of the spectrum rises since the fraction of accelerated electrons in the region is higher but here the spectrum becomes harder because the

number density of accelerated electrons injected into the region reduces. The reason the value of  $\alpha_{\text{spec}}$  does not reflect that same idea is because, as can be seen from the figure, the R-band peak flux frequency range lies in the lower part of the synchrotron spectrum that is close to the transition between synchrotron and SSC component. Thus the  $\alpha_{\text{spec}}$  does not come from a power-law distribution of the spectrum and gets a higher value.

On the other hand, a decreased value of  $\zeta_e$  (run 24) has the opposite effect on the SED and the spectral hardness of the spectrum. Here again the value of  $\alpha_{\text{spec}}$  is not reflective of the true nature of the spectrum because the R-band peak flux frequency range now lies in the rising part of the synchrtron spectrum making  $\alpha_{\text{spec}}$  negative in value. The variation of  $\alpha$  (runs 25 & 26) does not have much affect on the spectral hardness of the spectrum although the SED resulting from a higher value of  $\alpha$  has a slightly higher flux. This can be understood from the fact that since  $\alpha$  is the acceleration timescale parameter (the number of gyration cycles per acceleration time scale), it does not play an important role in the overall evolution of the SED and its spectral hardness except changing the value of  $\gamma_{\text{max}} \propto \alpha^{1/2}$  (Chapter 4, equation 4.19).

Increasing the value of  $q$  (run 28) increases the value of  $\gamma_{\text{min}}$  slightly, and the density of injected electrons keeping the magnetic field value the same. Thus the overall flux level of the SED rises slightly with a marginal increase in the ratio of SSC to synchrotron peak flux and the  $\nu_{\text{syn}}^{\text{peak}}$  value. The spectrum becomes softer as

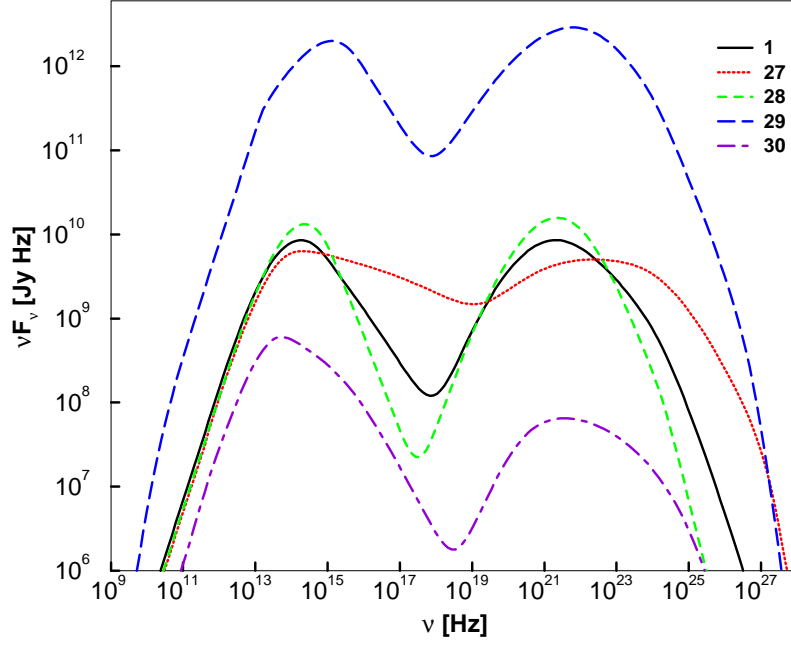


Figure 5.6: Simulated time-integrated SED of a generic source illustrating the effects of varying the 3rd set of emission-region parameters,  $q$  (runs 27 & 28), and  $R_z$  (runs 29 & 30), according to Table 5.2.

depicted by the value of  $\alpha_{\text{spec}}$  from Table 5.3. Decreasing  $q$  (run 27) decreases  $\gamma_{\text{min}}$  and the density of injected electrons, slightly. As a result, the overall flux of the SED decreases but the spectrum becomes flatter (harder) as can be seen in Figure 5.6 and Table 5.3. Increasing  $R_z$  (run 30) decreases the overall flux of the SED because in this case, the same density of electrons is now being injected into a larger region with a lower magnetic field. This also decreases the ratio of SSC to synchrotron peak flux and the  $\nu_{\text{syn}}^{\text{peak}}$  value and makes the spectrum harder. The opposite is true for a lower

value of  $R_z$  (run 29). Here again, the same is not true for the value of  $\alpha_{\text{spec}}$  because of the same explanation given before.

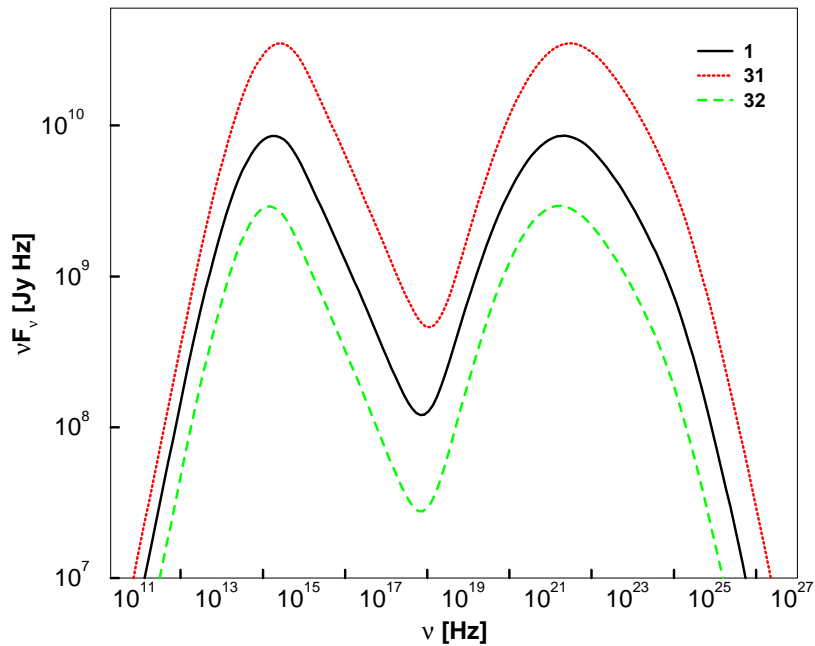


Figure 5.7: Simulated time-integrated SED of a generic source illustrating the effects of varying the jet parameters,  $\theta_{\text{obs}}$  (runs 31 & 32), according to Table 5.2.

As can be seen from Figure 5.7 and Table 5.3, decreasing the value of  $\theta_{\text{obs}}$  (run 31) increases the overall flux of the spectrum. This is because in this case, the jet is closely aligned with our line of sight as a result of which the overall radiation is boosted more strongly in our direction and makes the spectrum look spectrally harder. The opposite is true for the case where the jet is oriented at a larger angle with respect to our line of sight (run 32).

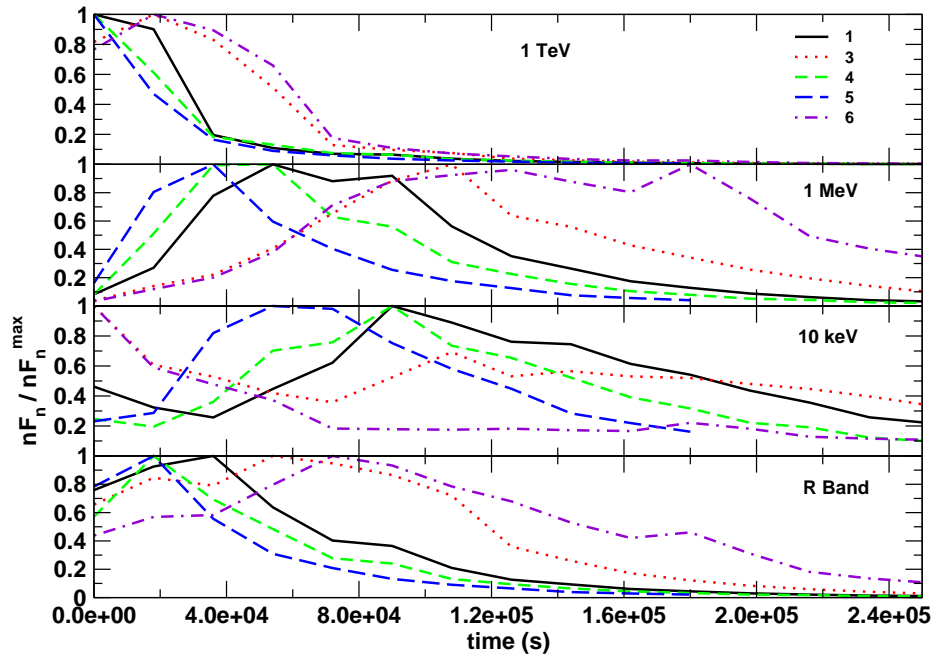


Figure 5.8: Example of simulated lightcurves in various energy bands (R, 10 keV, 1 MeV, and 1 TeV) of a generic blazar source resulting from varying the 1st set of shell parameters,  $\Gamma_i$  (runs 3 & 4) and  $\Gamma_o$  (runs 5 & 6).

Figures 5.8 - 5.10 illustrate the effects of varying various input parameters on the resulting lightcurves of a generic blazar source.

Figure 5.8 shows some sample lightcurves for the energy bands in the optical (R), X-ray (10 keV), high-energy (1 MeV), and VHE regime (1 TeV) resulting from runs 3 ( $\downarrow \Gamma_i$ ), 4 ( $\uparrow \Gamma_i$ ), 5 ( $\downarrow \Gamma_o$ ), and 6 ( $\uparrow \Gamma_o$ ). The flux value for every energy band in all the graphs has been normalized with respect to the maximum flux value of that energy band.

As can be seen from Figure 5.9, the lightcurve from run 17 is much more extended than the lightcurves of run 1 and 18. This is because run 17 corresponds to larger widths of the colliding shells and thus a wider resulting emission region. As a result,

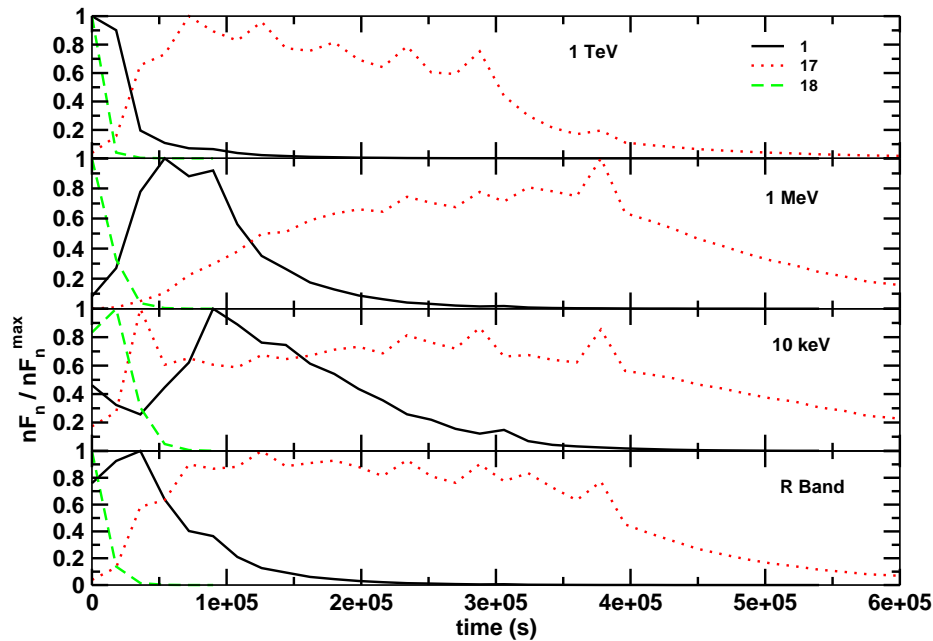


Figure 5.9: Simulated lightcurves of a generic blazar source in the R band, 10 keV, 1 MeV, and 1 TeV energy regimes illustrating the effects of varying shell widths (runs 17 & 18).

the time taken for the shocks to propagate through the region is extended and the acceleration continues for a longer time making the width of the pulse wider in all the energy bands. The opposite is true for the lightcurves of run 18.

The lightcurves from run 27 (minimum  $q$  value) (Figure 5.10) show that a harder energy distribution of the electron population in the region results in a sharper rise and a steeper decline of the acceleration pulse. Since the parent population of electrons is more energetic than that of runs 1 (base set) & 28 (maximum  $q$  value), the electrons lose their energy faster and more energetic synchrotron photons (X-ray and MeV; Figure 5.6) are produced first in comparison to the lower energy ones (optical). As a result, the rise in the pulse is sooner in the case of lightcurves of higher energy bands

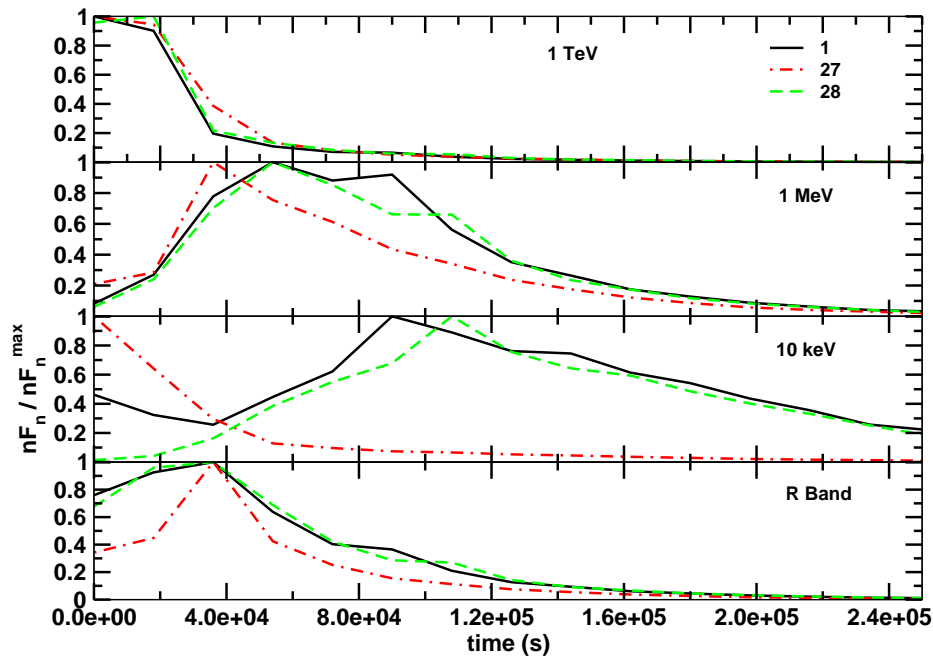


Figure 5.10: Simulated lightcurves in the R band, 10 keV, 1 MeV, and 1 TeV energy regimes of a generic source illustrating the effects of varying  $q$  (runs 27 & 28).

(10 keV, and 1 MeV) resulting from run 27 as compared to those of runs 1 & 28. On the other hand, optical photons in run 27 are produced from a cooled population of electrons and thus are produced at about the same time as that for runs 1 and 28. The VHE photons (1 TeV) result from the SSC scattering of lower energy (optical) synchrotron photons and hence are produced at the same time for all runs. Since the VHE photons are produced only during the acceleration phase of the emission region, the sharp drop in the 1 TeV energy regime is indicative of the time (in the observer's frame) the shocks completely break out of the system.

## 5.2 Acceleration Scenarios

Relativistic shocks can propagate through a jet such that the background magnetic field is parallel to the shock normal (parallel shocks) or is inclined with respect to the shock normal (oblique shocks). Both types of shocks can accelerate particles through 1st and 2nd order Fermi acceleration mechanisms.

In the case of 1st order Fermi acceleration mechanism, an electron crossing the shock front (from upstream to downstream) is reflected back through the shock (downstream to upstream) if it encounters any moving local magnetic inhomogeneity in the downstream region. In doing so, the electron gains energy. If the same process occurs upstream and the particle is reflected downstream, the particle again gains energy. These multiple reflections greatly increase the energy of the electron. The energy gain per shock crossing is linearly proportional to the shock velocity and that is why this mechanism is called the 1st order Fermi acceleration (Longair 1994). On the other hand, in the case of 2nd order Fermi acceleration the electron gains energy upon reflection from a moving magnetic mirror such that the energy gained is proportional to the square of the velocity of the mirror.

According to the current understanding of acceleration mechanisms, relativistic parallel shocks generally produce electron spectra that follow a power-law distribution with an injection index of  $q \sim 2.2 - 2.3$  (Achterberg et al. 2001; Gallant et al. 1999). Oblique shocks produce much softer injection spectral indices with  $q > 2.3$  (Ostrowski and Bednarz 2002; Niemiec and Ostrowski 2004). On the other hand, 2nd order Fermi

acceleration behind the shock front might give rise to a harder injection index of the order of  $q \sim 1$  or beyond. Thus, the value of  $q$  used for simulating the SED and spectral lightcurves of a blazar source can shed light on the type of shock propagating through the jet and the mode of acceleration mechanism dominant in the source.

### 5.3 Summary

The code has been tested to satisfy various analytical conditions. An extensive parameter study of the code has been carried out to understand the effects of varying various wind parameters (wind luminosity, wind duration and mass of the outer shell), shell parameters (BLF and width of the two shells), emission-region parameters (fraction of shock energy in the electron and magnetic field energy density, fraction of effectively accelerated electrons, acceleration timescale parameter, particle injection index, and radius of the zone/jet), and jet parameter (observing angle), on the resulting SED and spectral lightcurves. The goal of this exercise was to aid in future simulations of the observed features of various blazar sources. The value of the particle injection index that results in the successful reproduction of the observed features of a source can be used as an indicator of the type of shock propagation and mode of dominant acceleration prevalent in the blazar.

## CHAPTER 6

# Summary and Conclusions

### 6.1 Blazar Observations and Modeling

The main objective of this work was to understand the physics of radiation and particle acceleration in the jets of blazars. The idea was to be able to reproduce the observed spectral features, such as spectral energy distribution (SED), spectral variability and hysteresis patterns, lightcurves, and, if present, cross-correlations between different energy bands. The simulations of such spectral features provide an insight into the interplay between various radiation mechanisms responsible for producing the observed spectrum and give us hints about the dominant mode of particle acceleration in the jet of the simulated blazar.

Multiwavelength and simultaneous observations of blazars are extremely relevant for such types of modelling efforts. A recent campaign to obtain such multiwavelength data in order to understand the physical processes of 3C 66A was carried out for the low-frequency peaked BL Lac object 3C 66A in the year 2003 - 2004. I got started on this project by combining disparate data sets from different optical observatories and placing them on a common photometric scale besides de-reddening the optical data. I used the resulting multiwavelength data to estimate key physical properties

of the source, such as the size of the emission region, and strength of the comoving magnetic field, by employing fundamental physical arguments.

I have carried out an extensive analysis of the data of 3C 66A obtained from the multiwavelength monitoring campaign of the object from July 2003 to April 2004. In order to carry out the theoretical analysis of the object, I used the time-dependent radiation transfer code of [Böttcher and Chiang \(2002\)](#) to develop a model that successfully reproduced the observed SED across the entire electromagnetic spectrum and the optical variability pattern ([Joshi and Böttcher 2007](#)). The successful model resulted in predictions concerning potentially observable X-ray spectral variability and  $\gamma$ -ray emission and predicted that the object is within the sensitivity limits of MAGIC, VERITAS (if the external component (EC) component is dominant) and Fermi.

- The prediction regarding VERITAS recently came true when 3C 66A was detected in an active state by the telescope emitting  $> 100$  GeV  $\gamma$ -ray photons ([Swordy 2008](#)).

Observations with such facilities provide an important means to verify predictions regarding an object and improve a model's physical constraints at such high energies.

Besides carrying out the theoretical analysis of the data of 3C 66A, obtained from the multiwavelength campaign organized in 2003/2004, I have also conducted observations with the 1.3 m McGraw-Hill telescope of the MDM observatory at Kitt Peak primarily to collect more optical data on 3C 66A. In addition, I have observed several

other blazars of interest and contributed to blazar monitoring campaigns (Böttcher et al. 2007, e.g.,). I have also collected data to follow up on several gamma-ray burst (GRB) alerts (Yost et al. 2006; Böttcher and Joshi 2005; Mirabal et al. 2005) during some of these runs. The data collection for blazars was carried out by observing them in the U, B, V, R and I bands. I have been to 6 of such one-week observing runs and have reduced part of the data collected from these runs using IRAF. The reduction included the standard image reduction and photometry in order to obtain the calibrated fluxes of blazars and plot their respective lightcurves. This is a part of an ongoing project, aimed at monitoring the optical spectral variability of a sample of  $\gamma$ -ray loud blazars on various time scales in order to put stronger constraints on the mode of particle acceleration in the jets of these blazars and carry out follow-up observations of the afterglows of GRBs, should the occasion arise.

## 6.2 Internal Shock Model

I have used the internal shock model to understand the various modes of accelerating particles to relativistic energies and the geometrical structure of the acceleration region, at sub-parsec scales, inside a relativistic jet. This aspect is crucial to the development of a code that is capable of explaining the acceleration as well as the radiation mechanisms of high energy particles in the jets of blazars.

In this scenario, two shells of plasma of disparate mass, velocity, and energy content, were made to collide inelastically to result in two internal shocks, namely

the FS and the RS, both moving relativistically and separated by a CD. As the two shocks travelled through the shocked (emission) region, the electrons and positrons in the region were accelerated and started to continuously lose their energy via various radiative processes. I obtained the characteristics of the shock dynamics by solving the hydrodynamic Rankine-Hugoniot jump conditions across the shock fronts for a relativistic case (Spada et al. 2001). The resultant shock parameters were used to obtain the parameters for the FS and the RS emission region in the comoving frame of the shocked fluids. The emission region parameters were then used to calculate the radiation spectrum resulting from each emission region.

I have developed a zone+feedback scheme to properly calculate the resultant spectrum from the single inelastic collision and address the issue of the geometrical structure of the accelerating region and the non-locality and time-delayedness of the SSC emission of a blazar source. Under this scheme, I consider a cylindrical emission region that is divided into multiple zones. The reason for dividing the single emission region into multiple zones is to be able to incorporate the inhomogeneity in the photon and particle density throughout the emission region and make it trackable throughout the region numerically. I then consider the subsequent time-dependent radiation transfer within each zone and in between zones by including in the code the appropriate photon escape probability functions of a cylindrical region.

- I have calculated these functions analytically, and to the best of my knowledge such a calculation has been carried out for the first time. These functions will

be extremely useful to the blazar community and others carrying out a similar work.

I have also included in the code the time-delay effect for a cylindrical region resulting from the finiteness of the photon velocity.

### **6.3 Modeling Results and Acceleration Scenarios**

The acceleration+radiation mechanism (ARM) code has been tested to satisfy various analytical conditions. I have carried out an extensive parameter study of the code to understand the effects of varying shock and radiation parameters, such as the injection wind luminosity, colliding shell masses, shell widths, fraction of accelerated electrons, equipartition between electron energy density, magnetic energy density and shock internal energy density, particle spectral index, and radius of the emission region, on the resulting flux level and spectral hardness of the simulated SED as well as on the time-step of the simulation. Such a study is extremely useful in the reproduction of the observed SED, spectral variability patterns, and spectral lightcurves of blazars and in obtaining the results computationally faster. The ARM code is currently being used to simulate the SED and spectral lightcurves of the radio-loud quasar 3C 279 to gain insight into the dominant mode of acceleration responsible for accelerating particles to highly relativistic energies inside its jet and at the same time

get a clear picture of the interplay between various radiative processes responsible for producing its observed spectrum.

## 6.4 Future Direction

The ultimate goal of this work is to be able to use the ARM code to reproduce the observed SEDs and spectral variability patterns of many more blazars, especially those of the potential future TeV sources, with the aim of constraining the dominant acceleration mechanism in such objects and also make the code available for public use. The one main piece that needs to be incorporated into the code to complete my study of acceleration and radiation mechanisms in the jets of blazars is the EC component to understand its effect on the evolution of the electron energy distribution and hence, on the resulting radiation spectrum of a source.

The external Comptonization is the Compton upscattering of photons, external to the relativistic jet, by the electrons inside the jet. The seed photons for the EC process include the UV and soft X-ray emission from the disk entering the jet either directly ([Dermer et al. 1992](#); [Dermer and Schlickeiser 1993](#)) or after being reprocessed in the BLR or other circumnuclear material ([Sikora et al. 1994](#); [Dermer et al. 1997](#); [Böttcher and Bloom 2000](#)).

- Inclusion of the EC component is extremely important to correctly assess the interplay between the SSC and the EC component in producing the high-energy

component of the SED, which makes it possible to gauge the physical environment inside and outside the jet of a particular blazar source. This knowledge can be used to better understand the differences between the three sub-classes of blazars, namely FSRQs, LBLs, and HBLs.

The current approach of invoking a single inelastic collision in the ARM code can be extended to include multiple collisions in the jet and study their effects on the resulting spectrum. This kind of a study would prove to be a useful tool in looking for observational signatures of the presence of multiple shell collisions in a jet and in deciding whether single or multiple collisions are required to explain the observed variability patterns of a blazar source. If any smaller flaring episodes are observed during a major outburst, or in other words, if a major outburst is composed of many minor outbursts, then that might be a direct indication of multiple shell collisions taking place inside a jet. The ARM code can also be modified to understand the physics of radiation and acceleration in other similar astrophysical jets such as those found in GRBs, X-ray binaries.

One aspect of particle acceleration that is yet to be explored for astrophysical jets is shear acceleration at sub-parsec scales of the jet. The acceleration of particles and the origin of emission in astrophysical jets has been largely treated under the assumption of a one-dimensional flow profile. This approach, although quite useful, is adequate only to a first approximation because real jets are naturally expected to show a significant velocity shear across the jet. The jet's radial stratification has been

used to interpret some of the radio and optical observations of extragalactic jets, such as those of the radio galaxies M87, 3C 31, and 3C 296 (Stawarz and Ostrowski 2002) (and references therein). Energetic particles can be accelerated by this velocity shear in the relativistic background flow of the jet. In this case, the particles are accelerated to very high energies when they encounter different local flow velocities while being elastically scattered off small-scale magnetic field inhomogeneities that are embedded in the collisionless, and systematically moving background flow of the jet (Rieger and Duffy 2004). This is because the particle momentum relative to the flow changes for every travel across the shear, which increases its net momentum.

There are three possible ways of accelerating a particle travelling across a shear flow. A gradual velocity shear parallel to the jet axis, in which the particle experiences a gradual shear as the velocity of the flow changes continuously along the radial direction, such as a velocity profile decreasing linearly outward with radial coordinates. Another possibility is to have a nongradual and/or discontinuous longitudinal velocity shear in the flow. The third possibility is to have a gradual velocity shear that is perpendicular to the jet axis. This case corresponds to an intrinsic jet rotation (Rieger and Duffy 2004). In case of AGNs, the intrinsic jet rotation has been suggested by several indirect observations, such as the helical motion of knots, the detection of a double helical pattern, and observations of periodic variabilities (Rieger and Duffy 2004) (and references therein).

- The jet radial stratification is currently being understood for large-scale jet structures (parsec and kilo-parsec jet scales). Attempts need to be made to understand the effects of shear acceleration at sub-parsec scales of relativistic jets in order to obtain a complete picture of particle acceleration at all length scales of relativistic jets.

# Bibliography

- M. Abramowitz and I. A. Stegun. *Handbook of mathematical functions : with formulas, graphs, and mathematical tables*. Washington, D.C. : U.S. Dept. of Commerce, National Bureau of Standards ; For sale by the Supt. of Docs., U.S. G.P.O., 1970.
- A. Achterberg, Y. A. Gallant, J. G. Kirk, and A. W. Guthmann. Particle acceleration by ultrarelativistic shocks: theory and simulations. *MNRAS*, 328:393–408, December 2001.
- F. Aharonian, A. G. Akhperjanian, A. R. Bazer-Bachi, B. Behera, M. Beilicke, W. Benbow, D. Berge, K. Bernlöhr, C. Boisson, and O. Bolz, et al. An Exceptional Very High Energy Gamma-Ray Flare of PKS 2155-304. *ApJ*, 664:L71–L74, August 2007.
- C. W. Akerlof, F. A. Aharonian, K. Alatalo, M. C. Ashley, , S. D. Barthelmy, C. H. Blake, J. S. Bloom, M. Böttcher, D. N. Burrows, and E. E. Falco, et al. Optical Observations Of Gamma-Ray Bursts With ROTSE-III. In *Bulletin of the American Astronomical Society*, volume 38 of *Bulletin of the American Astronomical Society*, pages 134–+, June 2006.
- J. Albert, E. Aliu, H. Anderhub, P. Antoranz, A. Armada, C. Baixeras, J. A. Barrio, H. Bartko, D. Bastieri, and J. K. Becker, et al. Variable Very High Energy  $\gamma$ -Ray Emission from Markarian 501. *ApJ*, 669:862–883, November 2007.

- S. D. Bloom and A. P. Marscher. An Analysis of the Synchrotron Self-Compton Model for the Multi-Wave Band Spectra of Blazars. *ApJ*, 461:657–663, April 1996.
- M. Böttcher. Modeling the emission processes in blazars. *Ap&SS*, 309:95–104, June 2007.
- M. Böttcher, S. Basu, M. Joshi, M. Villata, A. Arai, N. Aryan, I. M. Asfandiyarov, U. Bach, R. Bachev, and A. Berduygin, et al. The WEBT Campaign on the Blazar 3C 279 in 2006. *ApJ*, 670:968–977, December 2007.
- M. Böttcher and S. D. Bloom. Analyzing the Multiwavelength Spectrum of BL Lacertae during the 1997 July Outburst. *AJ*, 119:469–477, February 2000.
- M. Böttcher and J. Chiang. X-Ray Spectral Variability Signatures of Flares in BL Lacertae Objects. *ApJ*, 581:127–142, December 2002.
- M. Böttcher, J. Harvey, M. Joshi, M. Villata, C. M. Raiteri, D. Bramel, R. Mukherjee, T. Savolainen, W. Cui, and G. Fossati, et al. Coordinated Multiwavelength Observation of 3C 66A during the WEBT Campaign of 2003-2004. *ApJ*, 631:169–186, September 2005.
- M. Böttcher and M. Joshi. GRB 051221A: MDM optical observations. *GRB Coordinates Network*, 4392:1–+, 2005.
- M. Böttcher, A. P. Marscher, M. Ravasio, M. Villata, C. M. Raiteri, H. D. Aller, M. F. Aller, H. Teräsanta, O. Mang, and G. Tagliaferri, et al. Coordinated Mul-

- tiwavelength Observations of BL Lacertae in 2000. *ApJ*, 596:847–859, October 2003.
- M. Böttcher, H. Mause, and R. Schlickeiser.  $\gamma$ -ray emission and spectral evolution of pair plasmas in AGN jets. I. General theory and a prediction for the GeV - TeV emission from ultrarelativistic jets. *A&A*, 324:395–409, August 1997.
- M. Böttcher and R. Schlickeiser. The pair production spectrum from photon-photon annihilation. *A&A*, 325:866–870, September 1997.
- D. A. Bramel, J. Carson, C. E. Covault, P. Fortin, D. M. Gingrich, D. S. Hanna, A. Jarvis, J. Kildea, T. Lindner, and R. Mukherjee, et al. Observations of the BL Lacertae Object 3C 66A with STACEE. *ApJ*, 629:108–114, August 2005.
- M. T. Carini and H. R. Miller. The Detection of Microvariability in the Blazar 3C 66A. In *Bulletin of the American Astronomical Society*, volume 23 of *Bulletin of the American Astronomical Society*, pages 1420–+, September 1991.
- B. W. Carroll and D. A. Ostlie. *An Introduction to Modern Astrophysics*. Institute for Mathematics and Its Applications, 1996.
- M. Catanese and T. C. Weekes. Very High Energy Gamma-Ray Astronomy. *PASP*, 111:1193–1222, October 1999.
- M. Chiaberge and G. Ghisellini. Rapid variability in the synchrotron self-Compton model for blazars. *MNRAS*, 306:551–560, July 1999.

- J. Chiang and C. D. Dermer. Synchrotron and Synchrotron Self-Compton Emission and the Blast-Wave Model of Gamma-Ray Bursts. *ApJ*, 512:699–710, February 1999.
- S. Ciprini, C. M. Raiteri, N. Rizzi, I. Agudo, L. Foschini, M. Fiorucci, L. O. Takalo, M. Villata, L. Ostorero, and A. Sillanpää, et al. Prominent activity of the blazar OJ 287 in 2005. XMM-Newton and multiwavelength observations. *Memorie della Societa Astronomica Italiana*, 78:741–+, 2007.
- L. Costamante and G. Ghisellini. TeV candidate BL Lac objects. *A&A*, 384:56–71, March 2002.
- J. H. Croston, M. J. Hardcastle, M. Birkinshaw, and D. M. Worrall. XMM-Newton observations of the hot-gas atmospheres of 3C 66B and 3C 449. *MNRAS*, 346:1041–1054, December 2003.
- A. Crusius and R. Schlickeiser. Synchrotron radiation in random magnetic fields. *A&A*, 164:L16–L18, August 1986.
- J. A. de Diego, M. R. Kidger, J. N. Gonzales-Perez, and H. J. Lehto. Rapid infrared spectral variability of 3C 66A in outburst. *A&A*, 318:331–336, February 1997.
- O. C. de Jager and A. K. Harding. The expected high-energy to ultra-high-energy gamma-ray spectrum of the Crab Nebula. *ApJ*, 396:161–172, September 1992.

- O. C. de Jager and F. W. Stecker. Extragalactic Gamma-Ray Absorption and the Intrinsic Spectrum of Markarian 501 during the 1997 Flare. *ApJ*, 566:738–743, February 2002.
- C. D. Dermer and R. Schlickeiser. Model for the High-Energy Emission from Blazars. *ApJ*, 416:458–, October 1993.
- C. D. Dermer, R. Schlickeiser, and A. Mastichiadis. High-energy gamma radiation from extragalactic radio sources. *A&A*, 256:L27–L30, March 1992.
- C. D. Dermer, S. J. Sturmer, and R. Schlickeiser. Nonthermal Compton and Synchrotron Processes in the Jets of Active Galactic Nuclei. *ApJS*, 109:103–137, March 1997.
- M. A. Dopita and R. S. Sutherland. *Astrophysics of the diffuse universe*. Berlin, New York: Springer, 2003. Astronomy and astrophysics library, 2003.
- J. D. Finke, J. C. Shields, M. Böttcher, and S. Basu. Redshift limits of BL Lacertae objects from optical spectroscopy. *A&A*, 477:513–516, January 2008.
- G. Fossati, L. Maraschi, A. Celotti, A. Comastri, and G. Ghisellini. A unifying view of the spectral energy distributions of blazars. *MNRAS*, 299:433–448, September 1998.
- J. A. Gaidos, C. W. Akerlof, S. D. Biller, P. J. Boyle, A. C. Breslin, J. H. Buckley, D. A. Carter-Lewis, M. Catanese, M. F. Cawley, and D. J. Fegan, et al. Very

- Rapid and Energetic Bursts of TeV Photons from the Active Galaxy Markarian 421. *Nature*, 383:319–320, 1996.
- Y. A. Gallant, A. Achterberg, and J. G. Kirk. Particle acceleration at ultra-relativistic shocks. Gamma-ray burst afterglow spectra and UHECRs. *A&AS*, 138:549–550, September 1999.
- M. Georganopoulos and A. P. Marscher. A Viewing Angle-Kinetic Luminosity Unification Scheme for BL Lacertae Objects. *ApJ*, 506:621–636, October 1998.
- I. S. Gradshteyn and I. M. Ryzhik. *Table of integrals, series and products*. New York: Academic Press, 5th ed., edited by Jeffrey, Alan, 1994.
- P. B. Graff, M. Georganopoulos, E. S. Perlman, and D. Kazanas. A multi-zone model for simulating the high energy variability of TeV blazars. *ArXiv e-prints*, 808, August 2008.
- R. C. Hartman, D. L. Bertsch, S. D. Bloom, A. W. Chen, P. Deines-Jones, J. A. Esposito, C. E. Fichtel, D. P. Friedlander, S. D. Hunter, and L. M. McDonald. The Third EGRET Catalog of High-Energy Gamma-Ray Sources. *ApJS*, 123:79–202, July 1999.
- R. C. Hartman, M. Böttcher, G. Aldering, H. Aller, M. Aller, D. E. Backman, T. J. Balonek, D. L. Bertsch, S. D. Bloom, and H. Bock, et al. Multiepoch Multiwavelength Spectra and Models for Blazar 3C 279. *ApJ*, 553:683–694, June 2001.

- F. C. Jones. Calculated Spectrum of Inverse-Compton-Scattered Photons. *Physical Review*, 167:1159–1169, March 1968.
- S. G. Jorstad, A. P. Marscher, M. L. Lister, A. M. Stirling, T. V. Cawthorne, W. K. Gear, J. L. Gómez, J. A. Stevens, P. S. Smith, J. R. Forster, and E. I. Robson, et al. Polarimetric Observations of 15 Active Galactic Nuclei at High Frequencies: Jet Kinematics from Bimonthly Monitoring with the Very Long Baseline Array. *AJ*, 130:1418–1465, October 2005.
- M. Joshi and M. Böttcher. Modeling the Spectral Energy Distribution and Variability of 3C 66A during the WEBT Campaign of 2003-2004. *ApJ*, 662:884–891, June 2007.
- J. Kataoka, T. Takahashi, F. Makino, S. Inoue, G. M. Madejski, M. Tashiro, C. M. Urry, and H. Kubo, et al. Variability Pattern and the Spectral Evolution of the BL Lacertae Object PKS 2155-304. *ApJ*, 528:243–253, January 2000.
- J. G. Kirk, F. M. Rieger, and A. Mastichiadis. Particle acceleration and synchrotron emission in blazar jets. *A&A*, 333:452–458, May 1998.
- S. Kobayashi, T. Piran, and R. Sari. Can Internal Shocks Produce the Variability in Gamma-Ray Bursts? *ApJ*, 490:92–98, November 1997.
- M. Kusunose, F. Takahara, and H. Li. Electron Acceleration and Time Variability of High-Energy Emission from Blazars. *ApJ*, 536:299–307, June 2000.

- S. Kwok. *Physics and Chemistry of the Interstellar Medium*. University Science Books, 2006., 2006.
- H. Li and M. Kusunose. Temporal and Spectral Variabilities of High-Energy Emission from Blazars Using Synchrotron Self-Compton Models. *ApJ*, 536:729–741, June 2000.
- T. Lindner. *STACEE observations of BL Lac objects*. PhD thesis, McGill University (Canada), 2007.
- M. S. Longair. *High energy astrophysics. Vol.2: Stars, the galaxy and the interstellar medium*. Cambridge: Cambridge University Press, 1994.
- A. P. Marscher and W. K. Gear. Models for high-frequency radio outbursts in extragalactic sources, with application to the early 1983 millimeter-to-infrared flare of 3C 273. *ApJ*, 298:114–127, November 1985.
- P. Mimica, M. A. Aloy, E. Müller, and W. Brinkmann. Synthetic X-ray light curves of BL Lacs from relativistic hydrodynamic simulations. *A&A*, 418:947–958, May 2004.
- N. Mirabal, M. Böttcher, J. Shields, M. Joshi, and J. P. Halpern. GRB 050502a: optical observations. *GRB Coordinates Network*, 3363:1–+, 2005.
- A. Mücke and R. J. Protheroe. A proton synchrotron blazar model for flaring in Markarian 501. *Astroparticle Physics*, 15:121–136, March 2001.

- A. Mücke, R. J. Protheroe, R. Engel, J. P. Rachen, and T. Stanev. BL Lac objects in the synchrotron proton blazar model. *Astroparticle Physics*, 18:593–613, March 2003.
- J. Niemiec and M. Ostrowski. Cosmic-Ray Acceleration at Relativistic Shock Waves with a “Realistic” Magnetic Field Structure. *ApJ*, 610:851–867, August 2004.
- M. Ostrowski and J. Bednarz. Comment on the first-order Fermi acceleration at ultra-relativistic shocks. *A&A*, 394:1141–1144, November 2002.
- P. Padovani. The blazar sequence: validity and predictions. *Ap&SS*, 309:63–71, June 2007.
- M. Perri, E. Massaro, P. Giommi, M. Capalbi, R. Nesci, G. Tagliaferri, G. Ghisellini, M. Ravasio, and H. R. Miller. X-ray and optical observations of BL Lac objects: 3C 66A (B0219+428) and ON 325 (B1215+303). *A&A*, 407:453–460, August 2003.
- B. M. Peterson. *An Introduction to Active Galactic Nuclei*. Cambridge, New York Cambridge University Press, 1997, February 1997.
- D. Petry, M. Böttcher, V. Connaughton, A. Lahteenmaki, T. Pursimo, C. M. Raiteri, F. Schröder, A. Sillanpää, G. Sobrito, and L. Takalo, et al. Multiwavelength Observations of Markarian 501 during the 1997 High State. *ApJ*, 536:742–755, June 2000.

- W. H. Press, S. A. Teukolsky, W. T. Vetterling, and B. P. Flannery. *Numerical recipes in C. The art of scientific computing*. Cambridge: University Press, —c1992, 2nd ed., 1992.
- C. M. Raiteri, M. Villata, V. M. Larionov, M. F. Aller, U. Bach, M. Gurwell, O. M. Kurtanidze, A. Lähteenmäki, K. Nilsson, and A. Volvach, et al. Radio-to-UV monitoring of AO 0235+164 by the WEBT and Swift during the 2006-2007 outburst. *A&A*, 480:339–347, March 2008.
- M. Ravasio, G. Tagliaferri, G. Ghisellini, P. Giommi, R. Nesci, E. Massaro, L. Chiappetti, A. Celotti, L. Costamante, and L. Maraschi, et al. BL Lacertae: Complex spectral variability and rapid synchrotron flare detected with BeppoSAX. *A&A*, 383:763–772, March 2002.
- M. Ravasio, G. Tagliaferri, G. Ghisellini, F. Tavecchio, M. Böttcher, and M. Sikora. BeppoSAX and multiwavelength observations of BL Lacertae in 2000. *A&A*, 408: 479–491, September 2003.
- F. M. Rieger and P. Duffy. Shear Acceleration in Relativistic Astrophysical Jets. *ApJ*, 617:155–161, December 2004.
- G. B. Rybicki and A. P. Lightman. *Radiative Processes in Astrophysics*. New York, Wiley-Interscience, 1979. 393 p., 1979.

- R. M. Sambruna, P. Barr, P. Giommi, L. Maraschi, G. Tagliaferri, and A. Treves. The X-ray spectra of blazars: Analysis of the complete EXOSAT archive. *ApJS*, 95:371–385, December 1994.
- M. Sikora, M. C. Begelman, and M. J. Rees. Comptonization of diffuse ambient radiation by a relativistic jet: The source of gamma rays from blazars? *ApJ*, 421:153–162, January 1994.
- M. Sikora, M. Błażejowski, M. C. Begelman, and R. Moderski. Modeling the Production of Flares in Gamma-Ray Quasars. *ApJ*, 554:1–11, June 2001.
- A. Sokolov, A. P. Marscher, and I. M. McHardy. Synchrotron Self-Compton Model for Rapid Nonthermal Flares in Blazars with Frequency-dependent Time Lags. *ApJ*, 613:725–746, October 2004.
- M. Spada, G. Ghisellini, D. Lazzati, and A. Celotti. Internal shocks in the jets of radio-loud quasars. *MNRAS*, 325:1559–1570, August 2001.
- L. Stawarz and M. Ostrowski. Radiation from the Relativistic Jet: A Role of the Shear Boundary Layer. *ApJ*, 578:763–774, October 2002.
- F. W. Stecker, M. A. Malkan, and S. T. Scully. Intergalactic Photon Spectra from the Far-IR to the UV Lyman Limit for  $0 < z < 6$  and the Optical Depth of the Universe to High-Energy Gamma Rays. *ApJ*, 648:774–783, September 2006.

- S. Swordy. Discovery of  $> 100$  GeV Gamma-ray Emission from the Blazar 3C66A by VERITAS. *The Astronomer's Telegram*, 1753:1–1, October 2008.
- L. O. Takalo, M. R. Kidger, J. A. de Diego, A. Sillanpaa, and K. Nilsson. Near infrared monitoring of a sample of blazars with the Carlos Sanchez Telescope. *AJ*, 104:40–52, July 1992.
- L. O. Takalo, A. Sillanpaa, T. Pursimo, H. J. Lehto, K. Nilsson, P. Teerikorpi, P. Heinaemaeki, M. Lainela, M. Kidger, and J. A. de Diego, et al. Monitoring of 3C 66A during an extended outburst. I. The light curves. *A&AS*, 120:313–321, December 1996.
- J. J. P. Virtanen and R. Vainio. Stochastic Acceleration in Relativistic Parallel Shocks. *ApJ*, 621:313–323, March 2005.
- B. J. Wills and D. Wills. C 66A: a Bright New Quasi-Stellar Object. *ApJ*, 190:L97–L98, June 1974.
- S. E. Woosley. Gamma-ray bursts from stellar mass accretion disks around black holes. *ApJ*, 405:273–277, March 1993.
- D. M. Worrall and B. J. Wilkes. X-ray spectra of compact extragalactic radio sources. *ApJ*, 360:396–407, September 1990.

- R. Wurtz, J. T. Stocke, and H. K. C. Yee. The Canada-France-Hawaii Telescope Imaging Survey of BL Lacertae Objects. I. Properties of the Host Galaxies. *ApJS*, 103:109–144, March 1996.
- G. Z. Xie, K. H. Li, F. K. Liu, R. W. Lu, J. X. Wu, J. H. Fan, Y. Y. Zhu, and F. Z. Cheng. CCD photometry of 14 BL Lacertae objects and theoretical model. *ApJS*, 80:683–699, June 1992.
- S. A. Yost, K. Alatalo, E. S. Rykoff, F. Aharonian, C. W. Akerlof, M. C. B. Ashley, C. H. Blake, J. S. Bloom, M. Böttcher, and E. E. Falco, et al. Optical Light Curve and Cooling Break of GRB 050502A. *ApJ*, 636:959–966, January 2006.

## APPENDIX A

# Photon Escape Time Calculation

Here, I write-out the intermediate steps used to derive Eqn. 4.28.

As shown in Figure A.1 (a),  $l_{\text{crit}+}$  is the distance travelled by a photon that managed to escape from the edge of the region in the forward direction making an angle  $\theta_{\text{crit}+}$  with the z-axis and similarly for  $l_{\text{crit}-}$  making an angle  $\pi - \theta_{\text{crit}-}$  with the z-axis, and  $b$  is the corresponding projection of these lengths on the horizontal plane (Figure A.1 (b)).

Using the law of cosines and solving the quadratic equation in  $b$  and realizing that negative distances are unphysical, an expression for  $b$  can be obtained as

$$b = \sqrt{R^2 - r^2 \sin^2 \phi} - r \cos \phi . \quad (\text{A.1})$$

Now, referring to Figure A.1 we can write

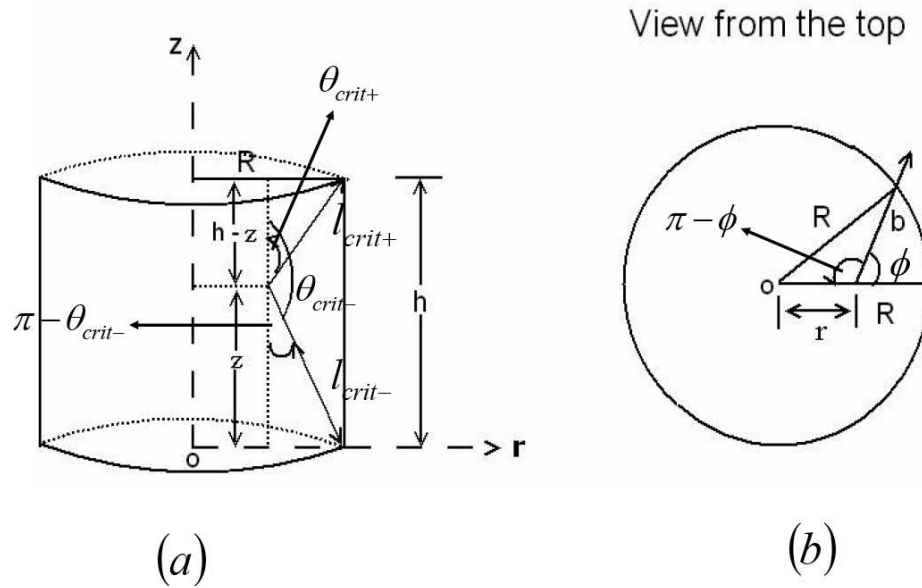


Figure A.1: In (a) we illustrate the three angles of escape along with their corresponding escape lengths. In (b) we show the angle consideration and the projection of the escape lengths on the horizontal plane of the cylinder, when viewed from the top.

$$\begin{aligned}
 \tan \theta_{\text{crit}+} &= \frac{b}{h-z}, \quad \tan \theta_{\text{crit}-} = \frac{-b}{z}, \\
 l_{\text{esc}-} &= \frac{-z}{\mu_-} \quad \text{for } -1 < \mu < \mu_{\text{crit}-}, \\
 l_{\text{esc}} &= \frac{b}{\sqrt{1-\mu^2}} \quad \text{for } \mu_{\text{crit}-} < \mu < \mu_{\text{crit}+}, \\
 l_{\text{esc}+} &= \frac{h-z}{\mu_+} \quad \text{for } \mu_{\text{crit}+} < \mu < +1, \\
 \mu_{\text{crit}+} &= \frac{h-z}{\sqrt{b^2 + (h-z)^2}}, \quad \mu_{\text{crit}-} = \frac{-z}{\sqrt{b^2 + z^2}}.
 \end{aligned} \tag{A.2}$$

Substituting equations A.2 in equation 4.27 (Chapter 4) and then equation 4.27 in 4.26 (Chapter 4), equation 4.26 can be written as

$$\langle t_{\text{ph,esc,V}} \rangle = \left( \frac{1}{\pi R^2 h} \right) \left( \frac{1}{4\pi c} \right) \int_0^{2\pi} \int_0^R \int_0^h \left( \int_0^{2\pi} d\phi \left[ \int_{-1}^{\mu_{\text{crit-}}} l_{\text{esc-}} d\mu_- + \int_{\mu_{\text{crit-}}}^{\mu_{\text{crit+}}} l_{\text{esc}} d\mu + \int_{\mu_{\text{crit+}}}^{+1} l_{\text{esc+}} d\mu_+ \right] \right) d\phi r dr dz , \quad (\text{A.3})$$

which gives

$$\langle t_{\text{ph,esc,V}} \rangle = \left( \frac{1}{\pi R^2 h} \right) \left( \frac{1}{4\pi c} \right) \int_0^{2\pi} \int_0^R \int_0^h \left( \int_0^{2\pi} d\phi \left[ \int_{-1}^{\mu_{\text{crit-}}} \frac{-z}{\mu_-} d\mu_- + \int_{\mu_{\text{crit-}}}^{\mu_{\text{crit+}}} \frac{b}{\sqrt{1-\mu^2}} d\mu + \int_{\mu_{\text{crit+}}}^{+1} \frac{h-z}{\mu_+} d\mu_+ \right] \right) d\phi r dr dz . \quad (\text{A.4})$$

Carrying out integration over  $\mu$ , and realizing that the integration of the right hand side expression over the volume  $\phi$  is going to give  $2\pi$ , the above equation can be written as

$$\langle t_{\text{ph,esc,V}} \rangle = \frac{2}{R^2 h} \int_0^R \int_0^h \left( \int_0^{2\pi} \left( \frac{1}{2c} [(z-h) \ln(h-z) - z \ln z] + I_1 + I_2 + I_3 \right) dz \right) r dr , \quad (\text{A.5})$$

where

$$\begin{aligned} I_1 &= \frac{h-z}{8\pi c} \int_0^{2\pi} \ln(b^2 + (h-z)^2) d\phi, \\ I_2 &= \frac{z}{8\pi c} \int_0^{2\pi} \ln(b^2 + z^2) d\phi, \\ I_3 &= \frac{1}{4\pi c} \int_0^{2\pi} b \left[ \arcsin\left(\frac{h-z}{\sqrt{b^2 + (h-z)^2}}\right) + \arcsin\left(\frac{z}{\sqrt{b^2 + z^2}}\right) \right] dz . \end{aligned} \quad (\text{A.6})$$

The above three integrals can be solved analytically by changing the variable  $h - z = y$  and using the identity  $\arcsin x = \arctan\left(\frac{x}{\sqrt{1-x^2}}\right)$  (p. 56 [Gradshteyn and Ryzhik 1994](#)) to obtain the final expression for the volume and angle averaged photon escape timescale for a cylindrical region to be

$$\langle t_{\text{ph,esc}} \rangle_V = \left(\frac{h}{4c}\right) \ln\left(1 + \frac{R^2}{h^2}\right) - \left(\frac{R^2}{4ch}\right) \ln\left(1 + \frac{h^2}{R^2}\right) + \left(\frac{R}{c}\right) \arctan\left(\frac{h}{R}\right) . \quad (\text{A.7})$$